

UNIVERSIDADE FEDERAL DE MINAS GERAIS

Instituto de Ciências Exatas

Departamento de Química

José María Muñoz López

**Peptides and glycotriazole-peptides: synthesis and solid-state NMR
investigations of their membrane interactions**

Belo Horizonte

2020

UFMG/ICEx/DQ. 1402

D. 763

José María Muñoz López

**Peptides and glycotriazole-peptides: synthesis and solid-state NMR investigations
of their membrane interactions**

Dissertação apresentada ao Departamento de
Química do Instituto de Ciências Exatas da
Universidade Federal de Minas Gerais como
requisito parcial para a obtenção do grau de
Mestre em Química – Química Orgânica

Orientador: Prof. Jarbas Magalhães Resende

Belo Horizonte

2020

Ficha Catalográfica

L864p López, José María Muñoz
2020 Peptides and glycotriazole-peptides [manuscrito] :
D synthesis and solid-state NMR investigations of their
membrane interactions / José María Muñoz López. 2020.
[xiv], 108 f. : il.

Orientador: Jarbas Magalhães Resende.

Dissertação (mestrado) - Universidade Federal de
Minas Gerais - Departamento de Química.
Inclui bibliografia.

1. Química orgânica - Teses. 2. Peptídios - Síntese
- Teses. 3. Ressonância magnética nuclear - Teses. 4.
Dinâmica molecular - Teses. 5. Atividade antifúngica -
Teses. 6. Testes microbiológicos - Teses. 7. Química
supramolecular - Teses. 8. Biofísica - Teses. I.
Resende, Jarbas Magalhães, Orientador II. Título.

CDU 043



UNIVERSIDADE FEDERAL DE MINAS GERAIS



"Peptides and glycotriazole-peptides: synthesis and solid-state NMR investigations of their membrane interactions"

José María Muñoz López

Dissertação aprovada pela banca examinadora constituída pelos Professores:

Prof. Jarbas Magalhães Resende - Orientador
UFMG

Prof. Rubén Dario Sinisterra Millán
UFMG

Prof. Tiago Antônio da Silva Brandão
UFMG

Belo Horizonte, 15 de julho de 2020.



Documento assinado eletronicamente por **Jarbas Magalhaes Resende, Presidente de comissão**, em 16/07/2020, às 16:58, conforme horário oficial de Brasília, com fundamento no art. 6º, § 1º, do [Decreto nº 8.539, de 8 de outubro de 2015](#).



Documento assinado eletronicamente por **Ruben Dario Sinisterra Millan, Membro de comissão**, em 16/07/2020, às 17:24, conforme horário oficial de Brasília, com fundamento no art. 6º, § 1º, do [Decreto nº 8.539, de 8 de outubro de 2015](#).



Documento assinado eletronicamente por **Tiago Antonio da Silva Brandao, Professor do Magistério Superior**, em 16/07/2020, às 18:25, conforme horário oficial de Brasília, com fundamento no art. 6º, § 1º, do [Decreto nº 8.539, de 8 de outubro de 2015](#).



A autenticidade deste documento pode ser conferida no site https://sei.ufmg.br/sei/controlador_externo.php?acao=documento_conferir&id_orgao_acesso_externo=0, informando o código verificador **0177441** e o código CRC **4A3F119E**.

*“Caminante, no hay camino,
se hace camino al andar”
Antonio Machado*

ABSTRACT

Peptides and glycotriazole-peptides: synthesis and solid-state NMR investigations of their membrane interactions

On the verge of a post-antibiotic era due to the rapidly increasing resistance that countless pathogens are developing, antimicrobial peptides are in the limelight for research as an alternative to conventional antibiotics. Besides, several studies have revealed that their mechanism of action is through the cell membrane disruption, which hampers microbial resistance. Ocellatins are a family of antimicrobial peptides which has been isolated from the skin secretions of anurans of the *Leptodactylus* genus. Three of these peptides, namely ocellatin-LB1, -LB2 and -F1 present a primary structure identical from residues 1 to 23 (Oce-LB1 sequence), whereas Oce-LB2 carries an extra Asn and Oce-F1 extra Asn-Lys-Leu residues at their C-termini. In spite of having similar primary structures, these extra amino acids ensure different membrane interactions as well as different antimicrobial potentials (-F1 >> -LB1 \geq -LB2), as proved by several biophysical studies and biological assays. In addition, the synthetic modification of natural peptides, such as hylaseptin-P1 (HSP1) and phylloseptin-2 (PS-2), by adding a glycotriazole residue led to enhanced antifungal activities of the respective glycotriazole-peptides (GtPs). Thus, in order to gain extra insight into how the subtle differences in the primary sequence of ocellatins at the C-termini and how the glycotriazole moiety increases both antimicrobial and antifungal peptides activities, we decided to investigate the membrane topologies of these peptides by static solid-state NMR spectroscopy. To this end, peptides were selectively labeled at single positions with ^{15}N -Leu or ^{15}N -Ala and 3,3,3- $^2\text{H}_3$ -Ala amino acid analogs during the peptide synthesis, which followed the Fmoc solid-phase strategy. Ocellatins were yielded as (3,3,3- $^2\text{H}_3$ -Ala-10, ^{15}N -Leu-17)-Oce (-LB1, -LB2 and -F1). Not least, the synthetic modification of labelled HSP1 and PS-2 peptides was carried out by the “click” reaction between the azide per-*O*-acetylate-glycose derivate and the propargyl glycine residue contained in their respective peptidyl-resin derivatives, yielding (3,3,3- $^2\text{H}_3$ -Ala-8, ^{15}N -Ala-10)-[pOAcGlc-Trz-A¹]-HSP1-NH₂ and (3,3,3- $^2\text{H}_3$ -Ala-10, ^{15}N -Leu-15)-[pOAcGlc-Trz-A¹⁴]-PS-2. Thus, labelled peptides were reconstituted into oriented phospholipid bilayers. The phospholipid bilayers encompassing peptides or GtPs were monitored by proton-decoupled ^{31}P solid-state NMR spectroscopy. On the other hand, peptides’ both tilt and pitch angles were studied by combined proton-decoupled ^{15}N and ^2H solid-state NMR spectroscopy along with simulations of both ^{15}N chemical shift and ^2H quadrupolar splitting. To our knowledge, this work investigates in an unprecedented way the membrane topologies of both glycotriazole-peptides and ocellatins. The membrane interactions of the ocellatin peptides were further investigated by isothermal titration calorimetry, surface plasmon resonance spectroscopy and computational simulations of molecular dynamics.

Key Words: Antimicrobial peptides, Solid-state NMR, Solid-phase synthesis, Biophysics, Supramolecular Chemistry, Organic Chemistry

RESUMO

Peptídeos e glicotriazol-peptídeos: síntese e estudos por RMN de sólidos das suas interações com membrana

À beira de uma era pós-antibióticos, causada pelo rápido aumento da resistência desenvolvida por inúmeros patógenos, os peptídeos antimicrobianos estão no centro das atenções em pesquisas, como uma alternativa aos antibióticos convencionais. Além disso, vários estudos mostram que seu mecanismo de ação envolve a ruptura da membrana celular, o que dificulta a resistência microbiana. As ocelatinas são uma família de peptídeos antimicrobianos, que são isolados das secreções cutâneas de anuros do gênero *Leptodactylus*. Três desses peptídeos, a saber ocelatina-LB1, -LB2 e -F1 apresentam estruturas primárias idênticas dos resíduos 1 a 23 (sequência da Oce-LB1), enquanto a Oce-LB2 contém resíduo extra de Asn e a Oce-F1 resíduos extra de Asn-Lys-Leu em suas porções C-terminal. Apesar de terem estruturas primárias semelhantes, estes aminoácidos extra asseguram diferentes potenciais antimicrobianos e diferentes magnitudes de interação com membranas (-F1 >>, -LB1 \geq -LB2), como provado por vários estudos biofísicos e ensaios biológicos. A modificação sintética de peptídeos naturais, como hilaseptina-P1 (HSP1) e filoseptina-2 (PS-2), pela adição de um resíduo glicotriazólico, tem levado a glicotriazol-peptídeos (GtPs) derivados com atividades antifúngicas bem mais pronunciadas. Assim, a fim de obter informação extra sobre como diferenças sutis nas porções C-terminais das ocelatinas e como a inserção da unidade glicotriazólica interferem nas atividades antimicrobianas e antifúngicas dos peptídeos, neste trabalho são investigadas as topologias de membrana desses derivados peptídicos por espectroscopia de RMN sólidos estáticos. Para tal, os peptídeos foram marcados seletivamente como análogos de resíduos de aminoácido de ^{15}N -Leu ou ^{15}N -Ala e $3,3,3\text{-}^2\text{H}_3$ -Ala durante a síntese dos peptídeos em fase sólida. As ocelatinas foram obtidas como $(3,3,3\text{-}^2\text{H}_3\text{-Ala-10, }^{15}\text{N}\text{-Leu-17})\text{-Oce}$ (-LB1, -LB2 e -F1). Ademais, a modificação sintética para obtenção dos derivados glicotriazólicos marcados dos peptídeos HSP1 e PS-2 foi realizada pela reação de "click" entre o derivado azido per-*O*-acetilado da glicose e a peptidil-resina contendo resíduo de propargil glicina, tendo-se obtido a $(3,3,3\text{-}^2\text{H}_3\text{-Ala-8, }^{15}\text{N}\text{-Ala-10})\text{-[pOAcGlc-Trz-A}^1\text{]-HSP1-NH}_2$ e a $(3,3,3\text{-}^2\text{H}_3\text{-Ala-10, }^{15}\text{N}\text{-Leu-15})\text{-[pOAcGlc-Trz-A}^{14}\text{]-PS-2}$. Assim, os respectivos peptídeos e GtPs marcados foram reconstituídos em bicamadas fosfolipídicas mecanicamente orientadas. O efeito exercido pelos peptídeos nas bicamadas lipídicas foi monitorado por espectroscopia de RMN de ^{31}P desacoplada de ^1H . Por outro lado, os ângulos de inclinação e de rotação interna dos derivados peptídicos foram obtidos por espectroscopia de RMN de sólidos de ^2H e de ^{15}N desacoplado de ^1H , juntamente com simulações do respectivos deslocamentos químicos de ^{15}N e desdobramentos quadrupolares de ^2H . Até o ponto que sabemos, este trabalho investiga de forma inédita as topologias de interação tanto de glicotriazol-peptídeos quanto de peptídeos da família das ocelatinas. As interações com membranas das ocelatinas foram ainda investigadas em maiores detalhes por calorimetria de titulação isotérmica, espectroscopia de ressonância plasmônica de superfície e por simulações de dinâmica molecular.

Palavras chave: Peptídeos antimicrobianos, RMN em estado sólido, Síntese em fase sólida, Biofísica, Química Supramolecular, Química Orgânica

List of figures

Figure 1: Modes of lipid membrane permeabilization by AMPs (from Silva et al.) ¹⁸	16
Figure 2: Chemical structure of the lipids used in the preparation of supported bilayers and LUV.....	19
Figure 3: Modifications of HSP1 peptide previously studied by Eduardo F.C. Junior et al...	22
Figure 4: Examples of polymeric supports according to the desired C-terminal nature of peptides.....	24
Figure 5: Orthogonal protecting group approach and Fmoc removal with piperidine (adapted from Kimmerlin et al., 2004) ⁴¹	25
Figure 6: Schematic representation of the principles of solid-phase peptide synthesis.....	26
Figure 7: Activation of the carboxyl group with DIC/HOBt and coupling reaction.	27
Figure 8: Schematic representation of Kaiser's test and reaction mechanism between free amino groups and ninhydrin.....	27
Figure 9: Schematic comparison of Huisgen's reaction and CuAAC reaction.	28
Figure 10: Mechanism of the Copper-catalyzed Azide-Alkyne Cycloaddition (CuAAC) involving a dinuclear Copper intermediate.	29
Figure 11: Chemical structure of both [pOAcGlc-Trz-A ¹]-HSP1-NH ₂ and [pOAcGlc-Trz-A ¹⁴]-PS-2 peptides. ¹⁵ N labelled sites are in green and ² H ₃ -Ala labelled sites are in pink.	30
Figure 12: "Click" reaction between the azide per-O-acetylate-glucose derivate and the propargyl glycine residue contained in the peptidyl-resin derivatives.....	33
Figure 13: HPLC chromatograms obtained for Oce-F1 (black), Oce-LB1 (red) and Oce-LB2 (blue) analytical profiles, with a Waters μBondapak TM C18 reverse stationary phase 10mm (7.8 x 3mm) semi-preparative column.	36
Figure 14: HPLC chromatograms obtained for Oce-F1 (black), Oce-LB1 (red) and Oce-LB2 (blue) purification, with a Waters μBondapak TM C18 reverse stationary phase 10mm (7.8 x 3mm) semi-preparative column.	36
Figure 15: Mass spectra obtained by MALDI-TOF spectrometry for (A) Oce-LB1, (B) Oce-LB2 and (C) Oce-F1 after HPLC purification.	37
Figure 16: ¹ H-NMR spectra of (A) Oce-LB1 recorded at 600 MHz spectrometer and (B) [LB1+163] impurity recorded at 350 MHz spectrometer. Both experiments were run in TFE-d ₂ :H ₂ O (60:40, v:v) containing 20 mM pH 7.0 phosphate buffer. The spectrum presented in (A) was obtained by Gomes et al., 2018 ³⁰	38
Figure 17: HPLC chromatograms obtained for [pOAcGlc-trz-A1]-HSP1-NH ₂ (black) and [pOAcGlc-trz-A14]-PS-2 (red) analytical profiles, with a Waters μBondapak TM C18 reverse stationary phase 10mm (7.8 x 3mm) semi-preparative column.	39
Figure 18: HPLC chromatograms obtained for [pOAcGlc-trz-A1]-HSP1-NH ₂ (black) and [pOAcGlc-trz-A14]-PS-2 (red) purifications, with a Waters μBondapak TM C18 reverse stationary phase 10mm (7,8 x 3mm) semi-preparative column.	39
Figure 19: Mass spectra obtained by MALDI-TOF spectrometry for [pOAcGlc-trz-A1]-HSP1-NH ₂ (A) and [pOAcGlc-trz-A14]-PS-2 (B) after HPLC purification.....	40
Figure 20: TFA acidolysis of Rink-amide MBHA resin and side-S _E Ar (electrophilic aromatic substitution) of tryptophan indole ring.....	41
Figure 21: Proposal of TFA acidolysis of Rink-amide AM resin and side-reactions with any nucleophile site and 2-(4-methylphenoxy) acetamide cation.....	42
Figure 22: Proposal for the single deprotection [MW-43] at C-6 of the per-O-acetylate-glucose moiety.....	43

Figure 23: Ellipsoidal representation of the ^{15}N chemical shift tensor next to the molecular frame of the peptide bond. Both σ_{11} and σ_{33} are aligned within the plane of the paper whereas σ_{22} is oriented toward the viewer (adapted from Bechinger et al., 2002) ⁵²	47
Figure 24: Representation of the proton-decoupled ^{15}N solid-state NMR spectrum and the orientation of helical peptides according to ^{15}N chemical shift (adapted from Bechinger et al., 2002) ⁵²	48
Figure 25: Schematic representation of Θ , the angle between the static magnetic field B_0 and the principal Z-axis of the electric field gradient tensor.	51
Figure 26: Proton-decoupled ^{15}N NMR spectra of Ocellatins at 1.0 mol % reconstituted into mechanically oriented POPC lipid bilayers. (A) (3,3,3- $^2\text{H}_3$ -Ala-10, ^{15}N -Leu-17)-Oce-LB1, (B) (3,3,3- $^2\text{H}_3$ -Ala-10, ^{15}N -Leu-17)-Oce-LB2 and (C) (3,3,3- $^2\text{H}_3$ -Ala-10, ^{15}N -Leu-17)-Oce-F1. All spectra were recorded for alignments with the membrane normal parallel to the magnetic field of the spectrometer.....	55
Figure 27: ^2H NMR spectra of Ocellatins at 1.0 mol % reconstituted into mechanically oriented POPC lipid bilayers. (A) (3,3,3- $^2\text{H}_3$ -Ala-10, ^{15}N -Leu-17)-Oce-LB1, (B) (3,3,3- $^2\text{H}_3$ -Ala-10, ^{15}N -Leu-17)-Oce-LB2 and (C) (3,3,3- $^2\text{H}_3$ -Ala-10, ^{15}N -Leu-17)-Oce-F1. All spectra were recorded for alignments with the membrane normal parallel to the magnetic field of the spectrometer. All central peaks are from the residual HDO form of deuterium depleted water (≤ 1 ppm).....	56
Figure 28: Proton-decoupled ^{31}P NMR spectra of mechanically oriented POPC lipid bilayers containing (A) (3,3,3- $^2\text{H}_3$ -Ala-10, ^{15}N -Leu-17)-Oce-LB1, (B) (3,3,3- $^2\text{H}_3$ -Ala-10, ^{15}N -Leu-17)-Oce-LB2 and (C) (3,3,3- $^2\text{H}_3$ -Ala-10, ^{15}N -Leu-17)-Oce-F1 at 1.0 mole %. Samples were prepared by spreading 50 mg of lipids on 22 glass plates. All spectra were recorded for alignments with the membrane normal parallel to the magnetic field of the spectrometer.	57
Figure 29: Alignments of (A) Oce-LB1, (B) Oce-LB2 (B) and (C) Oce-F1 (C) in lipid bilayers shown as functions of the tilt and rotational pitch angles. Black points represent orientations that are in agreement within the respective ^{15}N chemical shift whereas red points represent alignments that agree within the respective deuterium quadrupolar splitting. The intersection points shown as blue circles indicate orientations that simultaneously agree with both experimental parameters. Underneath each contour plot the respective peptide three-dimensional structure (PDB 5UA6, 5UA7 and 5U9Y ³⁰) is used to the topologies related to the intersection points for (D) Oce-LB1, (E) Oce-LB2 and (F) Oce-F1 (the N-termini shown in the back). Rotated views of the most thermodynamically favored alignment of each peptide is shown in panel (G). Hydrophilic residues are shown in green, whereas hydrophobic residues in blue. In panel (G) the lysine residues (-7, -11, -20 and -24) are highlighted in yellow. The gray areas represent approximately the hydrophobic thickness of a bilayer.....	58
Figure 30: Proton-decoupled ^{15}N NMR spectra of glycotriazole-peptides at 1.0 mol % reconstituted into mechanically oriented phospholipid bilayers. (A) (3,3,3- $^2\text{H}_3$ -Ala-8, ^{15}N -Leu-15)-[pOAcGlc-Trz-A ¹⁴]-PS-2 in POPC:POPS (3:1 molar ratio), (B) (3,3,3- $^2\text{H}_3$ -Ala-8, ^{15}N -Leu-10-[pOAcGlc-Trz-A ¹]-HSP1-NH ₂ in POPC:POPG:Ergosterol (3:1:1 molar ratio). All spectra were recorded for alignments with the membrane normal parallel to the magnetic field of the spectrometer.....	60
Figure 31: ^2H NMR spectra of glycotriazole-peptides at 1.0 mol % reconstituted into mechanically oriented phospholipid bilayers. (A) (3,3,3- $^2\text{H}_3$ -Ala-8, ^{15}N -Leu-15)-[pOAcGlc-Trz-A ¹⁴]-PS-2 in POPC:POPS (3:1 molar ratio), (B) (3,3,3- $^2\text{H}_3$ -Ala-8, ^{15}N -Leu-10-[pOAcGlc-Trz-A ¹]-HSP1-NH ₂ in POPC:POPG:Ergosterol (3:1:1 molar ratio). All spectra were recorded for alignments with the membrane normal parallel to the magnetic field of the spectrometer. All central peaks are from the residual HDO form of deuterium depleted water (≤ 1 ppm). ..	61
Figure 32: Proton-decoupled ^{31}P NMR spectrum of mechanically oriented (A) POPC:POPS (3:1 molar ratio) phospholipid bilayers containing (3,3,3- $^2\text{H}_3$ -Ala-8, ^{15}N -Leu-15)-[pOAcGlc-	

Trz-A¹⁴]-PS-2 (B) POPC:POPG:Ergosterol (3:1:1 molar ratio) phospholipid bilayers containing (3,3,3-²H₃-Ala-8, ¹⁵N-Leu-10-[pOAcGlc-Trz-A¹]-HSP1-NH₂ F1 at 1.0 mole %. Samples were prepared by spreading 50 mg of lipids on 22 glass plates. All spectra were recoded for alignments with the membrane normal parallel to the magnetic field of the spectrometer. 62

Figure 33: Alignments of [pOAcGlc-Trz-A¹⁴]-PS-2 in lipid bilayers shown as functions of the tilt and rotational pitch angles. Black points represent orientations that are in agreement within the respective ¹⁵N chemical shift whereas red points represent alignments that agree within the respective deuterium quadrupolar splitting. The intersection points shown as blue circles indicate orientations that simultaneously agree with both experimental parameters. Next to the contour plot the [pOAcGlc-Trz-A¹⁴]-PS-2 three-dimensional structure used to the topologies related to the intersection points (the N-termini shown in the back). Rotated view of the most thermodynamically favored alignment (II) is shown underneath. Hydrophilic residues are shown in green, hydrophobic residues in blue and the glycotriazole residue in red. The gray areas represent approximately the hydrophobic thickness of a bilayer. 63

Figure 34: Alignments of [pOAcGlc-Trz-A¹]-HSP1-NH₂ in lipid bilayers shown as functions of the tilt and rotational pitch angles. Black points represent orientations that are in agreement within the respective ¹⁵N chemical shift whereas red points represent alignments that agree within the respective deuterium quadrupolar splitting. The intersection points shown as blue circles indicate orientations that simultaneously agree with both experimental parameters. Next to the contour plot the [pOAcGlc-Trz-A¹]-HSP1-NH₂ three-dimensional structure used to the topologies related to the intersection points (the N-termini shown in the back). Rotated view of the most thermodynamically favored alignment (IV) is shown underneath. Hydrophilic residues are shown in green, hydrophobic residues in blue and the glycotriazole residue in red. The gray areas represent approximately the hydrophobic thickness of a bilayer. 64

Figure 35: Membrane alignments of PS-2 (Resende et al., 2014)⁵³ and [pOAcGlc-Trz-A¹⁴]-PS-2 (GtPS-2). Hydrophilic residues are shown in green and hydrophobic residues in blue. The red sticks represent Thr-14 for PS-2 and the glycotriazole moiety for [pOAcGlc-Trz-A¹⁴]-PS-2. The gray areas represent approximately the hydrophobic thickness of a bilayer..... 67

Figure 36: Schiffer-Edmundson wheel projection of [pOAcGlc-Trz-A¹]-HSP1-NH₂. Hydrophobic residues are shown in blue, positively charged residues are shown in green, negatively charged residues are shown in purple and the glycotriazole residue is shown in red. The pair of black lines delimit the separation between the hydrophilic and hydrophobic faces. GTrz circle was added manually in accordance to the three-dimensional structure of [pOAcGlc-Trz-A¹]-HSP1-NH₂. The hydrophobic perimeter is represented by the length of the external circumference delimited by these pairs of solid lines. This simulation was performed at <http://lbqp.unb.br/NetWheels/>. 70

Figure 37: (A) raw ITC data (B) binding isotherm from ITC experiment (from Frasca 2016)⁹⁴. 73

Figure 38: Simplified scheme of SPR operating mechanism (from Patching et. al)⁹⁶. 74

Figure 39: General sensogram showing the stages of interaction peptide-bilayer interaction (from Patching et. al)⁹⁶. 74

Figure 40: Isothermal titration calorimetry of ocellatin peptides in 10 mM Tris-HCl, pH 8.5, containing 20 mM NaCl with POPC LUVs (20mM stock solutions in 10 mM tris-HCl, pH 8.5 containing 20 mM NaCl). The heat flow for (A) ocellatin-LB1 (35.3 μM), (B) Ocellatin-LB2 (36.1 μM) and (C) ocellatin-F1 (18.2 μM) injection as a function of time (raw data). The enthalpy as a function of the (D) Ocellatin-LB1, (E) Ocellatin-LB2 and (F) Ocellatin-F1 to POPC molar ratio. The baseline was corrected, and the heat of dilution subtracted from each experimental point. 82

Figure 41: SPR sensograms for the bilayer interaction of (A) Ocellatin-LB1, (B) Ocellatin-LB2 and (C) Ocellatin-F1. POPC bilayers were immobilized onto the surface of a SiO₂ sensor chip and the peptides were injected at 2.6, 5.12, 11.25, 22.5 and 45 μM concentrations in 10 mM Tris-HCl buffer, pH 8.0, containing 20 mM NaCl. (D) Comparative sensogram for the bilayer interaction of the three ocellatins at ~ 50 μM (Oce-LB1 and -LB2 at 52 μM and -F1 50 μM). (E) Non-linear fitting of RU intensities as a function of peptide-POPC molar ratio of Oce-LB1 (red), Oce-LB2 (blue) and Oce-F1 (black). 83

Figure 42: Setup of the Ocellatin-LB2-POPC bilayer model. Initially the peptide is included in the simulation box ~20 Å apart from the bilayer surface at the topology derived from solid-state NMR data ($t = 86^\circ$ and $r = 26^\circ$). Different snapshots are shown to represent stages of the peptide insertion into the bilayer. Variations during the simulation of (A) the tilt angle and (B) the insertion depth relative to the distance between the isotopically labelled ¹⁵N-Leu-17 site and the lipid bilayer. (C) Lateral perspectives of the selected snapshots are shown to the right. 85

Figure 43: MD simulations of Ocellatin-LB2 reconstituted into POPC bilayer. (A) Rotational pitch and (B) tilt angles as function of the simulation time. The red dotted lines represent the topology determined from solid-state NMR data ($\tau = 86^\circ$ and $\rho = 26^\circ$) and the blue dotted lines represent the respective variations ($\Delta\tau$ and $\Delta\rho$) within $\pm 3^\circ$. (C) Lateral perspectives of selected snapshots with the respective angular pairs are shown to the right. . 86

Figure 44: Density profiles of Ocellatin-LB2 reconstituted into the POPC bilayer averaged over the last 200 ns of MD simulation (800 to 1000 ns). (A) Density profiles of the phosphorous and nitrogen atoms (POPC-P; POPC-N) in each bilayer leaf. From the average position of the P atoms of each leaf it is possible to estimate the center of bilayer at 4.47 nm. (B) Density profiles of oxygen atoms, in the ester groups (O21/O22 and O31/O32) of POPC. (C) Density profile for the amidic nitrogen of Ala-10, Leu-17 and Met-22. Together, these density profiles suggest that Ocellatin-LB2 is in the transition region of the bilayer hydrophobic core, with Ala-10, Leu-17 and Met-22 density peaks in the region of POPC O31/O32 atoms. Hydrogen bond analysis indicate interactions of the lysine residues (Lys-7, Lys-11 and Lys-20) with the phosphate groups and the oxygen atoms of the ester groups (data not shown). 87

List of tables

Table 1: Primary structures and membrane disruptive properties of three ocellatins	20
Table 2: Primary structure and labeled sites of ocellatins and glycotriazole-peptides	30
Table 3: Atoms used to align both peptides and glycotriazole-peptides	54
Table 4: Summary of the solid-state NMR parameters and membrane topologies for Oce-LB1, Oce-LB2 and Oce-F1	59
Table 5: Summary of the solid-state NMR parameters and membrane topologies for GtP-PS2 and GtP-HSP1-NH ₂	64
Table 6: Thermodynamic parameters obtained from ITC in both POPC and POPC:POPG (3:1 mole/mole) ³⁰ membranes	82
Table 7: Experimental Rotation and Tilt angle in the MD simulations	86

List of abbreviations and acronyms

AMBER	Assisted Model Building with Energy Refinement
AMP(s)	Antimicrobial peptide(s)
CD	Circular dichroism
DCM	Dichloromethane
DFT	Density Functional Theory
DIC	<i>N,N'</i> -diisopropylcarbodiimide
DMF	<i>N,N'</i> -dimethylformamide
DPC	Dodecylphosphocoline
EDT	1,2-Ethanedithiol
EDTA	Ethylenediaminetetraacetic acid
Fmoc	9-fluorenylmethoxycarbonyl
GROMACS	Groningen Machine for Chemical Simulations
GtP	Glycotriazole-peptide
HOBt	1-hydroxybenzotriazole
HSP1	Hylaseptin-P1
HSP1-NH ₂	C-terminal amidated Hylaseptin-P1
IPA	Isopropyl alcohol
LINCS	Linear Constraint Solver
LUVs	Large unilamellar vesicles
MALDI	Matrix assisted laser desorption/ionization
MD	Molecular Dynamics
MS	Mass spectrometry
Oce-F1	Ocellatin-F1
Oce-LB1	Ocellatin-LB1

Oce-LB2	Ocellatin-LB2
NOESY	Nuclear Overhauser effect spectroscopy
PDB	Protein data bank
[pOAc-Triz-A ¹]-HSP1	[[3-per- <i>O</i> -acetyl- β -glucopyranosyl-1,4-triazole-Alanine]-Residue ¹]- hylaseptin-1
[pOAc-Triz-A ¹⁴]-PS-2	[[3-per- <i>O</i> -acetyl- β -glucopyranosyl-1,4-triazole-Alanine]-Residue ¹⁴]- Phylloseptin-2
POPC	1-palmitoyl-2-oleoyl- <i>sn</i> -glycero-3-phosphocoline
POPG	1-palmitoyl-2oleoyl- <i>sn</i> -glycero-3-(phosphor-rac-(1-glycerol))
POPS	1-palmitoyl-2-oleoyl- <i>sn</i> -glycero-3-phospho-L-serine
RMSD	Root-Mean-Square Deviation
RU	Reconstructed intensity in relative Units
SDS	Sodium dodecyl sulfate
SIPIDS	Stockholm Lipids
PS-2	Phylloseptin-2
SPR	Surface Plasmon Resonance
TFA	Trifluoroacetic acid
TFE	2,2,2-Trifluoroethanol
THF	Tetrahydrofuran
TIS	Triisopropylsilane
ρ	Pitch angle
τ	Tilt angle

Acknowledgements

Agradecimentos-Agracedimientos-Agraïments

En retrospectiva, me n'adono com aquesta experiència d'haver viscut dos anys fora de casa no només ha eixamplat la meva formació com a químic, sinó que també m'ha fet créixer com a persona. He après sobre la importància dels principals moviments socials contra les seves formes d'opressió, la importància de les polítiques públiques com a mitjà per combatre les desigualtats socials i el poder de l'educació com a eina transformadora, entre d'altres. Viure fora és una frenesia d'estímul nous que fan que sembli que la vida passa en un tancar i obrir d'ulls. I la veritat és que la vida no s'atura ni aquí ni allà. Ets lluny, vivint aventures que mai hauries viscut si no haguessis marxat, però alhora, ets conscient que estàs perdent moments significatius de la teva vida d'allà, de Barcelona. En el transcurs d'aquests dos anys fora, en aquest petit instant d'un tancar i obrir d'ulls, el meu iaio Paco, el meu avi José i el meu oncle, i padrí, Edu han marxat. D'aquesta manera, m'agradaria dedicar aquest treball de màster als que quan vaig marxar hi eren, però que malauradament ara quan hi torni, no hi seran més. Us estimo.

Agradezco a mi padre y a mi madre (*in memoriam*) por todos sus esfuerzos en darme la mejor educación posible. Por motivarme a querer continuar estudiando y apoyarme, o haberme apoyado, en todas las decisiones que tomé para el trazado de mi futuro.

Agreixo a les meves avies, a les meves tietes i als meus oncles per tot el recolzament durant aquests anys d'estudis, per sempre desitjar-me el millor pel meu futur encara que "si és més a prop de casa, millor".

Agradeço ao professor Jarbas Magalhães Resende pela orientação científica neste trabalho nada trivial, especialmente nas simulações das topologias, pelo companheirismo, o carinho e a confiança. Sou muito grato pelas sugestões, conversas e discussões realizadas ao longo desses dois anos de projeto. Sua orientação foi chave para minha formação como cientista!

I am utterly grateful to professor Burkhard Bechinger for his trust and acceptance in his research team in Strasbourg, as well as for his critical reading in the manuscripts.

I owe a debt of gratitude to Dr Evgeniy Salnikov and Christopher Aisenbrey for their patience and time to teach me how to work with solid-state NMR spectrometers and also to Dr Elise Glattard for her help with HPLC.

Agradeço ao professor Rodrigo Verly (UFVJM) pela recepção as duas vezes que fui em Diamantina, o companheirismo, a amizade e auxílio em diversas etapas deste projeto assim como na leitura do manuscrito.

Agradeço ao Dr. Francisco Gomes Neto (Fiocruz) pela realização dos estudos de simulação de dinâmica molecular apresentados em este trabalho, as discussões sob o projeto, assim como pela recepção no Rio de Janeiro.

Agradeço à banca avaliadora: Prof. Dr. Rubén, Prof. Dr. Tiago e suplente Profa. Dra. Amanda, pelo tempo que dispuseram e se dedicaram na correção e melhorias da dissertação.

Agradeço aos meus companheiros e amigos do LASEP, Jade Lomeo, Lídia Barbosa, Breno Barbosa, Claudia Mancilha, Lucas Raposo e Izabella Ercole. Os almoços na bandeirão e os “jaeh” depois de trabalhar no lab: tudo pra mim.

Agradeço ao LASEB e em especial à Talita, pelo auxílio no HPLC e SPR, e ao Daniel A.G.R.M e Carolina S.F., pela colaboração com os experimentos de ITC e SPR.

Agradeço ao Hélio por estar sempre ao meu lado, por ser uma pessoa maravilhosa que todo dia me inspira mais, pela paciência e pelas forças dadas durante a realização dessa pesquisa

Agradeço aos pais do Hélio, Sãozinha e Hélio, pelo recebimento, carinho e cuidado durante estes anos.

Agradeço ao Centro de Laboratórios Multiusuários (CELAM) e ao Laboratório de Ressonância Magnética (LAREMAR) da UFMG pela realização de análises de espectrometria de massas e de RMN, respectivamente. Agradeço ao laboratório de RMN de sólidos da Universidade de Estrasburgo pela realização de análises de RMN.

Agradeço ao Conselho Nacional de Desenvolvimento Científico e Tecnológico (CNPq), à Fundação de Ampara à Pesquisa do Estado de Minas Gerais (FAPEMIG) e à Coordenação de Aperfeiçoamento de Pessoal de Nível Superior (CAPES) pelo fomento aos trabalhos desenvolvidos.

Finalmente, agradeço ao Conselho Nacional de Desenvolvimento Científico e Tecnológico (CNPq) pela concessão da minha bolsa de mestrado.

SUMMARY

ABSTRACT	II
RESUMO	III
List of figures	IV
List of tables	VIII
List of abbreviations and acronyms	IX
Acknowledgements	XI
SUMMARY	XIII
Chapter 1: Introduction to Antimicrobial Peptides (AMPs)	15
1.1. Mechanism of action	16
1.2. Mimetic membrane models	18
1.3. Background of the molecules studied in this master's thesis	20
Chapter 2: Solid-Phase Synthesis of Peptides and Glycotriazole-Peptides	24
2.1. Introduction	24
2.1.1 Peptide solid-phase synthesis	24
2.1.2 Copper(I)-catalyzed alkyne-azide cycloaddition	28
2.2. Objectives	30
2.3. Methods	31
2.3.1. Synthesis of selectively labeled (3,3,3- ² H ₃ -Ala-10, ¹⁵ N-Leu-17)-Oce (-LB1, -LB2 and -F1)	31
2.3.2. Synthesis of selectively labeled Glycotriazole-peptides (3,3,3- ² H ₃ -Ala-8, ¹⁵ N-Ala-10)-[pOAcGlc-Trz-A ¹]-HSP1-NH ₂ and (3,3,3- ² H ₃ -Ala-10, ¹⁵ N-Leu-15)-[pOAcGlc-Trz-A ¹⁴]-PS-2	32
2.3.3. Purification	33
2.4. Results	35
2.4.1. Synthesis of selectively labeled peptide derivatives	35
2.4.2. Purification of ocellatins	35
2.4.3. Purification of glycotriazole-peptides	38
2.5. Discussion	41
Chapter 3: Membrane topology and interaction of peptides and glycotriazole peptides by static solid-state NMR spectroscopy	44
3.1. Introduction	44
3.1.1. Chemical shift anisotropy	44
3.1.2. Deuterium quadrupolar splitting	48
3.2. Objectives	52
3.3. Methods	52
3.3.1. Solid-state NMR spectroscopy	52
3.3.2. Simulations of the membrane topology	53
3.4. Results	55
3.4.1. Ocellatins	55
3.4.2. Glycotriazole-peptides	60
3.5. Discussion	65
3.5.1. Ocellatins	65
3.5.2. Glycotriazole-peptides	67

Chapter 4: Computational and biophysical studies on the membrane interactions of ocellatins	71
4.1. Introduction	71
4.1.1. Isothermal titration calorimetry (ITC)	71
4.1.2. Surface plasmon resonance spectroscopy (SPR)	73
4.1.3. Molecular dynamics (MD)	75
4.2. Objectives	76
4.3. Methods	77
4.3.1. Isothermal titration calorimetry (ITC)	77
4.3.2. Surface Plasmon Resonance (SPR).....	77
4.3.3. Molecular dynamics simulations.....	78
4.4. Results	81
4.5. Discussion	88
Chapter 5: Conclusions.....	90
Bibliography	92
APPENDIX 1	102
APPENDIX 2	103
APPENDIX 3	105
APPENDIX 4	107

Chapter 1: Introduction to Antimicrobial Peptides (AMPs)

Antimicrobial peptides (AMPs) and proteins are an array of naturally occurring molecules produced as a first line of defense by both multicellular and unicellular organisms, although in higher eukaryotic organisms AMPs may be also referred to as ‘host defense peptides’ due to their immunomodulatory activities¹.

The first reported human antimicrobial protein, lysozyme², was inquisitively discovered by Alexander Fleming in 1922, six years before Fleming’s penicillin breakthrough. In light of that, penicillin and the ‘Golden Age of antibiotics’ overshadowed the thorough research in the therapeutic potential of natural AMPs. Notwithstanding, the raise of conventional antibiotics resistance by microbial pathogens, which is leading humankind on the threshold of a post-antibiotic era unless new drugs and alternative therapies are discovered, awakened the interest in AMPs host defense molecules.

Although neutral and anionic antimicrobial peptides have been reported, the majority of AMPs have a net positive charge^{3,4}. Cationic peptides roughly consist of between 10 and 50 amino acid residues rich in both basic and hydrophobic side chains that align in three dimensions on opposing faces. Thus, AMPs fold as unique amphipathic structures, with both positively charged and hydrophilic cores, that increases peptides solubility in water. Folded AMPs can be classified into four groups, according to their secondary structure^{5,6}. β -conformations, stabilized by internal disulfide bonds, found in batenecins and defensins; amphipathic α -helices, especially folded in non-polar environment such as the bacterial membrane, found in cecropin⁷ and magainin⁸; extended rich-proline helices as in indolicidin⁹; loop structures, formed by a single internal disulfide bond, as in gramicidin S¹⁰.

The increasing attractiveness in AMPs for clinical developments stems from their selectivity, their speed of action and the little likelihood to bacteria develop resistance mechanisms against them. True though it is, there are yet potential problems to overcome as the high production costs, toxicity against eukaryotic cells, and proteolytic degradation. However, despite these drawbacks, some antimicrobial peptides are already in clinical and commercial use, such as ampicillin, polymyxin B and gramicidin S¹¹.

1.1. Mechanism of action

The basis of antimicrobial peptides specificity to bacteria membranes stems from the difference between the composition and organization of cell membranes in eukaryotic and prokaryotic organisms. Unlike eukaryotic cell membranes, whose outer leaflet is exclusively constituted by zwitterionic phospholipids, the outermost leaflet of prokaryotic bilayers is assembled by negatively charged phospholipids. Conversely, in both animal and vegetal membranes, negatively charged headgroups are segregated into the inner leaflet¹², facing the cytoplasm. Furthermore, their membranes are abundant in sterols which contribute to the resistance against antimicrobial peptides¹³.

The interaction between AMPs and bacterial membranes is fundamental to their antimicrobial activity. According to the Shai-Matsuzaki-Huang (SMH) model¹⁴, peptide-membrane interactions cause the displacement of lipids, alteration of membrane structure and in some cases entry of the peptide into the target cell cytosol. From this schematic mechanism, many studies have presented several reasons why AMPs are capable to kill microbes such as fatal depolarization of the normally energized bacterial membrane¹⁵, creation of membrane pores by which cellular contents leak out¹⁶ or the induction of hydrolases that degrade the cell wall¹⁷.

Notwithstanding, the most abundant mechanism by which antimicrobial peptides permeates membranes is through pore formation. The explanation of this mechanism falls into three categories: barrel-stave model, toroidal pore model and carpet-like model (**Figure 1**).

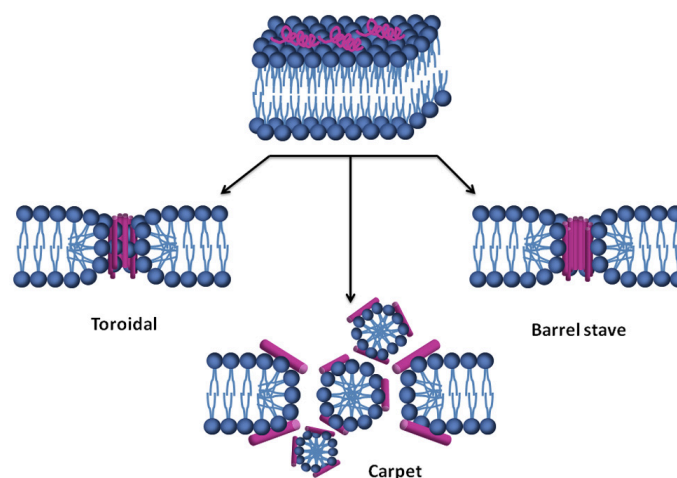


Figure 1: Modes of lipid membrane permeabilization by AMPs (from Silva *et al.*)¹⁸.

The barrel-stave model¹⁹ was the first pore induction mechanism to be actually proposed for antimicrobial peptides. The pore formation by this model occurs in three steps. First, peptides interact with the membrane surface, probably in the form of monomers. Second, peptides transit from a random coil organization to a well-defined secondary structure, which displaces the polar headgroup of the phospholipids and consequently promotes the bilayer thinning in that region. Thus, whereas the hydrophilic residues lie besides the headgroups, hydrophobic peptide sidechains insert into the hydrophobic core of the membrane. In the third and last step, monomers aggregate (oligomerization) and insert deeply in the membrane forming a pore. However, to occur the oligomerization it is necessary a monomer concentration threshold and a minimum exposure of the hydrophilic residues in the hydrophobic core, since peptides adopt transmembrane orientations.

Studies with α -helical peptides, such as magainin and PGLa, led to the toroidal pore model^{19,20}. Likewise the barrel-stave pore, the toroidal pore formation occurs in three steps. Initially, peptide molecules in the extracellular medium interact with the negatively charged membranes from microorganisms, transitioning from a random coil to an α -helical structure, which is oriented parallel to the surface of the bilayer. This interaction, followed by a conformational transition, disrupts membrane integrity. Henceforth, at a peptide-lipid ratio threshold, which varies for each AMP, peptide α -helices transit from the parallel orientation (inactive state) to a perpendicular orientation (active state) penetrating the hydrophobic region of the bilayer and, together with some lipid molecules, they adopt a multipore transitional state known as a supramolecular dynamic complex. As a result, some peptides may move inward the inner leaflet of the bilayer or even the cytosol. Therefore, the toroidal pore model might be the key mechanism for peptides to enter inside the microbial cytoplasm and access potential intracellular targets. Finally, unlike the pore formed by the barrel-stave model, the toroidal pores are made of peptides interspersed with lipids; hence, this structure has been referenced as representation of a pore formed by the membrane itself, which is coated with the polar surface of the peptides in interaction with groups of phospholipid heads.

The carpet-like model²¹ is featured by the surfactant action of peptides as means of membrane permeabilization in a relatively diffuse way. Cecropin and indolicidin are examples of AMPs that perform their activity through this mechanism²². The cationic AMPs first bind to the membrane surface via electrostatic interactions. Thus, the layer of peptide monomers in the outer leaflet destabilizes the packaging of the bilayer since the displacement of phospholipids

modifies the fluidity of the membrane and mitigates its barrier effectiveness. Reached a certain peptide concentration threshold, the membrane becomes energy-deficient, which culminates in the loss of its integrity, leading to the formation of micellar structures. From this perspective, the dissolution of the membrane occurs in a dispersion-like manner, which does not involve the formation of a pore neither do the peptides necessarily fit into the hydrophobic interior of the membrane.

Last but not least, it has also been reported that some membranolytic peptides are inquisitively able to interact with intracellular targets when used in subinhibitory concentrations without breaking membranes' integrity^{23,24}.

1.2. Mimetic membrane models

Due to the great complexity of biological membranes, several simplified systems have been developed to mimic the lipidic layers of the cell membranes, in order to enable biophysical approaches to investigate the mechanism of action of antimicrobial peptides. In this work we have used both mechanically oriented phospholipid bilayers and large unilamellar vesicles (LUVs).

Supported (mechanically oriented) phospholipid bilayers are one kind of membrane biomimetic model, which consists of lipid bilayers supported by a solid surface, such as glass or mica. One of the great advantages of supported beds is their stability, which allows the samples to last for weeks or even months²⁵. These systems typically not only allow the investigation of peptide interactions with phospholipids, but also predict the phase behavior and parallel organization of the molecules that compose the membrane. These systems can be easily prepared either by melting lipidic vesicles or by the depletion of surfactants from micelle solutions composed of a mixture of surfactants and phospholipids. Unlike phospholipid vesicles, which are free in solution, the supported lipidic bilayers are much easier to characterize and monitor by being fixed on the surface of a solid support. Therefore, a whole host of surface-sensitive techniques can be used for their characterization, such atomic force microscopy (AFM), X-Ray reflectivity, surface plasmon resonance (SPR) and solid-state nuclear magnetic resonance (NMR) spectroscopy, among others.

On the other hand, liposomes are the most popular biomembrane model due to their versatility. Liposomes are composed of leaflets, which are arranged in a similar way to biological

membranes. This set of phospholipids contains an internal hydrophilic surface and is organized by the spontaneous association among all the hydrophilic tails of phospholipids in an aqueous dispersion. This type of aggregate tends to rapidly reorganize forming multilamellar vesicles (MLVs), which are structures with greater thermodynamic stability. However, unilamellar vesicles are easily prepared from MLV suspensions in a controllable manner. Among all kinds of liposomes, LUVs are the most widely used in membrane-AMPs studies. The membrane permeability activity caused by AMPs can be estimated by using liposomes containing phospholipids from both Gram-negative and -positive bacteria membranes, carrying some fluorescent molecules such as calcein or carboxyfluorecein²⁶.

In this work, four kinds of lipids (**Figure 2**) have been used to create both oriented phospholipid bilayers and LUVs to investigate the membrane interactions of peptides and glyctoriazole-peptides. These lipids are: 1-palmitoyl-2-oleoyl-*sn*-glycero-3-phosphocoline (POPC), 1-palmitoyl-2-oleoyl-*sn*-glycero-3-(phospho-*rac*-(1-glycerol)) (POPG), 1-palmitoyl-2-oleoyl-*sn*-glycero-3-phospho-L-serine (POPS) and ergosterol.

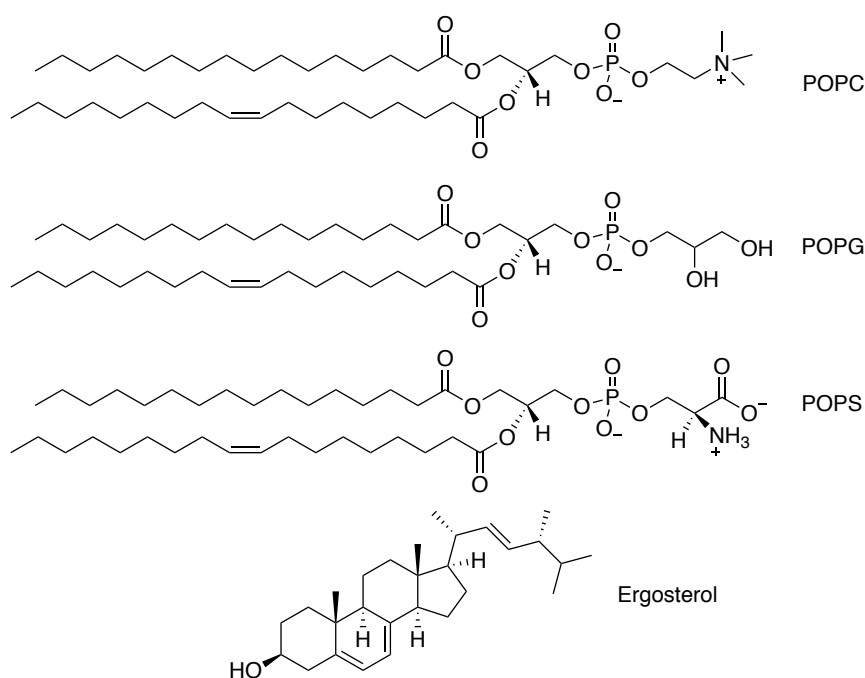


Figure 2: Chemical structure of the lipids used in the preparation of supported bilayers and LUV.

1.3. Background of the molecules studied in this master's thesis

Ocellatins are a family of antimicrobial peptides, which has been isolated from the skin secretions of anurans of the *Leptodactylus* genus²⁷⁻²⁹, usually found in the tropical forests of South America and Antilles. Recently, three of these peptides, namely ocellatin-LB1, -LB2 and -F1 (Oce-LB1, -LB2 and -F1) have been isolated from the skin secretion of the frog species *Leptodactylus labyrinthicus* (Table 1)²⁶.

These molecules are naturally amidated at their C-termini and their primary structures are identical from residues 1 to 23 (Oce-LB1 sequence), whereas Oce-LB2 carries an extra Asn and Oce-F1 extra Asn-Lys-Leu residues at their C-termini. In spite of having similar primary structures, these extra amino acids ensure different membrane interactions as well as different antimicrobial potentials (-F1 >>, -LB1 ≥ -LB2), as proved by several biophysical approaches and biological assays^{26,30}.

When the primary and secondary structures of these three Ocellatins are compared to each other, the antimicrobial character is directly correlated to the helical degree, hemolytic activities and membrane-disruptive properties. Besides presenting significantly smaller minimal inhibitory concentrations (MIC) compared to the other two peptides, Oce-F1 at 6.28 mM promotes 98 % dye release from calcein-loaded phospholipid vesicles, whereas -LB1 and -LB2 at concentrations near 20 mM promote only 48 % dye release. Overall, these results confirm that the extra Asn-Lys-Leu promote stronger peptide-membrane interactions and higher antimicrobial activities for Oce-F1, whereas the extra Asn-23 decreases the antimicrobial potential and membrane affinity of Oce-LB2²⁶ (Table 1).

Table 1: Primary structures and membrane disruptive properties of three ocellatins

Peptide	Sequence	Hemolytic Activity (%) ^{(a)*}	Dye Release (%) ^{(b)*}	Antimicrobial Activity ^{(c)*}		
				Gram-Negative	Gram-Positive	Fungi
Oce-LB1	GVVDILKGAAKDIAGHLASKVM-NH ₂	6	48.5	2	0	2
Oce-LB2	GVVDILKGAAKDIAGHLASKVMN-NH ₂	1	30	1	0	0
Oce-F1	GVVDILKGAAKDIAGHLASKVMNKL-NH ₂	13	96	2	1	1

^(a) Hemolytic activity in rabbit erythrocytes at 1000 µg·mL⁻¹ peptide concentration. ^(b) Calcein release promotion at peptide concentrations near 20 mM for both Oce-LB1 and -LB2 and 6.28 mM for Oce-F1 in POPC vesicles. ^(c) Number of microorganisms in which ocellatins showed antimicrobial activity. For each microorganism, two different strains were tested. *Data obtained by Gusmão, *et al.*, 2017²⁶

Two-dimensional solution-state NMR spectroscopy was used to determine the three-dimensional structures of these peptides in different membrane mimetic environments and well-defined α -helices have been observed in all cases³⁰. These high-resolution structures provide a useful prerequisite to investigate in detail the dynamics and topology of these closely related sequences in phospholipid bilayers³¹. Henceforth, one of the focuses of this work is to assess the topological differences among Oce-LB1, -LB2 and -F1 by ¹⁵N and ²H solid-state NMR spectroscopy using samples containing the selectively labelled peptides reconstituted into oriented 1-palmitoyl-2-oleoyl-*sn*-glycero-3-phosphocholine (POPC) bilayers. Besides, we have also performed ITC and SPR experiments to get extra information on how the extra amino acids near the C-terminus influence both thermodynamics and kinetics of the peptide-membrane interactions.

Two other molecules that this work aims to study are peptide derivatives known as Glycotriazole-peptides (GtP), not least glycotriazole-hylaseptin-P1 ($[p\text{-Glc-trz-A}^1\text{]-HSP1-NH}_2$) and glycotriazole-phyloseptin-2 ($[p\text{-Glc-trz-A}^{14}\text{]-PS-2}$). These derivatives are a new class of molecules which has recently been proposed and studied in partnership between our research group and Rodrigo Verly's group from Universidade Federal dos Vales do Jequitinhonha e Mucuri (UFVJM).

Hylaseptin-P1 (HSP1) was originally isolated from the anuran *Hyla punctata*, commonly found in the wet areas of the Brazilian north and northeast regions³². The wild-type peptide is composed of 14 amino acids (GILDAIKAIKAAG) and carries no modification on its primary structure. It shows no significant hemolytic activity and mild activity against *Candida albicans*, *Staphylococcus aureus*, *Escherichia coli* and *Pseudomonas aeruginosa*. For that reason, Eduardo F.C. Junior and collaborators chose this antimicrobial peptide as a scaffold for chemical modifications to assess the effect of glycosylation and triazolation³³ on the antifungal activity of this peptide. These GtP were also prepared with amidated C-termini, since this modification is known to increase antimicrobial activity³⁴⁻³⁶.

Three derivatives of HSP1 were prepared by the insertion of a single triazole ring to obtain $[\text{trz-A}^1\text{]-HSP1-NH}_2$ or by the insertion of distinct glycotriazole moieties to obtain $[p\text{-Glc-trz-A}^1\text{]-HSP1-NH}_2$ and $[p\text{-GlcNAc-trz-A}^1\text{]-HSP1-NH}_2$ (**Figure 3**).

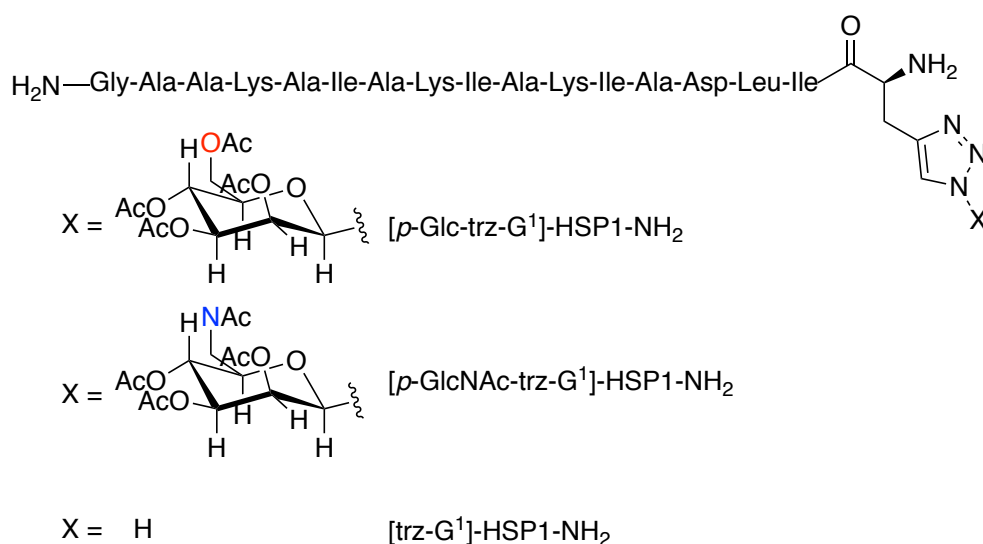


Figure 3: Modifications of HSP1 peptide previously studied by Eduardo F.C. Junior *et al.*

Biological assays had higher antifungal activities for these three derivatives in comparison to HSP1-NH₂ due to the inhibition effects on ergosterol biosynthesis. Notwithstanding, antifungal activities are greater for the glycotriazole-peptides when compared to the triazole derivative. These results are also in accordance with biophysical assays, such as dynamic light scattering (DLS), Zeta potential measurements, surface plasmon resonance (SPR) and carboxyfluorescein leakage from phospholipid vesicles, which indicate that the carbohydrate moiety ensures stronger membrane interactions for the GtP derivatives³³. Thus, glycotriazole-HSP1 derivatives present higher membrane disruption properties, lytic activities and stronger peptide-LUVs interactions when compared to the triazole derivative and to HSP1.

Phylloseptins (PS) are antimicrobial peptides found in the skin secretions of the *Phyllomedusa* genus (anura), tree frogs that inhabit the tropical forests of South and Central Americas³⁷. From the viewpoint of structure-function relationship, these C-terminus amidated peptides exhibit a high degree of similarities within their N-terminal domains but a high degree of variation in the last six residues. Phylloseptins show a direct correlation between their degree of helicity and their antimicrobial activities against both Gram-positive and -negative bacteria³⁸, in the order PS-2 > PS-1 > PS-3. In this work, however, we are interested in the study of peptide-membrane interaction topology of [p-Glc-trz-A¹⁴]-PS-2-NH₂ since biophysical assays showed that the glycotriazole residue does not enhance peptide's affinity for membranes but, inquisitively, increases its antifungal activity³⁹. Two-dimensional solution-state NMR spectroscopy was used to determine the three-dimensional structure of this GtP in zwitterionic and anionic membrane mimetic environments and well-defined α -helices have been observed in both cases⁴⁰. These

high-resolution structures provide a useful prerequisite to investigate in detail the membrane topology of this GtP reconstituted in phospholipid bilayers. Henceforth, the other focus of this work is to assess the role that the glycotriazole moiety plays in the topology of [*p*-Glc-trz-A¹]-HSP1-NH₂ and [*p*-Glc-trz-A¹⁴]-PS-2 reconstituted into oriented phospholipid bilayers by ¹⁵N and ²H solid-state NMR spectroscopy.

Chapter 2: Solid-Phase Synthesis of Peptides and Glycotriazole-Peptides

2.1. Introduction

2.1.1 Peptide solid-phase synthesis

The importance of peptide synthesis lies in the ability to incorporate unnatural amino acids and in the production of large quantities of pure peptides. In light of that, solid-phase peptide synthesis (SPPS) was one of the major breakthroughs in peptide chemistry, bestowing the Nobel Prize in Chemistry upon Robert Bruce Merrifield in 1984. In contrast to the peptide synthesis in solution, in which the product has to be isolated after each coupling reaction and purified before the next step, the growing peptide in the solid-phase strategy is linked to an insoluble polymeric support and as a consequence the byproducts are simply removed by filtration or washing after each reaction step. In addition, the whole host of polymeric supports that has been developed nowadays enables the synthesis of all kind of peptides according to their C-terminal nature (**Figure 4**). For instance, Wang resin is used for the synthesis of carboxylated peptides and Rink amide is used to obtain carboxamidated peptides (all peptides prepared in this work are carboxamidated)⁴¹.

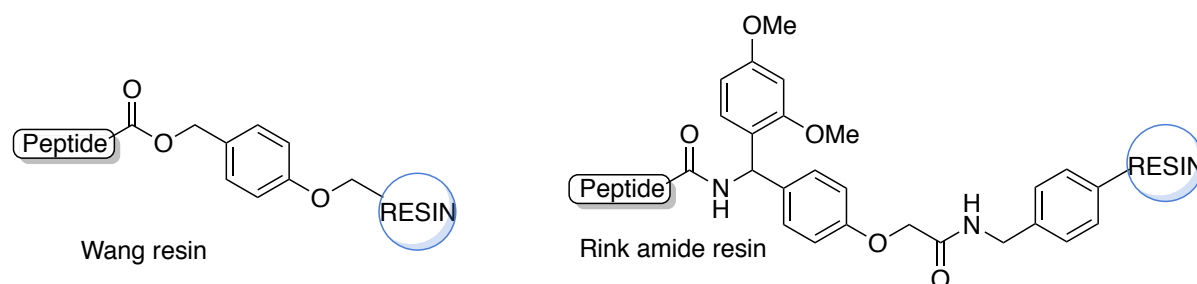


Figure 4: Examples of polymeric supports according to the desired C-terminal nature of peptides.

Fmoc-strategy in solid-phase synthesis is based on an orthogonal protecting group approach, using the base-labile 9-fluorenylmethyloxycarbonyl (Fmoc) group for the protection of α -amino group and acid-labile sidechain protecting groups and resin-linkage agents. Hence, whereas the removal of the *N*-Fmoc protecting group is usually achieved by treatment with piperidine 20-50% v/v in DMF, *tert*-butyloxycarbonyl (Boc) and other acid-labile groups are generally removed by trifluoroacetic acid (TFA). The key step of this reaction is the initial

deprotonation of the fluorene ring to generate the aromatic cyclopentadiene-type intermediate. Eventually, this intermediate is rapidly eliminated to form dibenzofulvene which is scavenged by piperidine (**Figure 5**)

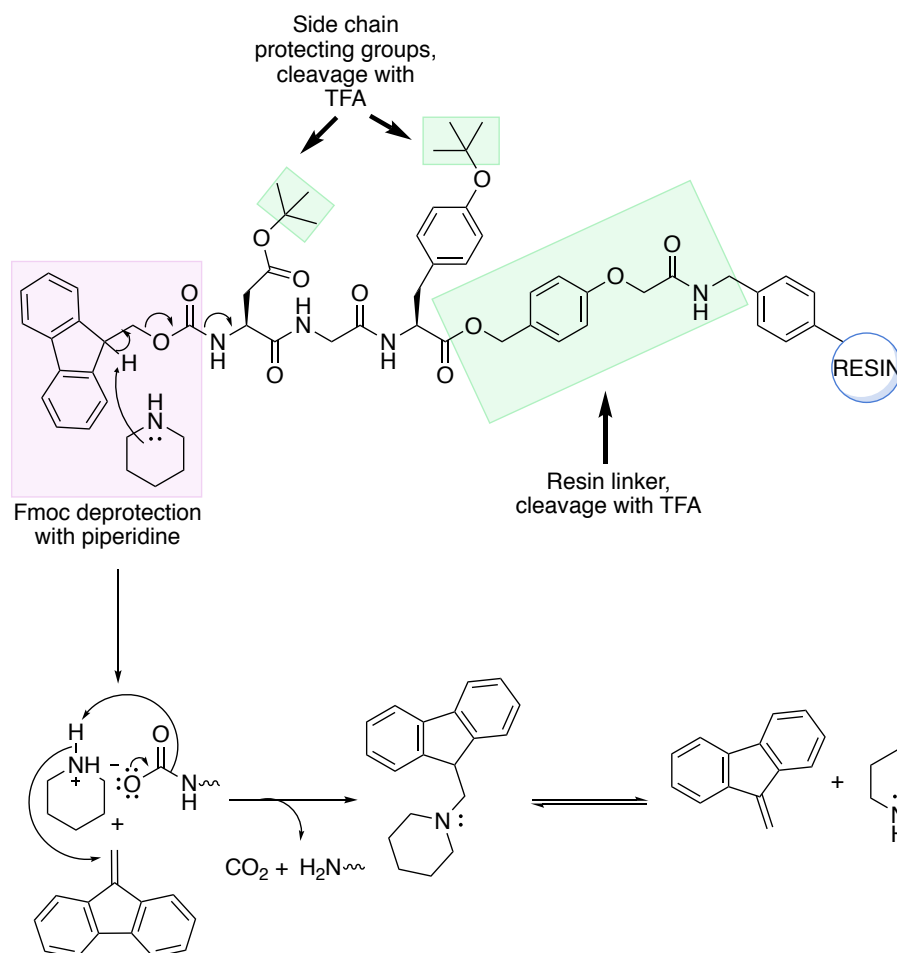


Figure 5: Orthogonal protecting group approach and Fmoc removal with piperidine (adapted from Kimmerlin *et al.*, 2004)⁴¹.

Fmoc-strategy in solid-phase synthesis^{41,42} (**Figure 6**) starts with the cleavage of Fmoc group from the resin under the same basic conditions stated above. In order to couple the first Fmoc-amino acid derivative to the resin, the carboxyl group must be activated and reagents such as DIC/HOBt or phosphonium salts may be used among other. Once the amino acid is activated, the coupling reaction with the free amino group of the resin takes place under constant stirring conditions. In order to carry out the next coupling with another Fmoc-amino acid derivative, the deprotection step of the amino acid bound to the resin and the activation step of the Fmoc-amino acid to be coupled must be brought forth before. Thereafter, the coupling reaction is carried out and yields a resin bound dipeptide which is Fmoc-protected at the N-terminus. Further deprotection and coupling steps are then successively performed until the desired resin

bound peptide sequence is obtained. After all these steps, one last deprotection of the amino group is performed under basic conditions and the removal of the acid-labile side-chain protecting groups as well as the peptide cleavage from the resin are finally carried out under acid conditions⁴². At the end of the synthesis, the peptide is then precipitated, lyophilized and purified by HPLC.

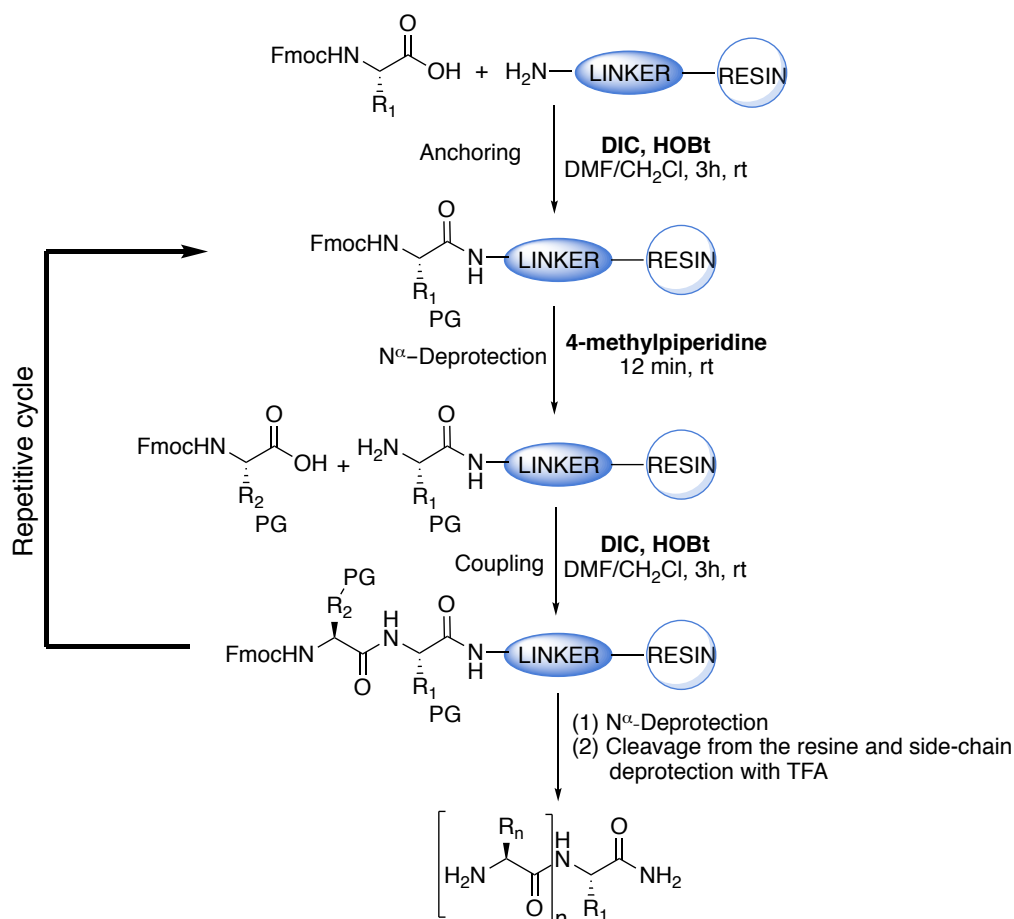


Figure 6: Schematic representation of the principles of solid-phase peptide synthesis.

In this work the activation of carboxyl group has been done by using 1,3-di-isopropyl-carbo-di-imide (DIC) and 1-hydroxy-benzotriazole (HOBt) in dimethylformamide (DMF). Thus, carboxyl group first attacks to the electron deficient DIC, followed by a reaction coupling with HOBt that leads to the release of a carbamide and the formation of the active ester (**Figure 7**). Thereafter, the coupling reaction occurs due to the attack from peptidyl-resin to the carbonyl of the active ester.

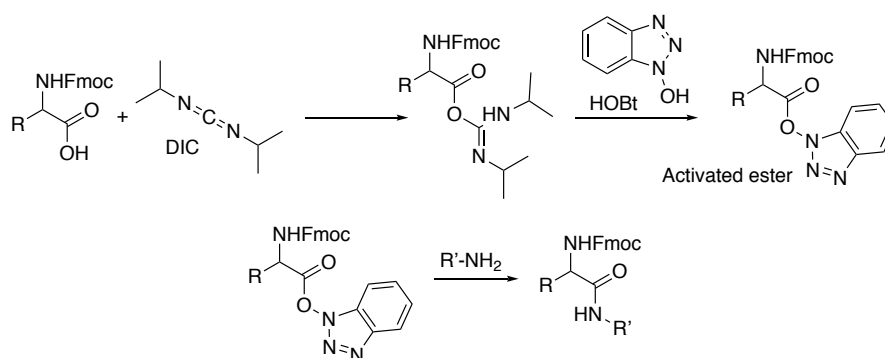


Figure 7: Activation of the carboxyl group with DIC/HOBt and coupling reaction.

Kaiser's test⁴² is used to monitor whether the coupling or *N*-Fmoc amine deprotection are completely yielded. This test consists of the reaction between ninhydrin and a free amine to yield Ruhemann's purple. Thus, if the *N*-Fmoc amine deprotection is successfully achieved, the colorless solution will turn blue-purple due to Ruhemann's product whereas it is supposed to remain colorless for successful coupling steps (**Figure 8**).

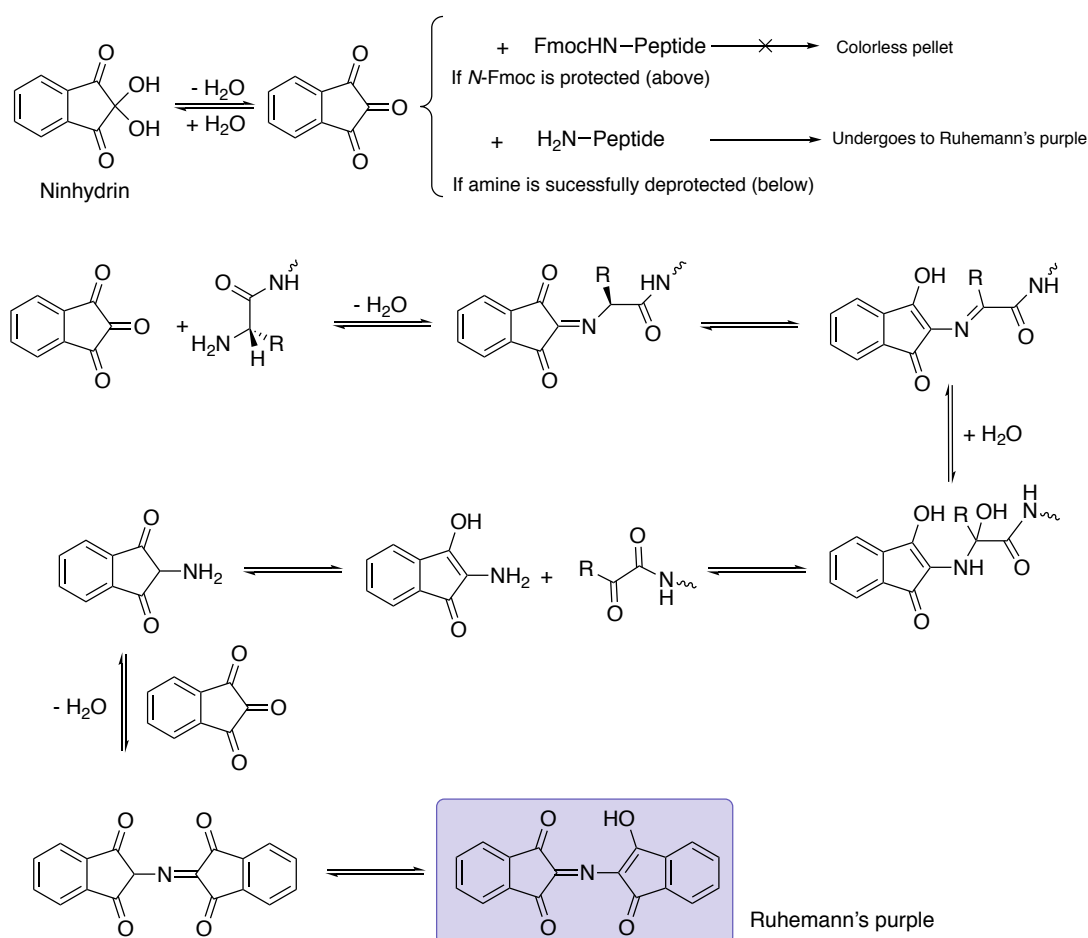


Figure 8: Schematic representation of Kaiser's test and reaction mechanism between free amino groups and ninhydrin.

2.1.2. Copper(I)-catalyzed alkyne-azide cycloaddition

On the cutting-edge of synthesis, “click” chemistry sprung as an efficient approach to bind two molecular building blocks together on a sustainable basis by using mild-water tolerant conditions, either avoiding or mitigating byproducts and increasing both selectivity and yield⁴³. The most used “click” reaction, which meets with success these conditions, is by all odds the Cu^I-catalyzed azide/alkyne cycloaddition (CuAAC).

The first strategy to synthesize 1,2,3-triazoles from azide/alkyne reaction was reported in 1893, known as the Huisgen reaction. However, this reaction produces a mixture of 1,4 and 1,5-disubstitution products. Conversely, the CuAAC reaction of terminal alkynes is completely regioselective in the formation of 1,4-disubstituted triazoles with a great deal of Cu^I catalysts^{44,45} (**Figure 9**)

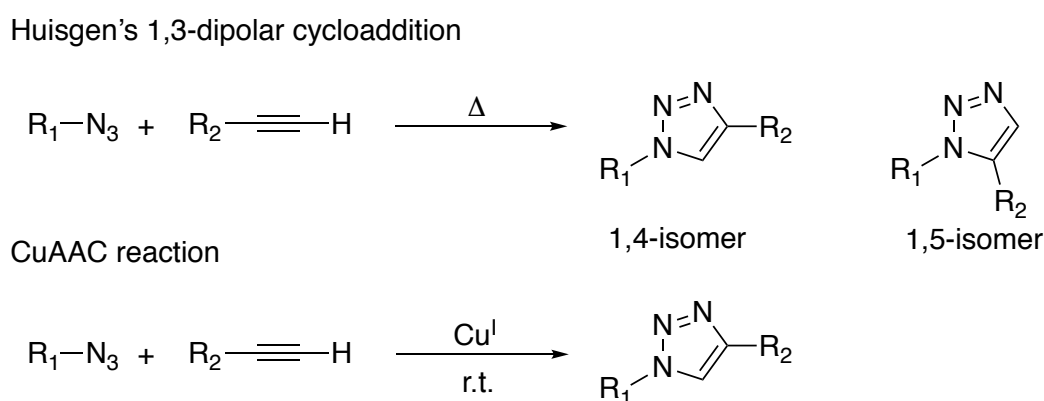


Figure 9: Schematic comparison of Huisgen's reaction and CuAAC reaction.

The most common method to generate Cu^I species and trigger the reaction is by using Cu^{II} salts as pre-catalyst, usually from CuSO₄, together with a reducing agent, usually sodium ascorbate. Thus, it is proposed that alkyne coordinates to Cu^I to form the π -alkyne-Cu^I intermediate. DFT and kinetic studies^{46,47} have shown that the alkyne coordination to Cu^I reduces its pK_a by 9.8 pH units, which makes water a strong enough base to deprotonate the π -alkyne-Cu^I intermediate and form the σ -alkynyl-Cu^I species. A bimetallic structure is then generated because of the π -complexation of the σ -alkynyl-Cu^I species which decreases the electron density on the *sp* carbon atoms⁴⁷. Hence, the σ -bound copper acetylide bearing a π -bound copper coordinates the azide forming an unusual six-membered copper metallacycle, in which the second copper atom acts as a stabilizing donor ligand. Finally, ring contraction to triazolyl-copper derivative is

followed by protonolysis that yields the triazole product and closes the catalytic cycle⁴⁸ (**Figure 10**).

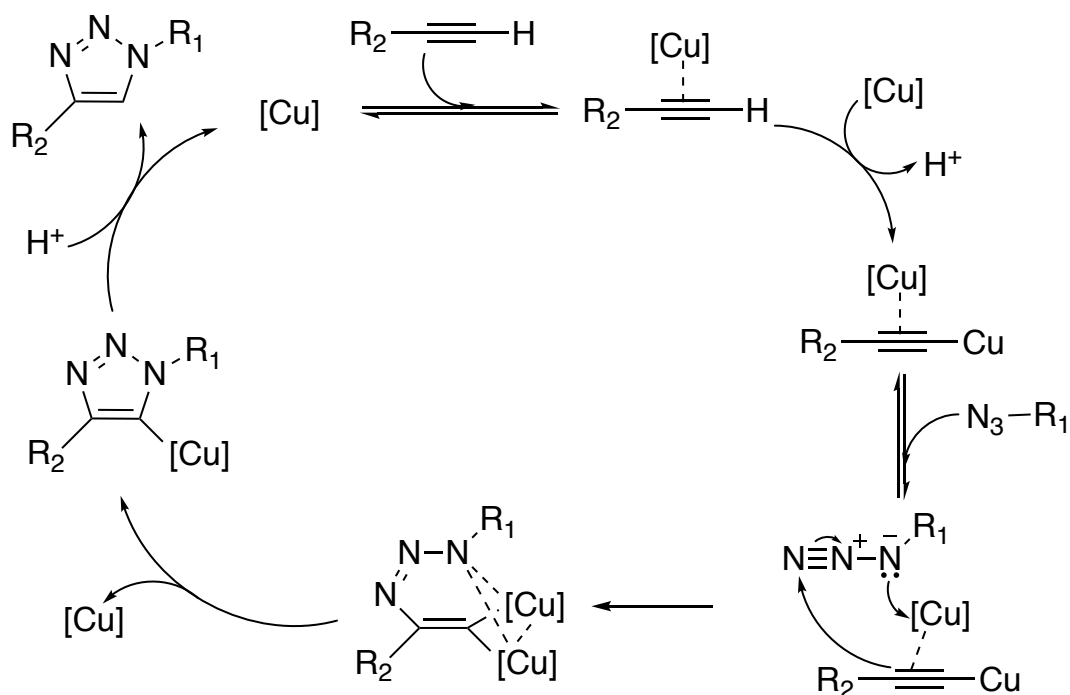


Figure 10: Mechanism of the Copper-catalyzed Azide-Alkyne Cycloaddition (CuAAC) involving a dinuclear Copper intermediate.

In conclusion, several applications have been described for CuAAC, as in classic organic synthesis as well as in the synthesis of dendrimers and polymers. However, the glycotriazolization of natural antimicrobial peptides from the reaction between azide per-*O*-acetylate-glucose derivatives and alkyne-decorated peptidyl-resin has recently been described³³. Thus, not only have these synthetic modifications by this approach led to great yields of glycotriazole-peptides, but also to an enhancement of their antifungal activities.

2.2. Objectives

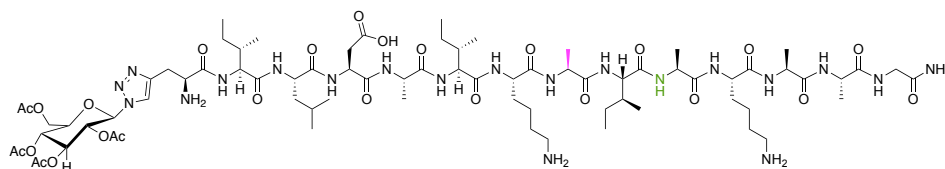
1. Synthesize (3,3,3-²H₃-Ala-10, ¹⁵N-Leu-17)-Oce-F1 peptide by Fmoc-SPPS strategy (Table 2)
2. Synthesize (3,3,3-²H₃-Ala-8, ¹⁵N-Ala-10)-[pOAcGlc-Trz-A¹]-HSP1 and (3,3,3-²H₃-Ala-8, ¹⁵N-Leu-15)-[pOAcGlc-Trz-A¹⁴]-PS-2 peptides by Fmoc-SPPS strategy along with copper(I)-catalyzed alkyne-azide cycloaddition (CuAAC) between the azide per-*O*-acetylate-glycose derivate and the propargyl glycine residue contained in the peptidyl-resin derivatives of HSP1-NH₂ ([Pra¹]HSP1-NH₂-peptidyl-resin) and PS-2 ([Pra¹⁴]PS-2-peptidyl-resine) (Table 2, Figure 11)

Table 2: Primary structure and labeled sites of ocellatins and glycotriazole-peptides

Peptide	Sequence
(3,3,3- ² H ₃ -Ala-10, ¹⁵ N-Leu-17)-Oce-LB1	GVVDILKGA <u>AK</u> DIAGHL <u>ASK</u> VM-NH ₂
(3,3,3- ² H ₃ -Ala-10, ¹⁵ N-Leu-17)-Oce-LB2	GVVDILKGA <u>AK</u> DIAGHL <u>ASK</u> VMN-NH ₂
(3,3,3- ² H ₃ -Ala-10, ¹⁵ N-Leu-17)-Oce-F1	GVVDILKGA <u>AK</u> DIAGHL <u>ASK</u> VMNKL-NH ₂
(3,3,3- ² H ₃ -Ala-8, ¹⁵ N-Ala-10)-[pOAcGlc-Trz-A ¹]-HSP1	A*ILDAIK <u>AI</u> AKAAG-NH ₂
(3,3,3- ² H ₃ -Ala-8, ¹⁵ N-Leu-15)-[pOAcGlc-Trz-A ¹⁴]-PS-2	FLSLIPH <u>AI</u> NAVSA* <u>L</u> VHHF-NH ₂

-NH₂ indicates C-terminal carboxamide; pOAcGlc indicates *D*-Glucose per-*O*-acetylated; trz indicates 1,4-disubstituted triazole ring; ¹⁵N labelled sites are underlined and ²H₃-Ala labelled sites are doubly underlined

[pOAcGlc-Trz-A¹]-HSP1-NH₂



[pOAcGlc-Trz-A¹⁴]-PS2

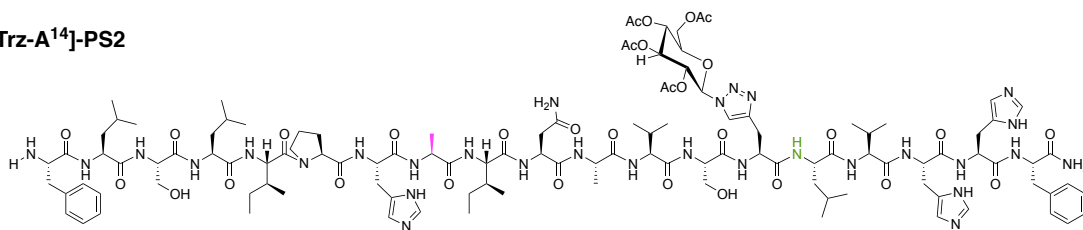


Figure 11: Chemical structure of both [pOAcGlc-Trz-A¹]-HSP1-NH₂ and [pOAcGlc-Trz-A¹⁴]-PS-2 peptides. ¹⁵N labelled sites are in green and ²H₃-Ala labelled sites are in pink.

2.3. Methods

2.3.1. Synthesis of selectively labeled (3,3,3-²H₃-Ala-10, ¹⁵N-Leu-17)-Oce (-LB1, -LB2 and -F1)

C-terminus amidated ocellatins (**Table 2**, p. 29) were obtained by solid-phase synthesis on a Rink-amide AM resin (Irish Biotech, Marktredwitz, Germany) (0.4 mmol/g) by using the Fmoc-strategy. All amino acids, unlabeled (Irish-Biotech, Marktredwitz, Germany) and labeled (CIL, Andover, MA, USA), were *N*^α-Fmoc protected whereas side-chain groups were protected by acid-labile protecting groups.

Resin was weighted, as well as all protected amino acids, in a Metler AE 163 balance with a precision of 0.1 mg. Thereafter, the resin was transferred to a syringe, provided with a piston and filter, whereby the synthesis was carried out.

N^α-Fmoc deprotections were carried out by using a solution of 4-methylpiperidine (PIPE) 20% v/v in previously distilled *N,N'*-dimethylformamide (DMF) (Vetec, PA). Couplings were performed with 4 equivalents of protected amino acids, DIC (Fluka) and HOBt (NovaBiochem-Merck) in 3.0 mL of a mixture of previously distilled DMF and chloroform (2:1) stirring the syringe during 120 min. Moreover, peptidyl-resin was washed three times with DMF and isopropanol (IPA), once with dichloromethane (DCM) and finally dried under vacuum after each step of *N*^α-Fmoc deprotection and coupling²⁶.

Kaiser's test was used to monitor both deprotection and coupling reactions. To perform this test, around 5-6 grains of peptidyl-resin were taken after each washing step and mixed with the following solutions in 1:2:1 volume-proportion:

1. Piperidine 2% v/v in aqueous solution of KCN 1 mM.
2. Aqueous solution of phenol 80%.
3. Ninhydrin 5% v/v in ethanol.

Thereafter, the mixture was heated up to 100 °C for 5 minutes⁴⁹. If the resin remained colorless, the coupling was yielded or the *N*^α-Fmoc deprotection reaction was unafforded. Otherwise, if the resin went purple the coupling was not yielded but *N*^α-Fmoc deprotection was. All these steps explained above were repeated until the desired peptidyl-resin was obtained.

The cleavage of the peptide from the resin and the deprotection of the sidechain protecting groups was carried out under strong acid conditions, using 3.0 mL solution of trifluoroacetic acid (TFA), Milli-Q water, 1,2-ethanedithiol (EDT) and triisopropylsilane (TIS) in 94:2.5:2.5:1 proportion. It is important to emphasize the use of TIS as an ionic scavenger to avoid by-products due to the release of carbocations which stem from the deprotection of sidechains⁴². In addition, in the case of Oce-F1, which contains a methionine in its primary sequence, it is also important to use EDT to avoid thiol oxidation to disulfide.

The cleavage solution was sucked out by the syringe containing the peptidyl-resin and stirred for 180 minutes at room temperature. Thereafter, the reaction crude was transferred to a 50 mL Falcon™ tube and the syringe was washed with 1.0 mL of TFA, collecting the washing solution in the same tube. Then, solution was reduced to 3.0 mL by evaporation together with a continuous flow of gas nitrogen. Thus, the crude peptide was precipitated with 3 mL of freezing diisopropyl ether (Veter, PA), cold in liquid nitrogen and centrifugated at 5000 rpm for 4 min. The supernatant was removed with a pipette and the white solid was washed two more times by the same procedure until getting it in the minimum amount of water. Finally, the white solid was dissolved in the minimum amount of water, frozen in liquid nitrogen and lyophilized for 48 h in the Thermo ModulyoD lyophilizer.

2.3.2. Synthesis of selectively labeled Glycotriazole-peptides ($3,3,3\text{-}^2\text{H}_3\text{-Ala-8}$, $^{15}\text{N-Ala-10}$)-[pOAcGlc-Trz-A¹]-HSP1-NH₂ and ($3,3,3\text{-}^2\text{H}_3\text{-Ala-10}$, $^{15}\text{N-Leu-15}$)-[pOAcGlc-Trz-A¹⁴]-PS-2

The alkyne-decorated peptidil resins corresponding to the GtP derivatives of HSP1 and PS-2 (**Table 2** and **Figure 11**, p. 29) were prepared on a Rink-amide resin by the Fmoc-strategy, as mentioned above in section 2.3.1. The difference is related to the coupling of the Fmoc-L-propargyl-Gly-OH (Fmoc-Pra-OH) residue, which was performed with 1.5 equivalents of coupling reagents. The cleavage of both GtPs from the resin and the deprotection of the sidechain protecting groups was carried out using 3.0 mL solution of TFA, milli-Q water and TIS in 95:2.5:2.5 proportion. Due to their different chain lengths, the substitution degree of the resin for the syntheses of HSP1 and PS-2 derivatives were 0.57 and 0.52 mmol/g, respectively.

The key step for the synthesis of both glycotriazole-peptides^{33,39} is then characterized by the CuAAC reaction between the alkyne-decorated peptidyl-resin intermediate ([Pra¹]-HSP1-resin

and [Pra¹⁴]-PS-2-resin) and the respective per-*O*-acetylated azide derivatives of glucose (Figure 12).

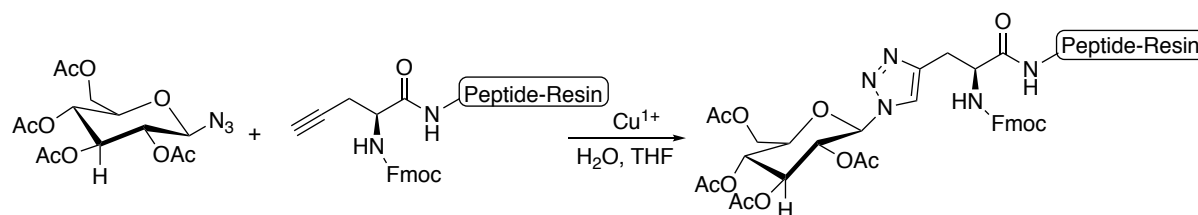


Figure 12: "Click" reaction between the azide per-*O*-acetylate-glucose derivate and the propargyl glycine residue contained in the peptidyl-resin derivatives.

CuAAC reaction was performed within the syringe for both peptides. The following three solutions were prepared:

1. Solution A: 2.4 mol of per-*O*-acetylate-glucose in 1.2 mL of THF.
2. Solution B: 0.5 mol of $\text{CuSO}_4 \cdot 5\text{H}_2\text{O}$ in 100 μL of Milli-Q water.
3. Solution C: 0.6 mol of sodium ascorbate in 200 μL of Milli-Q water.

Each solution was sucked out by the syringe as listed above and the system was stirred for 48 h. Peptidyl-resins were washed three times with 3.0 mL of THF, 3.0 mL of a solution containing 10% EDTA and 25% NH_4OH and, finally, in Milli-Q water in order to remove copper ions. The peptidyl-resins were then washed three times with DMF and isopropanol (IPA), once with dichloromethane (DCM) and finally dried under vacuum. Once glycotriazol-peptides were completely synthesized, cleaved and sidechain deprotected, both work-up and lyophilization were carried as described for the synthesis of selectively labeled ocellatins (section 2.3.1).

2.3.3. Purification

The purification of each peptide and GtP was carried out by HPLC (Varian, Inc.) on a ProStar 315 chromatograph equipped with a Waters $\mu\text{Bondapak}$ TM C18 reverse stationary phase 10mm (7,8 x 3mm) semi-preparative column, and UV-Vis detector and a Rheodyne[®] valve injection at (Laboratório e Síntese e Estrutura de Biomoléculas - LASEB- at the Universidade Federal dos Vales do Jequitinhonha e Mucuri). Each analysis was executed using linear gradients of two elution solutions: MilliQ water with TFA at 0.1% v/v, as solvent A, and acetonitrile (ACN) with TFA at 0.08% v/v as solvent B.

To determine the profile of each synthesis and the purification conditions, 1.0 mg/mL aliquots were prepared for each peptide and GtP. Thus, 100 μ L of each sample were injected at 1 mL/min flow rate from 0% of ACN to 100%. The detection was done by ultraviolet (UV-Vis) spectroscopy at $\lambda_{\text{max}} = 215$ nm. According to the respective analytical profile, each peptide derivative was set to its own purification conditions by adjusting the analysis time, flow and elution gradient. The protocol for the three ocellatins was the same as their analytical profiles and retention times were almost identical. The gradient used was from ACN 15% to 40% in 15 min and from ACN 40% to 55% in 15 min with 2 mL/min flow rate. On the other hand, both glycotriazole-peptides also showed similar analytical profiles despite the notorious difference between both sequences and the protocol used for both samples was: from 20% ACN to 45% in 15 min and from ACN 45% to 70% in 35 min at 2 mL/min flow rate.

Once the desired fractions were collected, ACN was removed under reduced pressure in a rotary evaporator. Thereafter, samples were dissolved in a 4.0% acetic aqueous (MilliQ water) solution and lyophilized in the Thermo ModulyoD lyophilizer. Finally, *Matrix-Assisted Laser Desorption/Ionization* (MALDI) coupled to time-of-flight (TOF) detector was used to confirm the identity of each peptide derivative.

However, as it will be discussed in *section 2.4*, mass spectra showed that some of the purified samples still contained some impurities and, in these cases (Oce-LB1, Oce-LB2, Gt-HSP1-NH₂ and Gt-PS-2), further purifications were performed using a similar protocol as described above at Université de Strasbourg, France. The purification was done by HPLC system (Gilson) with automatic collector and column Luna 5 μ m C18 100 Å reverse stationary phase (150 x 3000 mm) and 20 ml/min flow. The protocols used at University of Strasbourg were based on the results obtained at UFVJ. However, samples were centrifugated during 5 min at 10.000g to remove potential aggregates, instead of being filtered, and readjusted to a solvent gradient made of MilliQ water and ACN 9:1 acidified with TFA 0.1% v/v as solvent A and ACN acidified with TFA 0.08% as solvent B.

2.4. Results

2.4.1. Synthesis of selectively labeled peptide derivatives

The syntheses of ocellatins peptides were performed as described in *section 1.2.1*. After cleavage and lyophilization, all molecules were afforded as white powders and the following yields: Oce-LB1 95.02 mg, 63% yield; Oce-LB2 93.80 mg, 67% yield; Oce-F1 100.89 mg, 67% yield.

The syntheses of glycotriazole-peptides derivatives of HSP1 and PS-2 were carried out as described in *section 1.2.2*. Interestingly, during the CuAAC reaction step, the color of the solution inside the syringe changed to an intense brown color when the aqueous sodium ascorbate (solution C) was sucked in. This sudden change stems from the reduction of copper (II) to copper (I) due to ascorbate. However, the syringe containing [Pra¹]-HSP1-resin went orange whereas [Pra¹⁴]-PS-2-resin went black after leaving them in continuous stirring for 48h at room temperature. These abrupt changes in the color solutions were taken as a sign of the end of the CuAAC reaction and, therefore, the per-*O*-acetyl-glycosylation through triazole ring of both peptidyl-resin intermediates. Both GtPs were afforded as white powders in the following yields: [pOAcGlc-Trz-A1]-HSP1-NH₂ 120.68 mg, 80.4% yield; and [pOAcGlc-Trz-A14]-PS-2 20.0 mg, 11.1% yield.

The peculiarities of each coupling step are summarized on **Appendix 1**.

2.4.2. Purification of ocellatins

Purification of Ocellatin-F1, -LB1 and -LB2 was first carried out at Universidade Federal dos Vales do Jequitinhonha e Mucuri (UFVJM). All ocellatins showed similar analytical profiles (**Figure 13**).

Since the analytical run of Oce-LB1, -LB2 and -F1 crude samples presented similar profiles with a large number of components, a gradient of solvents was used to avoid large retention times, especially for Oce-F1 ($t_R = 33.83$ min). Thereafter, the elution time was adjusted to a 30 min and retention times of 24.76, 24.56 and 24.12 min were observed for ocellatin-F1, -LB1 and -LB2, respectively (**Figure 14**).

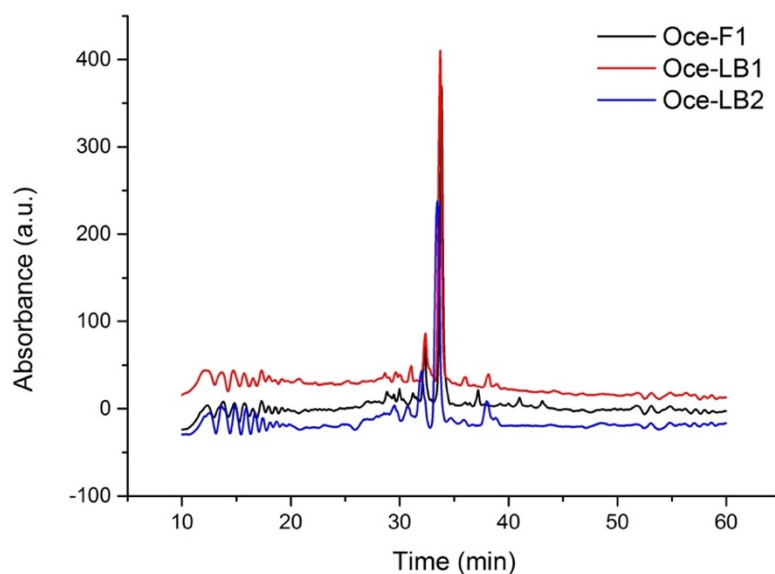


Figure 13: HPLC chromatograms obtained for Oce-F1 (black), Oce-LB1 (red) and Oce-LB2 (blue) analytical profiles, with a Waters μ Bondapak TM C18 reverse stationary phase 10mm (7.8 x 3mm) semi-preparative column.

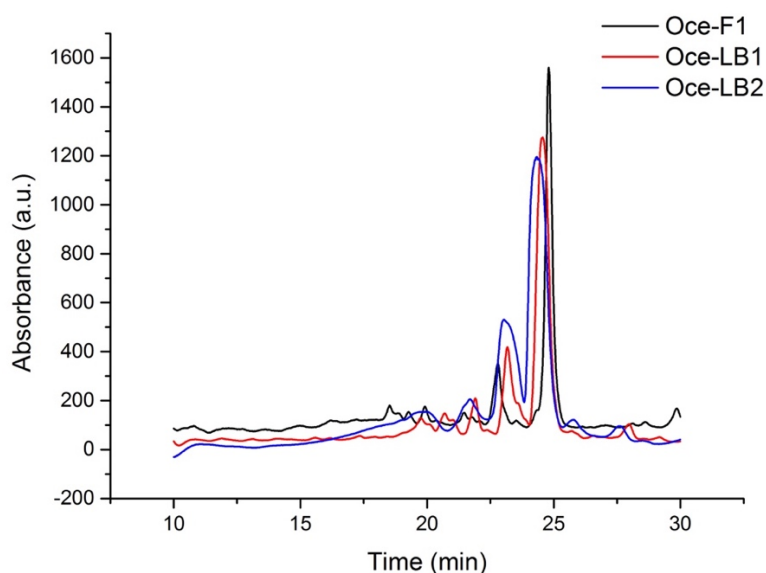


Figure 14: HPLC chromatograms obtained for Oce-F1 (black), Oce-LB1 (red) and Oce-LB2 (blue) purification, with a Waters μ Bondapak TM C18 reverse stationary phase 10mm (7.8 x 3mm) semi-preparative column.

After purification, each peptide was lyophilized and both identity and purity were verified by MALDI-TOF mass spectrometry. The purification of ocellatin-F1 was successful and a single specie was detected at m/z 2552.70 (theoretical value 2552.07). However, although the labelled derivatives of ocellatin-LB1 and -LB2 were also characterized (peaks at m/z 2197.62 and 2311.54, which correspond to theoretical values of 2196.63 and 2310.37, respectively), an extra peak corresponding to species $[MW + 163]$ were observed in the respective mass spectra (**Figure 15**).

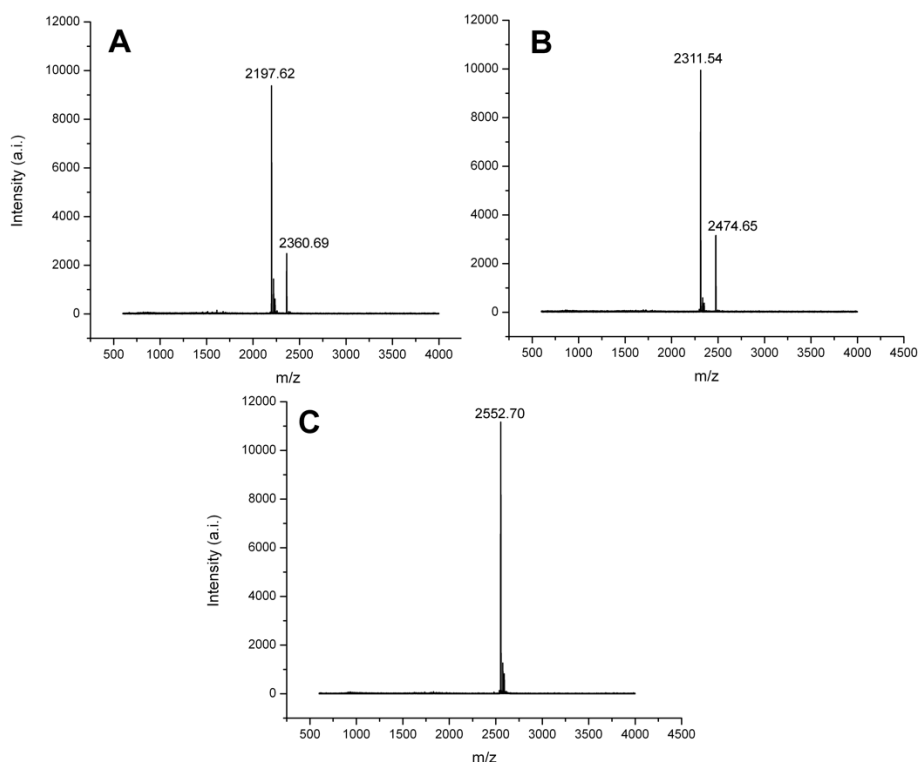


Figure 15: Mass spectra obtained by MALDI-TOF spectrometry for (A) Oce-LB1, (B) Oce-LB2 and (C) Oce-F1 after HPLC purification.

Due to the fact that the purification of both Oce-LB1 and -LB2 was unsuccessful, it was decided to further purify the leftover crude fractions at facilities of the Membrane Biophysics and NMR group of the Université de Strasbourg. Purifications were carried out by HPLC system equipped with an automatic collector. As can be seen in the respective chromatograms (**Appendix 2**), some impurities had retention times far close to peptides elution times ($t_R = 23.39$ min for Oce-LB2 and $t_R = 24.15$ min for Oce-LB1) what could make the purification laborious using not automated protocols. Thus, Oce-LB1, -LB2 and other fractions with intense peaks were collected and characterized by MALDI-TOF. Finally, both ocellatins were successfully purified (single specie at m/z 2196.676 for Oce-LB1 and m/z 2310.418 for Oce-LB2). Besides, it was also possible to isolate 0.6 mg of the [LB1 + 163] impurity and other impurities such as [LB1 – Asn], [LB1 – Val], [LB1 + O] and [LB2 + O] (**Appendix 3**).

In order to gain insight into the origin of the [LB1 + 163] impurity, ^1H , TOCSY, NOESY and NMR spectra of the impurity reconstituted in a TFE- d_2 : H_2O (60:40, v:v) solution were obtained under similar conditions as described in the literature for the pure unlabeled peptide³⁰. However, due to the rather small isolated amount of the impurity as to the relatively limited resonance dispersion and sensitivity of the spectrometer available (350 MHz for ^1H), the resolution and

signal-to-noise ratio of the obtained spectra were rather low. Notwithstanding, by comparing both (A) Oce-LB1³⁰ and (B) [LB1 + 163] ¹H-spectra (**Figure 16**) at the aromatic and amide region of the impurity, it is noteworthy the presence of a swamped singlet at 7.12 ppm and two doublets at 6.98 and 7.28 ppm for [LB1 + 163] which are absent for Oce-LB1.

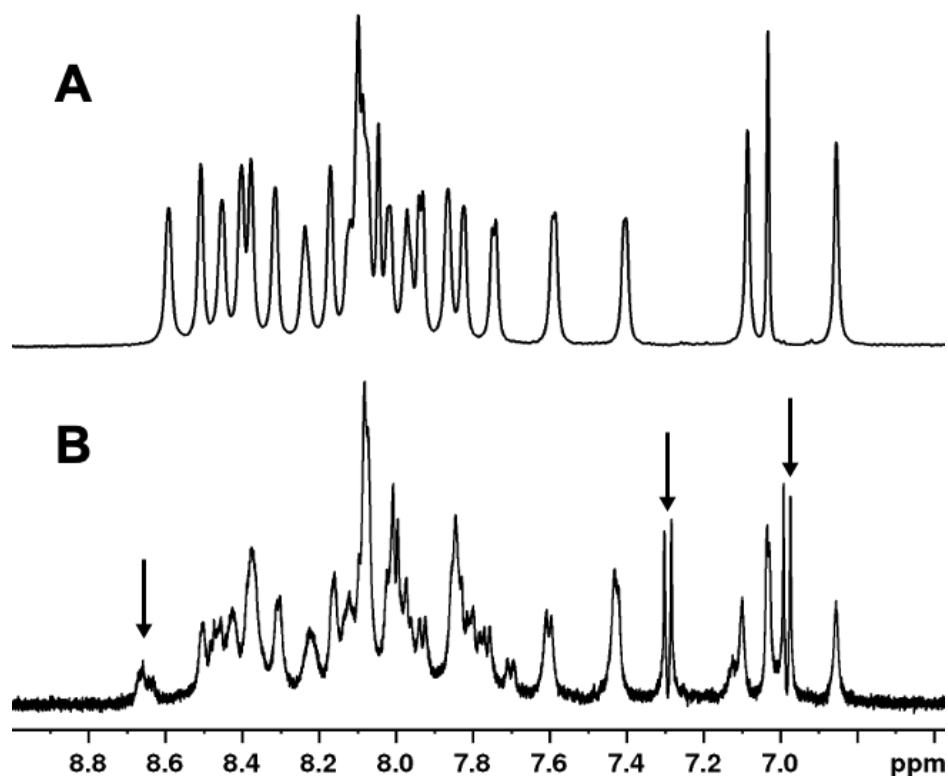


Figure 16: ¹H-NMR spectra of (A) Oce-LB1 recorded at 600 MHz spectrometer and (B) [LB1+163] impurity recorded at 350 MHz spectrometer. Both experiments were run in TFE-*d*₂:H₂O (60:40, v:v) containing 20 mM pH 7.0 phosphate buffer. The spectrum presented in (A) was obtained by Gomes et al., 2018³⁰.

In summary, all ocellatins were successfully purified despite the struggles with Oce-LB1 and -LB2. Ocellatin-F1 was purified by 31% yield whereas ocellatin-LB1 and -LB2 by 49% and 46% yield, respectively.

2.4.3. Purification of glycotriazole-peptides

Similar to ocellatins, the purification of the labeled glycotriazole-peptides was first carried out at Universidade Federal dos Vales do Jequitinhonha e Mucuri (UFVJM). Both [pOAcGlc-Trz-A¹]-HSP1-NH₂ and [pOAcGlc-Trz-A¹⁴]-PS-2 showed similar analytical profiles despite the lack of similarity between both sequences (**Figure 17**).

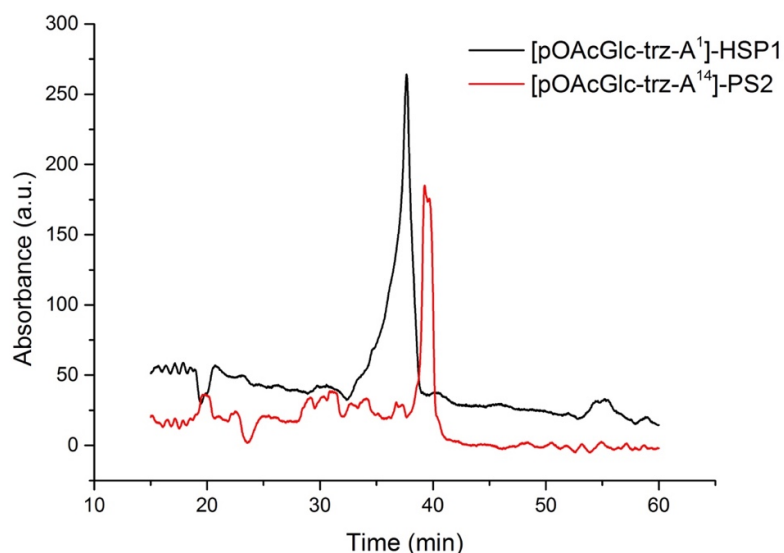


Figure 17: HPLC chromatograms obtained for [pOAcGlc-trz-A¹]-HSP1-NH₂ (black) and [pOAcGlc-trz-A¹⁴]-PS-2 (red) analytical profiles, with a Waters μ Bondapak TM C18 reverse stationary phase 10mm (7.8 x 3mm) semi-preparative column.

Since the analytical run of both glycotriazole-peptides crude samples presented large retention times, especially for PS-2 derivative ($t_R = 39.51$ min), a gradient of solvents was used to decrease run times. Thereafter, it was adjusted to a 35 min elution and retention times of 28.03 and 26.42 min were obtained for [pOAcGlc-Trz-A¹⁴]-PS-2 and [pOAcGlc-Trz-A¹]-HSP1-NH₂ respectively (**Figure 18**).

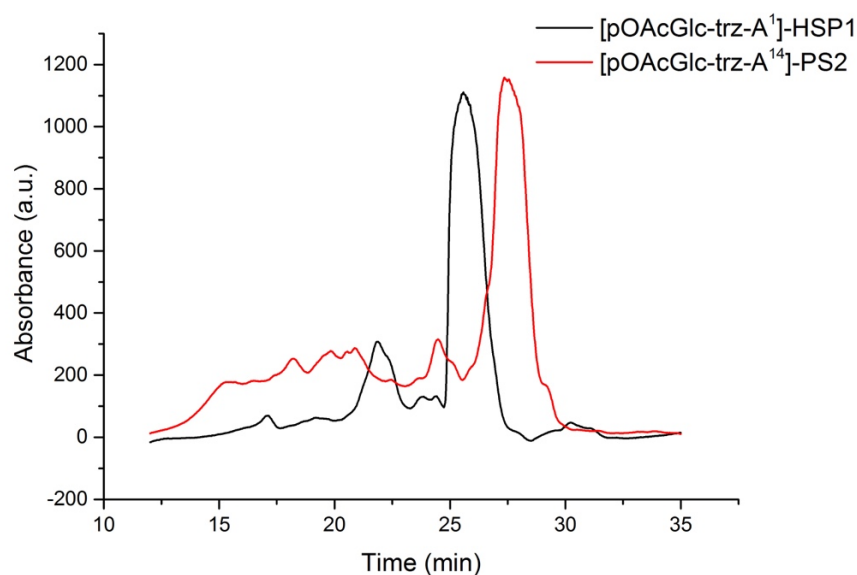


Figure 18: HPLC chromatograms obtained for [pOAcGlc-trz-A¹]-HSP1-NH₂ (black) and [pOAcGlc-trz-A¹⁴]-PS-2 (red) purifications, with a Waters μ Bondapak TM C18 reverse stationary phase 10mm (7,8 x 3mm) semi-preparative column.

After purification, each peptide was lyophilized, and their identity and purity were evaluated by MALDI-TOF mass spectrometry. Based on the obtained results, the purification of both GtP was unsuccessful, since apart from the labelled GtPs molecular peaks (m/z 1725.73 and 2487.25, which correspond to theoretical values of 1724.98 [pOAcGlc-trz-A¹]-HSP1-NH₂ and 2486.28 for [pOAcGlc-trz-A¹⁴]-PS-2, respectively), there were [MW – 43] for both glycotriazol peptides and both [MW – 86] and [MW + 163] peaks only for glycotriazole-PS-2 (**Figure 19**).

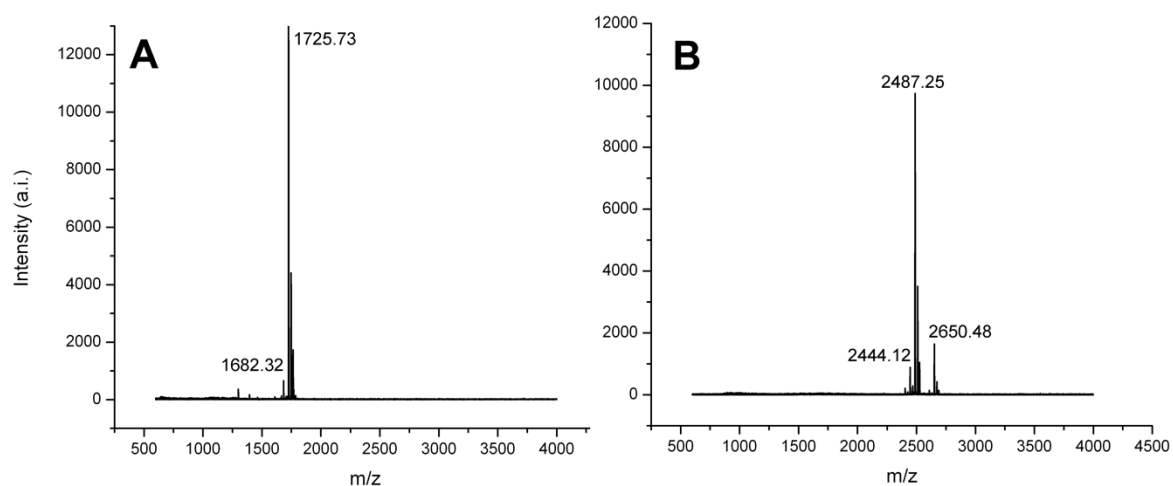


Figure 19: Mass spectra obtained by MALDI-TOF spectrometry for [pOAcGlc-trz-A1]-HSP1-NH₂ (A) and [pOAcGlc-trz-A14]-PS-2 (B) after HPLC purification.

As it was done for Ocellatin-LB1 and -LB2, both glycotriazol-HSP1-NH₂ and -PS-2 were purified at Université de Strasbourg. Purifications were carried out using a HPLC system with automatic collector and, likewise ocellatins -LB1 and -LB2, some of these impurities had retention times far close to those of the glycotriazole-peptides ($t_R = 18,57$ min for HSP1 and $t_R = 23,61$ min for PS-2). Finally, both glycotriazol-peptides were successfully purified, isolated and characterized by MALDI-TOF (single species at m/z 1726.337 for GtP-HSP1-NH₂ and m/z 2486.254 for GtP-PS2) (**Appendix 2 and 3**).

Overall, both glycotriazol-peptides were successfully purified despite the first undesired outcomes. Glycotriazol-HSP1-NH₂ was purified with a 55% yield whilst glycotriazol-PS-2 with a 53% yield.

2.5. Discussion

All purifications were achieved with reasonable yielding. However, the [MW + 163] impurity was found in four different peptide synthesis. Previous works⁵⁰ have reported several side reactions caused by steady carbocations released from the resin linker during the cleavage and global deprotection step. It has been reported that tryptophan tends to be alkylated by 2-(4-methylphenoxy) acetamide cation (**Figure 20**), released during the TFA acidolysis in Rink-amide MBHA peptidyl resins, unless it is sufficiently scavenged during the cleavage step.

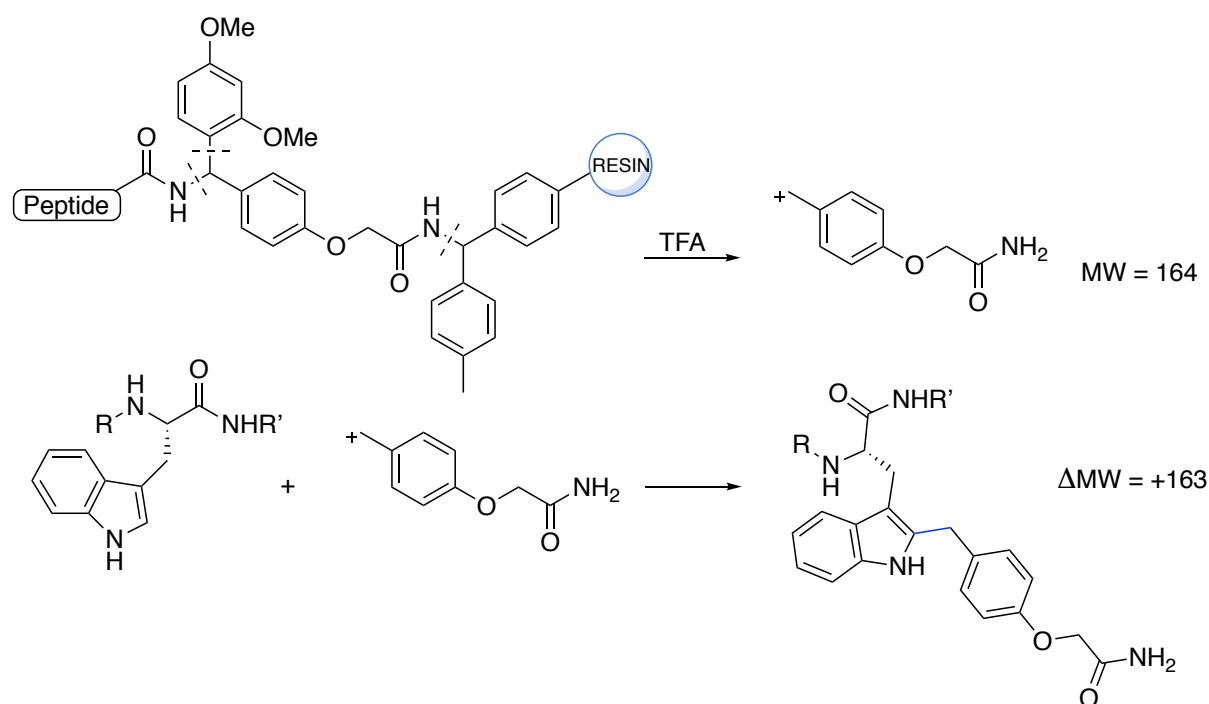


Figure 20: TFA acidolysis of Rink-amide MBHA resin and side-S_EAr (electrophilic aromatic substitution) of tryptophan indole ring.

None of the peptides studied in this work contain tryptophan residues nor the resin used was Rink MBHA. Nevertheless, Rink Amide also contains the 2-(4-methylphenoxy) acetamide moiety with a slight difference, as it is *N*-linked to a benzyl group instead of a diphenyl methyl. Therefore, although benzylic cation is less steady than diphenyl methyl one, *N*-benzyl bond might be broken by acidolysis since it is stabilized by resonance delocalization of the open valence shell. On the other hand, all peptides contain a plethora of nucleophilic sites, and for that reason, side reactions with 2-(4-methylphenoxy) acetamide cation may not rely only to indolyl alkylation case of tryptophan but to any nucleophilic attack followed by a proton elimination (**Figure 21**).

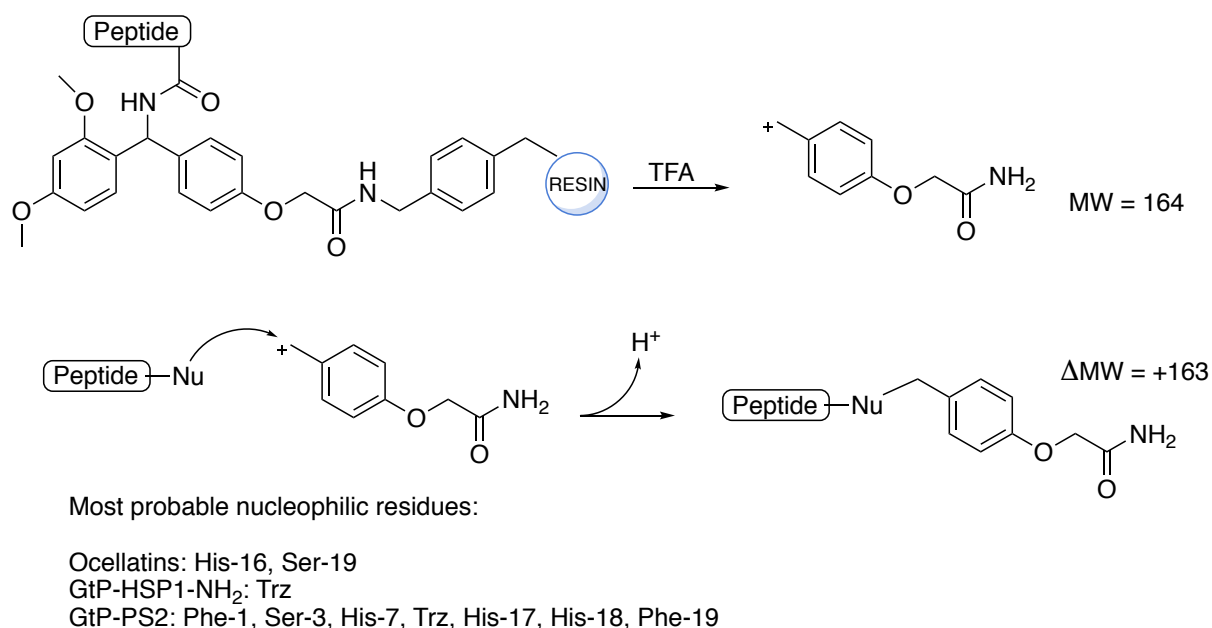


Figure 21: Proposal of TFA acidolysis of Rink-amide AM resin and side-reactions with any nucleophile site and 2-(4-methylphenoxy) acetamide cation.

In light of the arguments stated above, ¹H, NOESY and TOCSY spectra were recorded for [LB1 + 163] in order to find out whether the nature of [MW + 163] impurity stemmed from the alkylation of any nucleophilic site by 2-(4-methylphenoxy) acetamide cation. [LB1 + 163] sample was prepared in the same fashion as described in Gusmão's work³⁰. Hence, amide and both C₂ symmetry aromatic protons were identified and assigned by comparing both Oce-LB1 and [LB1 + 163] ¹H NMR spectra. Amide protons showed a swamped singlet at 7.12 ppm whilst aromatic protons showed two doublets at 6.98 and 7.28 ppm. However, neither benzylic nor alpha protons could be assigned as they appear overlapped with other signals. Thus, unless it cannot be assured that this impurity is caused by the release of by 2-(4-methylphenoxy) acetamide cation, the mass spectra and both aromatic and amide protons give some constrains that if the impurity is not caused by the 2-(4-methylphenoxy) acetamide cation, it must be a similar isomer of it.

Mass-to-charge ratio of +43 is characteristic of acetyl groups. Thus, both peaks [MW-43] and [MW-86] found in GtP-HSP1-NH₂ and GtP-PS-2 mass spectra suggest single and double deprotection of the per-*O*-acetylate-glucose moiety. Since the anomeric carbon is devoid of acetylated hydroxyl group, no position is apparently preferred for the ester hydrolysis, and consequently species related to [MW-43] and [MW-86] must be any isomer randomly deprotected. Notwithstanding, based on the nature of each hydroxyl group, C-6 is probably the

most reactive not only because it is the unique primary alcohol of the glucose moiety, but rather the least hindered (**Figure 22**).

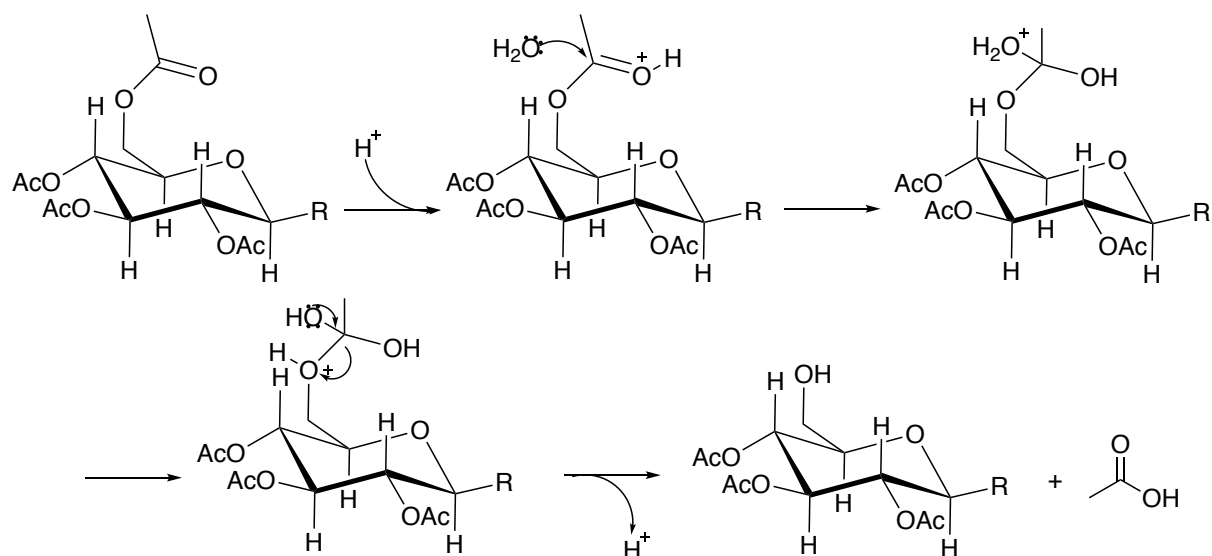


Figure 22: Proposal for the single deprotection [MW-43] at C-6 of the per-*O*-acetylate-glucose moiety.

In view of the drawbacks obtained during the cleavage step, some considerations must be taken into account in further studies in order to circumvent laborious purification protocols and to increase yields. Therefore, new synthetic routes need to be explored for the synthesis of glycotriazole-peptides in order to avoid undesirable deprotection of hydroxylic groups.

Nevertheless, following the purification, all peptides and glycotriazole-peptides were obtained with high purity, ensuring adequate quality for the solid-state NMR experiments and other biophysical assays.

Chapter 3: Membrane topology and interaction of peptides and glycotriazole peptides by static solid-state NMR spectroscopy

3.1. Introduction

The investigation of antimicrobial peptides by biophysical approaches, such as isothermal titration calorimetry (ITC), surface plasmon resonance spectroscopy (SPR) or Zeta Potential, has cast light in understanding the mechanisms of how antimicrobial peptides interact with membranes and selectively kill bacteria⁵¹. Notwithstanding, solid-state NMR spectroscopy has significantly grown in recent years as a valuable method for the investigation of membrane-associated proteins and peptides in their bilayer natural environment at atomic resolution. Important information as tilt and rotational pitch angles of helices are accessible using this technique, allowing one the determination of the peptide orientation with regard to the bilayer normal^{52,53}.

Unlike solution NMR spectroscopy, where fast molecular tumbling ensures averaging of the anisotropic nuclear interactions, in static solid samples the chemical shift, dipolar and quadrupolar interactions are all dependent on the molecular alignment relative to the magnetic field direction. Indeed, advantages can be taken from the orientation dependence of NMR interactions in the solid-state by reconstituting peptides and proteins into macroscopically oriented membranes. In this manner, by labeling isotopically in single sites with both ^{15}N ($I = \frac{1}{2}$) and ^2H ($I = 1$), the amide ^{15}N chemical shift and the deuterium quadrupolar splitting, among many other parameters, provide orientational constraints and thereby give important information on the alignment of peptides within the membrane.

3.1.1. Chemical shift anisotropy

The chemical shift stems from the induction of currents in the electron clouds of the molecule by the external magnetic field B_0 and the generation of induced magnetic fields (B_{induced}) because of these circulating molecular currents⁵⁴. Therefore, the nuclear spins sense the sum of

the applied external field and the induced field generated by the electrons, which leads to measurable shifts in the spin precession frequencies.

The induced field can be described by⁵⁴

$$B_{induced} = \sigma \cdot B_0 \quad [1]$$

Where σ represents the chemical shift interaction, which is mathematically described by a second-rank tensor⁵²:

$$\sigma = \begin{pmatrix} \sigma_{xx} & \sigma_{xy} & \sigma_{xz} \\ \sigma_{yx} & \sigma_{yy} & \sigma_{yz} \\ \sigma_{zx} & \sigma_{zy} & \sigma_{zz} \end{pmatrix} \quad [2]$$

However, for each nuclear site it exists three spatial directions of the external magnetic field B_0 whereby the induced field is parallel to the external field. These particular directions are inherently perpendicular to each other and hence set up the principal axes of the chemical shift tensor (σ)⁵⁴. The principal axes X , Y and Z generally correlate with the molecular structural components. Therefore, it is feasible to re-write [2] in the principal axes system (PAS), in which only diagonal elements persist:

$$\sigma_{PAS} = \begin{pmatrix} \sigma_{11} & 0 & 0 \\ 0 & \sigma_{22} & 0 \\ 0 & 0 & \sigma_{33} \end{pmatrix} \quad [3]$$

On the one hand, if all three principal values are equal, as it happens in solution NMR spectroscopy, the chemical shift tensor is said to be isotropic. On the other hand, if two or more principal values of the chemical shift tensor are different, then the chemical shift tensor is said to be anisotropic⁵⁴.

In order to gain insight into the alignment of peptides within membranes, the anisotropic σ_{PAS} tensor can be transformed into any other coordinate system by applying rotations in the three Euler angles (Φ , Θ , Ψ)⁵². The angle Φ consists of the first rotation about the z axis of the former frame, leading to an intermediate frame (x' , y' , z'). A second rotation (Θ) is carried out about y' , defining a third frame (x'' , y'' , z''). Finally, the transformation is completely achieved by

the rotation (Ψ) about z'' . The tensor in the new frame is hence expressed by using the rotation matrices R_{ij} .

$$\begin{pmatrix} \sigma_{XX} \\ \sigma_{YY} \\ \sigma_{ZZ} \end{pmatrix} = R \cdot \begin{pmatrix} \sigma_{11} & 0 & 0 \\ 0 & \sigma_{22} & 0 \\ 0 & 0 & \sigma_{33} \end{pmatrix} \cdot R^{-1} \quad [4]$$

$$R = R_{z''}(\Psi) \cdot R_{y'}(\Theta) \cdot R_z(\Phi) \quad [5]$$

$$R_z(\Phi) = \begin{pmatrix} \cos \Phi & \sin \Phi & 0 \\ -\sin \Phi & \cos \Phi & 0 \\ 0 & 0 & 1 \end{pmatrix} \quad [5a]$$

$$R_{y'}(\Theta) = \begin{pmatrix} \cos \Theta & 0 & -\sin \Theta \\ 0 & 1 & 0 \\ \sin \Theta & 0 & \cos \Theta \end{pmatrix} \quad [5b]$$

$$R_{z''}(\Psi) = \begin{pmatrix} \cos \Psi & \sin \Psi & 0 \\ -\sin \Psi & \cos \Psi & 0 \\ 0 & 0 & 1 \end{pmatrix} \quad [5c]$$

The zz component corresponds to the measured NMR chemical shift value⁵², which is related to the static magnetic field direction of the spectrometer. In this fashion, the measured amide ¹⁵N chemical shift can be expressed in terms of the Euler angles (Φ , Θ) and the principal elements of the chemical shift tensor σ_{11} , σ_{22} and σ_{33} :

$$\sigma_{zz} = \sigma_{11} \sin^2 \Theta \cos^2 \Phi + \sigma_{22} \sin^2 \Theta \sin^2 \Phi + \sigma_{33} \cos^2 \Theta \quad [6]$$

Should [6] be rewritten with Cartesian coordinates, the ¹⁵N chemical shift tensor can be graphically represented by an ellipsoid (**Figure 23**):

¹⁵ N chemical shift tensor [7a]		Ellipsoid [7b]
$\frac{\sigma_{11}}{R^2 \sigma_{zz}} X^2 + \frac{\sigma_{22}}{R^2 \sigma_{zz}} Y^2 + \frac{\sigma_{33}}{R^2 \sigma_{zz}} Z^2 = 1$		$\frac{X^2}{a^2} + \frac{Y^2}{b^2} + \frac{Z^2}{c^2} = 1$

Where $X = R\cos\Phi\sin\Theta$, $Y = R\sin\Phi\sin\Theta$, $Z = R\cos\Theta$ and relationships between both equations are $R^2 = 1/\sigma_{zz}$, $a^2 = 1/\sigma_{11}$, $b^2 = 1/\sigma_{22}$ and $c^2 = 1/\sigma_{33}$.

Thus, the three main axes of the ellipsoid are represented by $a = 1/\sqrt{\sigma_{11}}$, $b = 1/\sqrt{\sigma_{22}}$ and $c = 1/\sqrt{\sigma_{33}}$. In contrast, the intersection of the external magnetic field B_0 and the ellipsoid corresponds to $1/\sqrt{\sigma_{zz}}$, in which σ_{zz} is the chemical shift tensor that corresponds to a given orientation of the peptide⁵².

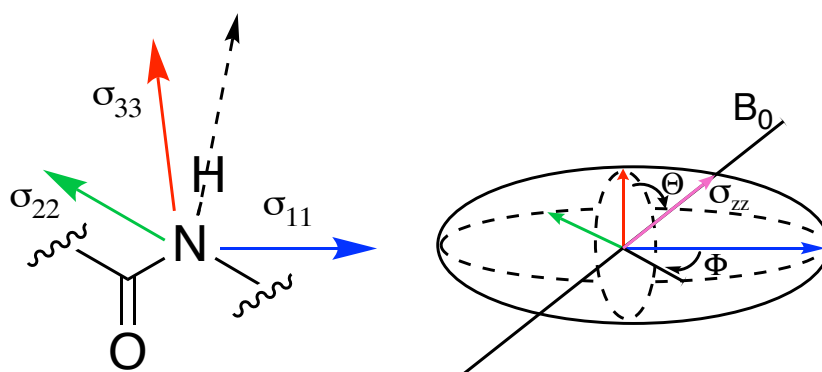


Figure 23: Ellipsoidal representation of the ^{15}N chemical shift tensor next to the molecular frame of the peptide bond. Both σ_{11} and σ_{33} are aligned within the plane of the paper whereas σ_{22} is oriented toward the viewer (adapted from Bechinger *et al.*, 2002)⁵².

Unlike σ_{33} component, which is characterized by a value of approximately 230 ppm, both σ_{11} and σ_{22} main tensor elements exhibit values in the 60 to 85 ppm range⁵⁵, respectively. However, despite this significant difference between σ_{33} and both σ_{11} and σ_{22} values, the σ_{33} component covers an angle of about 18° with the N-H vector in α -helical peptides and, as a consequence, both are oriented within a few degrees of the helix along the axis⁵².

Because of the similar magnitudes of σ_{22} and σ_{11} , which describes interactions perpendicular to σ_{33} axis, and the unique size of σ_{33} , σ_{zz} can be re-written as a prolate shaped tensor, it is to say a tensor with cylindrical symmetry:

$$\sigma_{zz} = (\sigma'_{\parallel} + \sigma'_{\perp})\cos^2\Theta + \sigma'_{\perp} \quad [8]$$

Where $\sigma'_{\parallel} = \sigma_{33}$ and $\sigma'_{\perp} = (\sigma_{11} + \sigma_{22})/2$ in this particular case. By this approach, Θ coincides within a few degrees with the tilt angle of the helix long axis with respect to the membrane normal. Moreover, this $\sigma'_{\parallel} - \sigma'_{\perp}$ coordinate system describes the ^{15}N amide tensor relative to

σ_{33} , which coincides with the helix axis and makes it a good approximation to determine peptides tilt angles.

By and large, under the assumption that rotational averaging predominantly occurs around an axis parallel to both magnetic field and bilayer normal, as well as ignoring the small difference between the alignment of σ_{33} and the helix long axis, the measured ^{15}N chemical shift is a direct indicator of the helix tilt angle. Therefore, ^{15}N resonance >200 ppm indicates transmembrane peptide orientations, whereas if ^{15}N resonates within the $\sigma_{11} - \sigma_{22}$ range (<100 ppm) indicates an alignment parallel to the membrane surface⁵² (**Figure 24**).

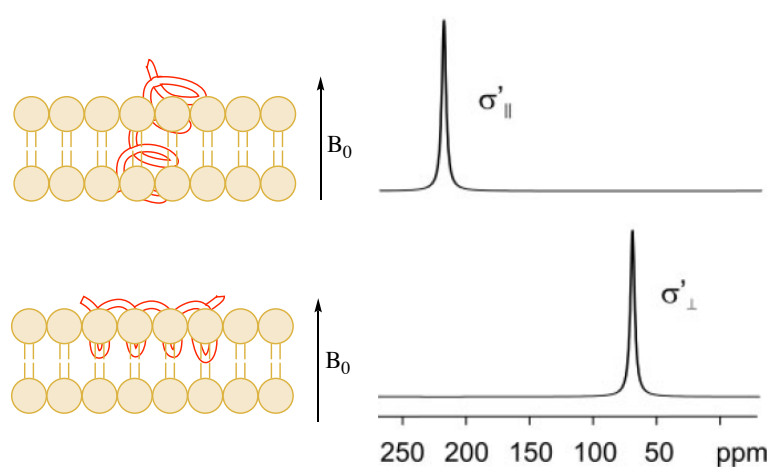


Figure 24: Representation of the proton-decoupled ^{15}N solid-state NMR spectrum and the orientation of helical peptides according to ^{15}N chemical shift (adapted from Bechinger *et al.*, 2002)⁵².

Chemical shift anisotropy also reveals interesting details about the phospholipid packing when antimicrobial peptides insert into the membrane interface. Thus, unlike the homogeneous lipid alignment of a perfectly oriented phospholipid bilayer results in a single ^{31}P resonance, about 30 ppm for POPC, additional peaks at lower chemical shifts positions sprung due to the distortion in the alignment of phospholipids induced by peptides⁵⁶.

3.1.2. Deuterium quadrupolar splitting

Deuterium charge distribution, so as any other nucleus whose $I > \frac{1}{2}$, can be described as a superposition of electric multipoles:

$$\mathbb{C}(r) = \mathbb{C}^{(0)}(r) + \mathbb{C}^{(1)}(r) + \mathbb{C}^{(2)}(r) + \dots + \mathbb{C}^{(n)}(r) \quad [9]$$

Where $\mathbb{C}^{(0)}(r)$ represents the magnitude of the total electric charge of the nucleus, $\mathbb{C}^{(1)}(r)$ the dipolar electric charge distribution, $\mathbb{C}^{(2)}(r)$ the quadrupolar electric charge distribution and so on⁵⁴.

In molecules, deuterium is engulfed by an electric cloud, which can be deemed as an electric potential field $V(r)$. Indeed, the center of the nucleus adopts a stable position at a minimum of the electric potential surface, which may lead to a deformation of the surface homogeneity in other sides of the nucleus affecting its rotational motion. Like the nuclear charge distribution, the electric potential field may be represented as a superposition of terms:

$$V(r) = V^{(0)}(r) + V^{(1)}(r) + V^{(2)}(r) + \dots + V^{(n)}(r) \quad [10]$$

Defining $V^{(0)}(r)$ as the electric potential at the center of the nucleus, $V^{(1)}(r)$ the potential gradient at the center of the nucleus, $V^{(2)}(r)$ the gradient of the gradient and so on.

The electric interaction energy of the nucleus and the field may be written as:

$$\begin{aligned} E_{elec} &= E_{elec}^{(0)} + E_{elec}^{(1)} + E_{elec}^{(2)} + \dots + E_{elec}^{(n)} \quad [11] \\ &= \int \mathbb{C}^{(0)} V^{(0)}(r) dr + \int \mathbb{C}^{(1)} V^{(1)}(r) dr + \int \mathbb{C}^{(2)} V^{(2)}(r) dr + \dots + \int \mathbb{C}^{(n)} V^{(n)}(r) dr \end{aligned}$$

The first term $E_{elec}^{(0)}$ represents the electrostatic forces between the nuclei and the electrons but it has no direct importance in NMR spectroscopy, nonetheless. Theoretically, $E_{elec}^{(1)}$ would represent the interaction of the nuclear electric dipole moment with the electric field. Notwithstanding, some studies have concluded that there is no electric dipole moments in nuclei and thereupon all electric terms, $E_{elec}^{(1)}, E_{elec}^{(3)}, E_{elec}^{(5)} \dots$, vanish. Furthermore, symmetry properties link the shape of the nucleus with its spin magnetic momentum as:

$$\mathbb{C}^{(n)}(r) = 0 \Leftrightarrow n > 2I \quad [12]$$

Therefore, ^1H ($I = 1/2$) is spherically symmetrical and there are no electric energy terms that depend on the orientation or internal structure of the nucleus. On the other hand, ^2H ($I = 1$), and

any other nucleus whose $I > \frac{1}{2}$, the electric charge distribution is asymmetrical and depends on its orientation (θ)⁵⁴.

Since the electric quadrupolar moment is rather small, it may be treated as a small perturbation of the magnetic energy⁵⁷ and, thanks to this approximation, Schrödinger's equation can be solved for a full spin Hamiltonian, which contains both magnetic and electric terms. The energy levels for any nucleus whose $I = 1$ is explicitly:

$$\left. \begin{aligned} E_{+1} &= -\mu_N B_0 + \frac{1}{4} eQV \\ E_0 &= -\frac{1}{2} eQV \\ E_{-1} &= \mu_N B_0 + \frac{1}{4} eQV \end{aligned} \right\} \quad [13]$$

Where Q is the nuclear electric quadrupole moment, e the fundamental charge and V the electric field gradient tensor. The allowed transitions given by the selection rule $\Delta m = \pm 1$ lead to the resonance energies:

$$h\nu_+ = E_{-1} - E_0 = \mu_N B_0 + \frac{3}{4} eQV \quad [14a]$$

$$h\nu_- = E_0 - E_{+1} = \mu_N B_0 - \frac{3}{4} eQV \quad [14b]$$

Hence, the frequency spacing of the two lines observed in the ²H NMR spectra are called the quadrupole splitting:

$$\Delta\nu_Q = \nu_+ - \nu_- = \frac{3}{2} \frac{eQ}{h} V \quad [15]$$

The electric field gradient tensor V is similar to the CSA one, as far as properties are considered. However, due to electromagnetic theory constrains V must be traceless^{54,57}, it is to say $V_{xx} + V_{yy} + V_{zz} = 0$. Thus, the principal values of the electric field gradient tensor are:

$$V_{PAS} = \begin{pmatrix} -\frac{1}{2} eq(1 - \eta_Q) & 0 & 0 \\ 0 & -\frac{1}{2} eq(1 + \eta_Q) & 0 \\ 0 & 0 & eq \end{pmatrix} \quad [16]$$

Where η_Q represents the biaxiality $(V_{xx} - V_{yy})/V_{zz}$, and it consequently leads to that fact that the z direction is the largest field gradient whereas y direction the smallest one ($V_{zz} > V_{xx} > V_{yy}$).

Should the spectral changes be associated with the rotation of a single axis from the deuterium nucleus principal axes system, a better physical meaning for equation [15] is obtained. Hence, the simplest situation is an uniaxial alignment of the magnetic field B_0 parallel to V_{zz} , which is the direction of the largest electric field gradient⁵⁷.

As previously done for ^{15}N chemical shift, the anisotropic V_{PAS} tensor can be transformed into the laboratory frame system by applying rotations in two Euler angles [5a, 5b]. Henceforth, the angle Φ consists of the first rotation about the z axis of the field gradient tensor and a second rotation (θ) about y' , defining that V_{zz} is parallel to B_0 . Therefore, the quadrupolar splitting at any molecular orientation is described as⁵⁷:

$$\Delta\nu_Q = \frac{3}{2} \frac{e^2 q Q}{h} \frac{(3\cos^2\theta - 1)}{2} \quad [17]$$

Where θ is the angle between the principal Z -axis of the electric field gradient tensor and the static magnetic field (**Figure 25**).

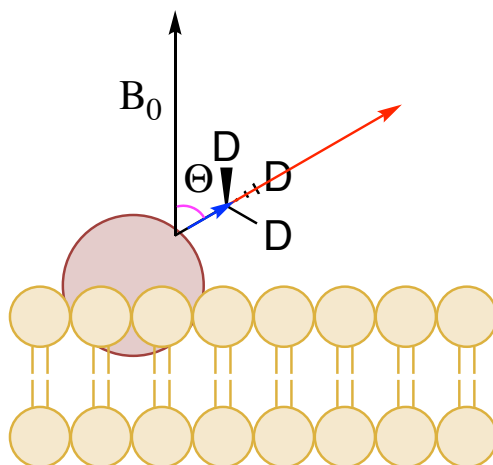


Figure 25: Schematic representation of θ , the angle between the static magnetic field B_0 and the principal Z -axis of the electric field gradient tensor.

This orientational dependency between the deuterium quadrupolar splitting and the spectrometer magnetic field can be used to obtain topological restraints high complementary to those derived from ^{15}N chemical shift. [$^2\text{H}_3$]-Alanine residues have interesting advantages⁵⁸. At

room temperature, the alanine methyl group exhibits fast rotational motions around the C_{α} - C_{β} bond. As a result, the three methyl deuterons are equivalent and exhibit overlapping resonances. The resulting ^2H tensor is axially symmetric with respect to the C_{α} - C_{β} bond vector and the measured quadrupolar splitting is directly related to Θ . Thus, ^2H quadrupolar splitting can be used to describe the orientation of the C_{α} - C_{β} bond relative to the magnetic field direction.

3.2. Objectives

1. Perform ^1H -decoupled ^{31}P solid-state NMR experiments of mechanically oriented phospholipid bilayers to determine their alignment and perturbation degree.
2. Perform ^1H -decoupled ^{15}N and ^2H solid-state NMR experiments of peptides (Oce-F1, Oce-LB1 and Oce-LB2) and glycotriazole-peptides ($[p\text{-Glc-trz-A}^1\text{]-HSP1-NH}_2$ and $[p\text{-Glc-trz-A}^{14}\text{]-PS-2}$) accommodated in mechanically oriented phospholipid bilayers.
3. Determine the membrane topologies of peptides (Oce-F1, Oce-LB1 and Oce-LB2) and glycotriazole-peptides ($[p\text{-Glc-trz-A}^1\text{]-HSP1-NH}_2$ and $[p\text{-Glc-trz-A}^{14}\text{]-PS-2}$) through comparison between the experimental and simulated NMR data.

3.3. Methods

3.3.1. Solid-state NMR spectroscopy

POPC, 50 mg, and the respective amount of labelled ocellatins were codissolved in a mixture of chloroform:methanol (3:1, v:v) (Sigma-Aldrich) at a peptide/lipid ratio 1/99 mol/mol. The same procedure was used to prepare the glycotriazole-samples, although different membrane compositions were used: POPC:POPG:Ergosterol (3:1:1 molar ratio) for $[p\text{OAcGlc-Trz-A}^1\text{]-HSP1}^{33}$ and POPC:POPS (3:1 molar ratio) for $[p\text{OAcGlc-Trz-A}^{14}\text{]-PS-2}^{53}$. The resulting mixture was concentrated by reducing the solvent volume under a nitrogen stream leading to a gel, which was spread onto 22 ultrathin coverglasses (8 x 12 mm², Marienfeld, Lauda-Königshofen, Germany). The samples were first dried in air and straightaway in high vacuum overnight. Thereafter, the membranes were equilibrated at 93% relative humidity with deuterium depleted water for two days, then the coverglasses were stacked up on the top of each other and the resulting pile was sealed with Teflon tape and plastic wrappings⁵¹. The

oriented samples were inserted into e-free NMR flat-coil probes (Bruker, Biospin, Rheinstetten, Germany) with the membrane normal parallel to the magnetic field direction. All experiments were recorded at room temperature.

Proton-decoupled ^{31}P solid-state NMR spectra of the oriented phospholipid bilayers encompassing the peptides were recorded at 121.570 MHz on a Bruker Avance wide-bore 300 MHz NMR spectrometer. A Hahn-echo⁵⁹ pulse sequence with 8 μs 90° pulse width, a spectral width of 100 kHz, an echo delay of 50 μs , a recycle delay of 3 s and an acquisition time of 10.2 ms were used. Spectra were referenced externally to 85% H_3PO_4 at 0 ppm.

Proton-decoupled ^{15}N cross-polarization (CP) spectra were acquired at 76.02 MHz on a Bruker Avance wide-bore 750 MHz solid-state NMR spectrometer using a cross-polarization pulse sequence⁶⁰. The CP contact time was 700 μs , the recycle delay 2 s, the 90° pulse length 8 μs , acquisition time 4 ms and the spectral width 50 kHz. The spectra were calibrated relative to external $^{15}\text{NH}_4\text{Cl}$ at 41.5 ppm.

^2H spectra of the $^2\text{H}_3$ -alanine-labeled peptides reconstituted into phospholipid bilayers were recorded at 76.76 MHz on a Bruker Avance wide-bore 500 MHz using a quadrupolar echo pulse sequence^{51,61}. The following parameters used were: 1000 kHz spectral width, 5 ms acquisition time, 5.6 μs 90° pulse width, 1s recycle delay and 40 μs echo delay. The spectra were referenced relative to $^2\text{H}_2\text{O}$ (0 ppm). Nonetheless, due to the harsh ringing artifacts obtained for both (3,3,3- $^2\text{H}_3$ -Ala-10, ^{15}N -Leu-17)-Oce-LB2 and [pOAcGlc-Trz-A¹⁴]-PS-2 spectra, EASY tool⁶² was used to remove them. Thus, all experimental parameters were the same as mentioned before except for the acquisition time, which was 2 ms.

These experiments were performed at the solid-state NMR laboratory of the University of Strasbourg (France), under the supervision of Professor Burkhard Bechinger.

3.3.2. Simulations of the membrane topology

The solution NMR structures of Oce-LB1, -LB2 and -F1³⁰, [pOAcGlc-Trz-A¹]-HSP1-NH₂⁶³ [pOAcGlc-Trz-A¹⁴]-PS-2⁴⁰ were used in the simulation of ^{15}N chemical shift (σ_{zz}) and deuterium quadrupolar splitting ($\Delta\nu_Q$), to determine the orientation of each peptide in the lipid bilayers. Each molecular geometry was first aligned^{38,64} by means of ^{15}N set as the origin

(0,0,0). Thereafter, z axis was defined laying parallel to the helix main axis by choosing a second backbone N atom (**Table 3**). Finally, the internal coordinate system was defined by setting the carbonyl carbon of the peptide bond involving the ^{15}N -labeled site at the xz -plane leading to the y axis orthogonal to the plane of the ^{15}N -labeled peptide bond.

Table 3: Atoms used to align both peptides and glycotriazole-peptides

Peptide	Oce-LB1	Oce-LB2	Oce-F1	GtP-HSP1-NH ₂	GtP-PS-2
Number of atoms	325	325	325	252	331
Origin (0,0,0)	^{15}N -Leu-17	^{15}N -Leu-17	^{15}N -Leu-17	^{15}N -Ala-10	^{15}N -Leu-15
z-axis (0, 0, z)	N-Ala-10	N-Ala-10	N-Ala-10	C-Asp-3	N-Ile-4
xz-plane (x, 0, z)	C-His-16	C-His-16	C-His-16	C-Ile-9	C-Ala*-14

On the one hand, the observed ^{15}N chemical shift is given by equation [6], being σ_{11} , σ_{22} and σ_{33} the chemical shift main tensor elements⁵⁵ whereas both Φ and Θ are the Euler angles representing rotations around z and y' axes, respectively⁵². On the other hand, the quadrupolar splitting $\Delta\nu_Q$ is calculated by using equation [17], where, e^2qQ/h is the quadrupolar coupling constant^{56,57}.

Having all these theoretical considerations in mind, as well as the defined coordinate system, the peptide structures are successively rotated (180 x 180 steps) around the helix main axis (z -axis) and y -axis. The values of σ_{zz} and $\Delta\nu_Q$ are evaluated for each alignment as a function of the tilt (τ) and rotational pitch (ρ) angles. The ^{15}N chemical shift is calculated from [6] by two angular correcting terms obtained from structural data, which are related to rotations around the y and x axes in order to properly align the local coordinate system with the main axes system, as σ_{33} tensor draws an angle of $\sim 18^\circ$ with the N-H bond vector^{53,55}. The C_α and C_β coordinates of the ^2H -labeled sites were used to evaluate $\cos^2\Theta$ and hereafter the values of $\Delta\nu_Q$. Both geometry alignments and simulations of σ_{zz} and $\Delta\nu_Q$ were performed using a FORTRAN program previously developed by our research group⁶⁵.

3.4. Results

3.4.1. Ocellatins

Ocellatins labeled with stable ^{15}N and ^2H isotopes at selected positions (^{15}N -Leu-17 and 3,3,3- $^2\text{H}_3$ -Ala-10) were yielded by solid-phase peptide synthesis and reconstituted into mechanically oriented POPC bilayers. Thereafter, the samples were inserted into the NMR spectrometer with the membrane normal parallel to the magnetic field direction. The proton-decoupled ^{15}N NMR spectra of all ocellatins (**Figure 26**) exhibit chemical shifts smaller than 100 ppm, indicating that all helices present an alignment approximately parallel to the bilayer surface⁵². Oce-LB1, -LB2 and -F1 exhibit resonances at 69 ppm (A), 76 ppm (B) and 64 ppm (C), respectively. Narrow line shapes observed in the spectra of Oce-LB1 and -F1 indicate that the peptides' labeled sites are homogeneously aligned⁶⁶ parallel to the bilayer surface. Oce-LB2 spectrum, on the other hand, exhibits a broader line shape in comparison to the spectra of the other peptides, which suggests an alignment somehow more inhomogeneous.

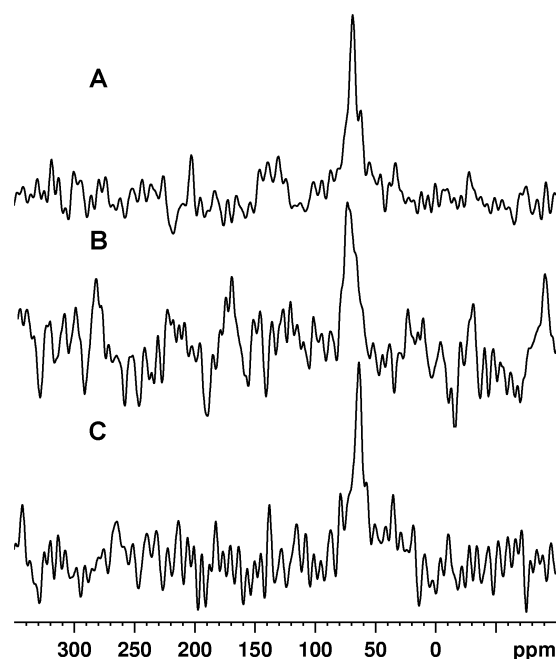


Figure 26: Proton-decoupled ^{15}N NMR spectra of Ocellatins at 1.0 mol % reconstituted into mechanically oriented POPC lipid bilayers. (A) (3,3,3- $^2\text{H}_3$ -Ala-10, ^{15}N -Leu-17)-Oce-LB1, (B) (3,3,3- $^2\text{H}_3$ -Ala-10, ^{15}N -Leu-17)-Oce-LB2 and (C) (3,3,3- $^2\text{H}_3$ -Ala-10, ^{15}N -Leu-17)-Oce-F1. All spectra were recorded for alignments with the membrane normal parallel to the magnetic field of the spectrometer.

The ^2H NMR spectra of the ocellatins reconstituted into oriented POPC lipid bilayers (**Figure 27**) present three peaks. The central one is related to the residual HDO form of deuterium depleted water whereas the other two correspond to pair of resonances from the labeled peptide

sites. These two latter define quadrupolar splittings of 17.8 kHz (A), 18.6 kHz (B) and 12.0 kHz (C) for samples encompassing selectively labelled Oce-LB1, -LB2 and -F1. Again, broader line shapes are observed in the spectrum Oce-LB2, reinforcing the idea of greater topological heterogeneity

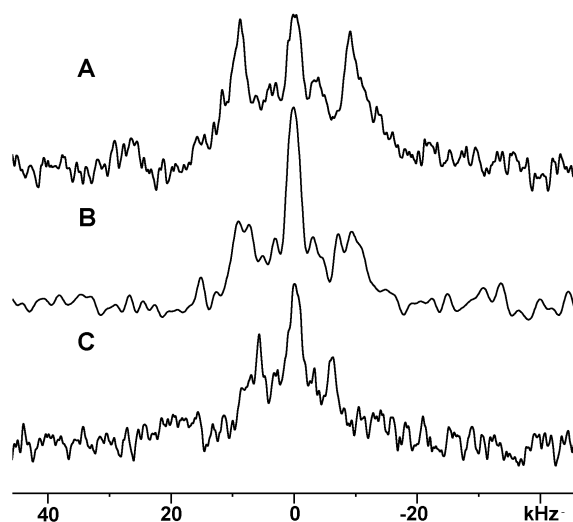


Figure 27: ^2H NMR spectra of Ocellatins at 1.0 mol % reconstituted into mechanically oriented POPC lipid bilayers. (A) $(3,3,3\text{-}^2\text{H}_3\text{-Ala-10, } ^{15}\text{N-Leu-17})\text{-Oce-LB1}$, (B) $(3,3,3\text{-}^2\text{H}_3\text{-Ala-10, } ^{15}\text{N-Leu-17})\text{-Oce-LB2}$ and (C) $(3,3,3\text{-}^2\text{H}_3\text{-Ala-10, } ^{15}\text{N-Leu-17})\text{-Oce-F1}$. All spectra were recorded for alignments with the membrane normal parallel to the magnetic field of the spectrometer. All central peaks are from the residual HDO form of deuterium depleted water (≤ 1 ppm).

All ^{31}P NMR spectra (**Figure 28**) present an intense peak near 30 ppm, which is characteristic of liquid crystalline POPC bilayers with the lipid long axes aligned parallel to B_0 ^{56,64}. This intense peak indicates a good degree of membrane alignment despite the presence of the peptides, whereas the smaller ^{31}P resonance intensities observed at -15 ppm are related to phosphorus headgroups lying perpendicular to the external magnetic field. The similar peak intensities in all spectra suggest membrane disturbances were not caused during sample preparation, but rather by the peptides themselves⁵⁶.

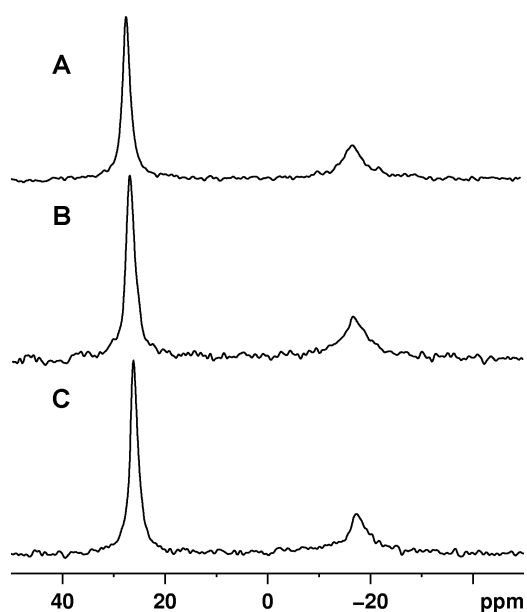


Figure 28: Proton-decoupled ^{31}P NMR spectra of mechanically oriented POPC lipid bilayers containing (A) (3,3,3- $^2\text{H}_3$ -Ala-10, ^{15}N -Leu-17)-Oce-LB1, (B) (3,3,3- $^2\text{H}_3$ -Ala-10, ^{15}N -Leu-17)-Oce-LB2 and (C) (3,3,3- $^2\text{H}_3$ -Ala-10, ^{15}N -Leu-17)-Oce-F1 at 1.0 mole %. Samples were prepared by spreading 50 mg of lipids on 22 glass plates. All spectra were recorded for alignments with the membrane normal parallel to the magnetic field of the spectrometer.

Although it is not possible to determine precisely the peptide orientation from the ^{15}N chemical shift or the ^2H quadrupolar splitting alone, the two parameters furnish highly complementary topological restraints that can be used to obtain an accurate definition of the peptide orientation in the bilayer ^{56,65}. As presented in **Figure 29 (A-C)**, the traces in black represent orientations in which the simulated ^{15}N chemical shift agrees with the experimental data within ± 2 ppm, whereas the red lines trace the angular pairs where the ^2H quadrupolar splitting agrees with experimental values within ± 1 kHz. In the three cases, only four topologies agree with both measurements simultaneously (intersections in blue) and these are shown beneath each contour plot in **Figure 29 (D-F)**, where the hydrophilic sidechains are presented in green and the hydrophobic in blue. Energetic considerations are used to solve ambiguities of which alignment represents the most suitable topology for each peptide ^{65,67}.

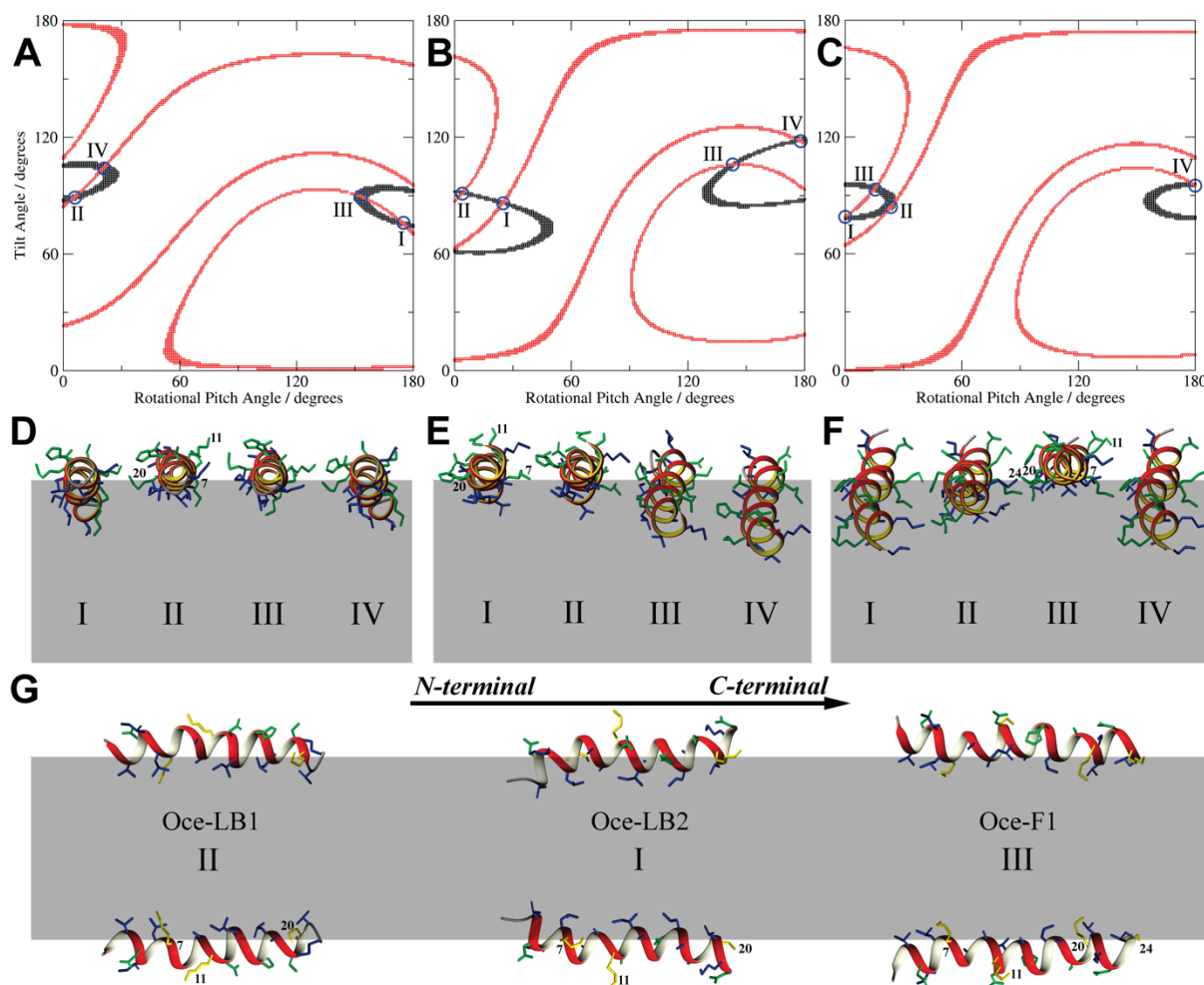


Figure 29: Alignments of (A) Oce-LB1, (B) Oce-LB2 (B) and (C) Oce-F1 (C) in lipid bilayers shown as functions of the tilt and rotational pitch angles. Black points represent orientations that are in agreement within the respective ^{15}N chemical shift whereas red points represent alignments that agree within the respective deuterium quadrupolar splitting. The intersection points shown as blue circles indicate orientations that simultaneously agree with both experimental parameters. Underneath each contour plot the respective peptide three-dimensional structure (PDB 5UA6, 5UA7 and 5U9Y³⁰) is used to the topologies related to the intersection points for (D) Oce-LB1, (E) Oce-LB2 and (F) Oce-F1 (the N-termini shown in the back). Rotated views of the most thermodynamically favored alignment of each peptide is shown in panel (G). Hydrophilic residues are shown in green, whereas hydrophobic residues in blue. In panel (G) the lysine residues (-7, -11, -20 and -24) are highlighted in yellow. The gray areas represent approximately the hydrophobic thickness of a bilayer.

For Oce-LB1, topologies I ($175^\circ/76^\circ$) and IV ($21^\circ/104^\circ$) (**Figure 29A and D**) present significant deviations of planarity (14°) which would cause the insertion of hydrophilic amino acids within the hydrophobic part of the bilayer. Conversely, topologies II ($6^\circ/89^\circ$) and III ($153^\circ/89^\circ$) represent both planar alignments, although important differences arise from rotations around the helix main axis (pitch angle). Whereas III leads to the complete insertion of the charged Lys-7 into the hydrophobic core ($\rho = 153^\circ$), topology II represents the adequate partition of hydrophilic and hydrophobic residues within the membrane interface ($\rho = 6^\circ$). Although the Lys-7 lies in the bilayer interface, the representation shown in **Figure 29E** indicates the insertion of its sidechain into the membrane, which would represent a significant energetic cost.

However, the lysine sidechains are flexible and have been suggested to snorkel at the membrane interface⁶⁸⁻⁷¹. Thus, it is expected that that hydrophobic CH₂ segments and the charged amino group at the end of the sidechain would redistribute in such a manner to position the positive ⁺NH₃ at the membrane hydrophilic surface^{68,72}. Actually, apart from a single correlation involving the δ hydrogens of Lys-7, no other medium range inter-residue NOE involving the respective γ , δ , or ϵ hydrogens was observed in the respective NOESY spectrum, which indicates a considerable degree of freedom for these lysine side chains³⁰.

Similarly, for Oce-LB2 the in-plane topology I (25°/86°) presents a clear partition between hydrophilic and hydrophobic faces within the membrane interface (**Fig.30 B and E**), which is clearly delimited by Lys-7 and Lys-20. Topology II (4°/91°) represents a quite similar alignment, although it forces the insertion of Lys-20 into the bilayer, which represents an energy cost. In contrast, the other topologies (III 143°/106° and IV 178°/118°) represent unsuitable alignments, since the helix tilt angle pulls several hydrophilic residues into the hydrophobic core of the membrane. Likewise, topologies I (0°/79°), II (23°/84°) and IV (180°/95°) are also incongruous for Oce-F1 (**Figure 29C and F**), whereas III (15°/93°) reflects an ideal amphipathic partition for this in-plane orientation. Finally, the lateral perspectives of the thermodynamically most favored topology of each peptide are presented in **Figure 29G**, where the sidechains of the lysine residues are presented in yellow.

Below are summarized the experimental NMR parameters and topological data obtained for the thermodynamically most favorable topologies of ocellatin peptides (**Table 4**)

Table 4: Summary of the solid-state NMR parameters and membrane topologies for Oce-LB1, Oce-LB2 and Oce-F1

Peptide	σ_{zz} (ppm)	$\Delta\nu_Q$ (kHz)	Orientation (ρ/τ)
Oce-LB1	69	17.8	6°/89°
Oce-LB2	76	18.6	25°/86°
Oce-F1	64	12.0	15°/93°

3.4.2. Glycotriazole-peptides

Glycotriazole-peptides labeled with stable ^{15}N and ^2H isotopes at selected positions (^{15}N -Leu-15 and $3,3,3\text{-}^2\text{H}_3$ -Ala-8 for [pOAcGlc-Trz-A 14]-PS-2, and $3,3,3\text{-}^2\text{H}_3$ -Ala-8, ^{15}N -Ala-10 for [pOAcGlc-Trz-A 1]-HSP1-NH $_2$) were obtained by solid-phase peptide synthesis and copper(I)-catalyzed Huisgen 1,3-dipolar cycloaddition.

Due to previous investigations with the respective original peptides or GtPs reported in the literature, different membrane compositions were chosen^{33,39,53}. Thus, [pOAcGlc-Trz-A 14]-PS-2 was reconstituted into mechanically oriented POPC:POPS (3:1 mol:mol) bilayers, whereas [pOAcGlc-Trz-A 1]-HSP1-NH $_2$ was accommodated into POPC:POPG:Ergosterol (3:1:1 mol:mol:mol) bilayers. Thereafter, the samples were inserted into the NMR spectrometer with the membrane normal parallel to the magnetic field direction. The proton-decoupled ^{15}N NMR spectra of the two glycotriazole-peptides (**Figure 30**) exhibit chemical shifts smaller than 100 ppm, indicating that the helices present alignments approximately parallel to the bilayer surface⁵². On the one hand, ^{15}N -Leu-[pOAcGlc-Trz-A 14]-PS-2 resonates at 75 ppm (**Figure 30A**) within a narrow window of resonances, indicating a homogeneous alignment parallel to the bilayer surface. On the other hand, [pOAcGlc-Trz-A 1]-HSP1-NH $_2$ exhibits ^{15}N -resonance at 82 ppm (**Figure 30B**) and a broader line shape, suggesting a rather more inhomogeneous alignment.

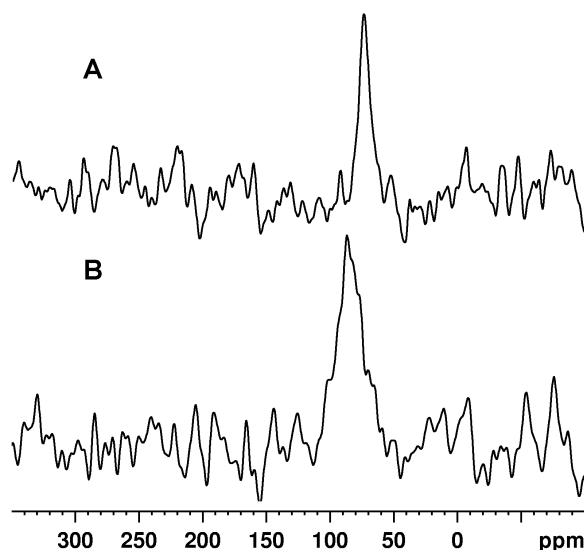


Figure 30: Proton-decoupled ^{15}N NMR spectra of glycotriazole-peptides at 1.0 mol % reconstituted into mechanically oriented phospholipid bilayers. (A) ($3,3,3\text{-}^2\text{H}_3$ -Ala-8, ^{15}N -Leu-15)-[pOAcGlc-Trz-A 14]-PS-2 in POPC:POPS (3:1 molar ratio), (B) ($3,3,3\text{-}^2\text{H}_3$ -Ala-8, ^{15}N -Leu-10)-[pOAcGlc-Trz-A 1]-HSP1-NH $_2$ in POPC:POPG:Ergosterol (3:1:1 molar ratio). All spectra were recorded for alignments with the membrane normal parallel to the magnetic field of the spectrometer.

The ^2H NMR spectra of [pOAcGlc-Trz-A 14]-PS-2 reconstituted in POPC:POPS (3:1 mol:mol) bilayers revealed a quadrupolar splitting of 44.5 kHz (**Figure 31A**). On the other hand, the frequency spacing between the two allowed transitions was 23.0 kHz for [pOAcGlc-Trz-A 1]-HSP1-NH $_2$ in POPC:POPG:Ergosterol (3:1:1 mol:mol:mol) membranes (**Figure 31B**).

^{31}P NMR experiments reveal lipids long axis orientation in bilayers. Hence, the spectrum for [pOAcGlc-Trz-A 14]-PS-2 sample which present two well-defined peaks from POPC (near 30 ppm) and POPS (near 40 ppm) demonstrates a highly homogeneous alignment for both phospholipids in liquid-crystal state with the lipid main axis parallel to B_0 (**Figure 32A**). Conversely, both POPC and POPG phospholipids appear isochronally⁵⁶ under the peak of 30 ppm in [pOAcGlc-Trz-A 1]-HSP1-NH $_2$ sample, which indicate alignments parallel to B_0 . The peak of lower intensity near -15 ppm stems from the phosphorous headgroups lying perpendicular to the external magnetic field (**Figure 32B**) and also suggests a greater heterogeneity of the phospholipid headgroups in comparison to the bilayers encompassing the glycotriazole PS-2 derivative.

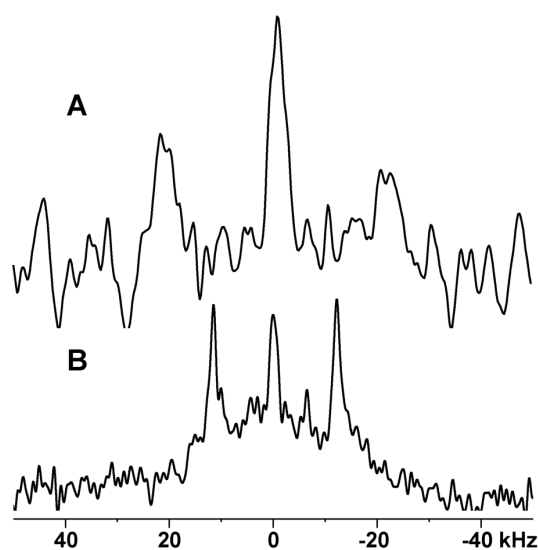


Figure 31: ^2H NMR spectra of glycotriazole-peptides at 1.0 mol % reconstituted into mechanically oriented phospholipid bilayers. (A) (3,3,3- $^2\text{H}_3$ -Ala-8, ^{15}N -Leu-15)-[pOAcGlc-Trz-A 14]-PS-2 in POPC:POPS (3:1 molar ratio), (B) (3,3,3- $^2\text{H}_3$ -Ala-8, ^{15}N -Leu-10)-[pOAcGlc-Trz-A 1]-HSP1-NH $_2$ in POPC:POPG:Ergosterol (3:1:1 molar ratio). All spectra were recorded for alignments with the membrane normal parallel to the magnetic field of the spectrometer. All central peaks are from the residual HDO form of deuterium depleted water (≤ 1 ppm).

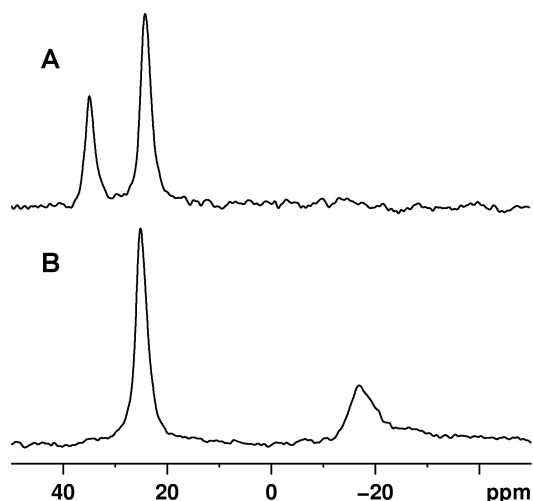


Figure 32: Proton-decoupled ^{31}P NMR spectrum of mechanically oriented (A) POPC:POPS (3:1 molar ratio) phospholipid bilayers containing (3,3,3- $^2\text{H}_3$ -Ala-8, ^{15}N -Leu-15)-[pOAcGlc-Trz-A 14]-PS-2 (B) POPC:POPG:Ergosterol (3:1:1 molar ratio) phospholipid bilayers containing (3,3,3- $^2\text{H}_3$ -Ala-8, ^{15}N -Leu-10)-[pOAcGlc-Trz-A 1]-HSP1-NH $_2$ F1 at 1.0 mole %. Samples were prepared by spreading 50 mg of lipids on 22 glass plates. All spectra were recorded for alignments with the membrane normal parallel to the magnetic field of the spectrometer.

As mentioned before, the combination of ^{15}N chemical shift and ^2H quadrupolar splitting furnishes enough topological restraints to depict peptides orientation when accommodated in phospholipid bilayers. In accordance with the same color pattern previously used for ocellatins topological contour maps, in **Figure 33A and 34A** the traces in black represent orientations in which the simulated ^{15}N chemical shift agrees with the experimental data within ± 2 ppm, the red lines trace the angular pairs where the ^2H quadrupolar splitting agrees with experimental values within ± 1 kHz and the blue circles represent the topologies which agree with both measurements simultaneously. These topologies are also represented in **Figure 33B and 34B** where the hydrophobic sidechains are presented in green, the hydrophobic in blue and the glycotriazole residue in red. Finally, the lateral perspectives of the most thermodynamically favored topology of each glycotriazole-peptide are presented in **Figure 33C and 34C**.

The three-dimensional NMR structure used for the topological simulations of PS-2 glycotriazole derivative was obtained by Wust and co-workers⁴⁰. Interestingly, only two topologies agree simultaneously with the ss-NMR experimental data obtained for [pOAcGlc-Trz-A 14]-PS-2 (**Figure 33A**). Among these, topology I ($168^\circ/76^\circ$) presents a significant deviation of planarity (14°) which is thermodynamically unfavored due to the insertion of hydrophilic residues within the hydrophobic membrane core. On the other hand, topology II ($142^\circ/91^\circ$) represents an in-planar alignment onto the membrane with the adequate partition of both hydrophilic and hydrophobic core of the α -helix, including the insertion of the charged

His-7. Interestingly, the per-*O*-acetalized glycotriazole residue is pulled into the hydrophilic phase pointing towards the membrane interface (**Figure 33B**).

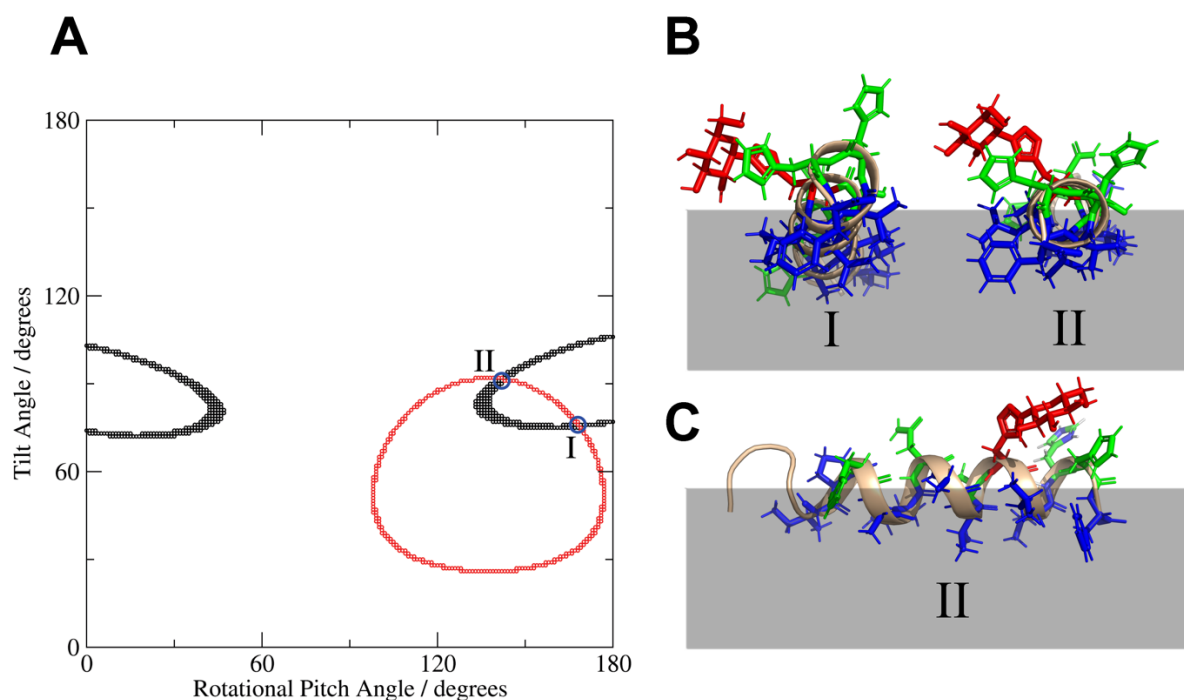


Figure 33: Alignments of [pOAcGlc-Trz-A¹⁴]-PS-2 in lipid bilayers shown as functions of the tilt and rotational pitch angles. Black points represent orientations that are in agreement within the respective ¹⁵N chemical shift whereas red points represent alignments that agree within the respective deuterium quadrupolar splitting. The intersection points shown as blue circles indicate orientations that simultaneously agree with both experimental parameters. Next to the contour plot the [pOAcGlc-Trz-A¹⁴]-PS-2 three-dimensional structure used to the topologies related to the intersection points (the N-termini shown in the back). Rotated view of the most thermodynamically favored alignment (II) is shown underneath. Hydrophilic residues are shown in green, hydrophobic residues in blue and the glycotriazole residue in red. The gray areas represent approximately the hydrophobic thickness of a bilayer.

The structure used for the simulations of [pOAcGlc-Trz-A¹]-HSP1-NH₂ corresponds to its analogue [pOAcNAc-Glc-Trz-A¹]-HSP1-NH₂, in which the sugar moiety is per-*O*-acetylate-*N*-acetylglucosamine, since the structure for [pOAcGlc-Trz-A¹]-HSP1 has not been calculated yet⁶³. Notwithstanding, since the NOESY spectra of both glycotriazole-peptides are roughly identical⁶³, it indicates that the structure of [pOAcNAc-Glc-Trz-A¹]-HSP1 might be used to represent the solid-state NMR data of [pOAcGlc-Trz-A¹]-HSP1-NH₂ in POPC:POPG:Ergosterol (3:1:1 molar ratio) bilayers.

A set of five topologies agrees simultaneously with the experimental data of [pOAcGlc-Trz-A¹]-HSP1-NH₂ (**Figure 34A**). Except for topology III (118°/80°), all of the other topologies present a significant deviation of planarity. Nevertheless, as III, topologies II (175°/72°) and V (137°/95°) insert hydrophilic residues within the hydrophobic membrane core. In contrast, the

hydrophilic residues are pulled into membrane interface for topologies I ($44^\circ/72^\circ$) and IV ($20^\circ/102^\circ$) (**Figure 34B**).

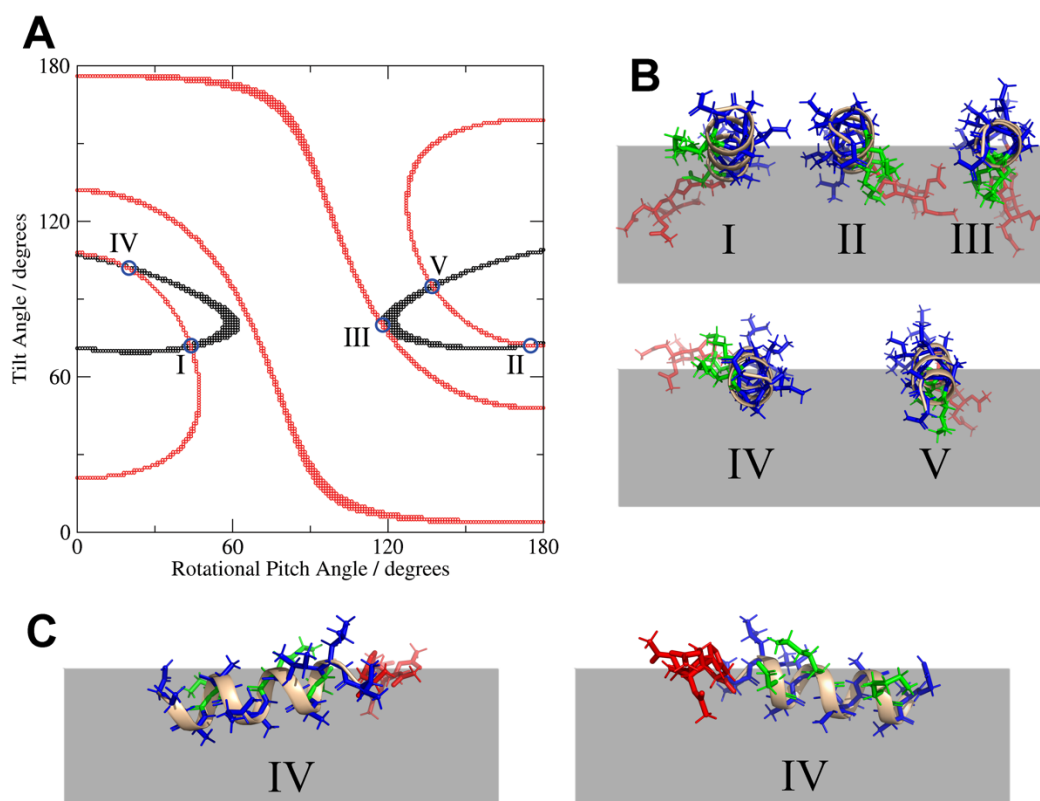


Figure 34: Alignments of [pOAcGlc-Trz-A¹]-HSP1-NH₂ in lipid bilayers shown as functions of the tilt and rotational pitch angles. Black points represent orientations that are in agreement within the respective ¹⁵N chemical shift whereas red points represent alignments that agree within the respective deuterium quadrupolar splitting. The intersection points shown as blue circles indicate orientations that simultaneously agree with both experimental parameters. Next to the contour plot the [pOAcGlc-Trz-A¹]-HSP1-NH₂ three-dimensional structure used to the topologies related to the intersection points (the N-termini shown in the back). Rotated view of the most thermodynamically favored alignment (IV) is shown underneath. Hydrophilic residues are shown in green, hydrophobic residues in blue and the glycotriazole residue in red. The gray areas represent approximately the hydrophobic thickness of a bilayer.

Below are summarized the experimental NMR parameters and topological data obtained for the thermodynamically most favorable membrane topologies of the glycotriazole-peptides (**Table 5**)

Table 5: Summary of the solid-state NMR parameters and membrane topologies for GtP-PS2 and GtP-HSP1-NH₂

Peptide	σ_{zz} (ppm)	$\Delta\nu_Q$ (kHz)	Orientation (ρ/τ)
GtP-PS2	73	44.5	$142^\circ/91^\circ$
GtP-HSP1-NH ₂	82	23.0	$20^\circ/102^\circ$

3.5. Discussion

3.5.1. *Ocellatins*

Mechanically oriented POPC bilayers containing Oce-LB1, -LB2 and -F1 were investigated by solid-state NMR spectroscopy. The similar relative line intensities and line widths observed in the ^{31}P NMR spectra of POPC bilayers containing each of the three peptides clearly indicate that this topological distribution is related to peptide dynamics rather than to some effect related to the membrane⁵⁶.

All ocellatins shown ^{15}N chemical shifts ≤ 76 ppm, indicating that the peptide helices adopt planar or approximately planar membrane orientations. Besides, energetic considerations and high complementary topological information gained from ^2H NMR allowed to assess in detail the peptide orientations, which indeed are related to in-plane alignments (**Figure 29**).

For Oce-LB1, topology II ($6^\circ/89^\circ$) clearly represents the suitable partition between hydrophilic and hydrophobic faces within the lipid bilayer (**Figure 29A, D, E**) and here it becomes clear the role of both Lys-7 and Lys-20, not only in delimiting the peptide hydrophobic perimeter as well as the membrane topology, but also as anchoring points of the peptide in the membrane^{73,74}. This is evident when the in-plane alignments II and III are compared to each other, inasmuch as III ($153^\circ/89^\circ$) would force the insertion of Lys-7 in the membrane, which is thermodynamically unfeasible.

The high similarities of the primary structures naturally lead to similar structural and topological features for the three membrane peptides. Nevertheless, the additional amino acids at the C-termini of the two longer peptide sequences induce subtle differences in comparison to the smallest ocellatin. The additional hydrophilic Asn-23 in Oce-LB2 slightly modulates tilt and rotational pitch angles, as observed for the most energetically favored topology I ($25^\circ/86^\circ$; **Figure 29B, E, G**) when compared to Oce-LB1. A slight deviation from the planarity is also observed when Oce-LB2 peptide topology I (**Figure 29B, E, G**) is compared to the most stable topology II of Oce-LB1 (**Figure 29A, D, G**).

Asn residues at peptide C-terminus have already been held responsible for the deviation from in-plane orientations, as observed for phylloseptin-1, whose alignment is more tilted in comparison to its analogues phylloseptin-2 and -3⁵³. This slightly tilted alignment is likely to

maximize the contact of Asn-23 with the hydrophilic face. This effect allied with a small difference in the helix internal rotation (pitch angle) leads His-16 at the membrane interface. Interestingly, although according to topology I Oce-LB2 is also anchored to the membrane by Lys-7 and Lys-20, the ^{15}N and ^2H solid-state NMR spectra of Oce-LB2 are characterized by broader lines, when compared to the NMR spectra of the other ocellatins, indicating a more heterogenous distribution of alignments and/or conformations.

In addition to Asn-23, Oce-F1 also carries additional -Lys-Leu residues at its C-terminus when compared to Oce-LB1. The extra Lys-24 is separated from Lys-20 by exactly one helical turn and, consequently, it lies on the same helical surface within the membrane interface (Oce-F1, Topology III, **Figure 29F, G**). This strategical position enables Oce-F1 to be anchored by three lysine residues (Lys-7, -20 and -24), suggesting that these residues modulate peptide pitch angle. Although the C-terminal Asn-23 seems to induce a slightly more tilted topology for Oce-LB2, the extra -Lys-Leu residues at Oce-F1 C-terminus may offset this effect, highly likely as a means of pulling Lys-24 into membrane interface. Indeed, since hydrophobicity and hydrophobic moment have a great influence on the alignment and penetration depth of amphipathic peptides, things become further complicated by possible ‘snorkeling’ effects of the lysine side chains^{68–71,75} and potential Leu-25 hydrophobic interactions with nonpolar tails^{76,77}, leading these interplays to modulate peptide tilt angle over Asn-23.

In summary, the energetically most favored topologies of the three ocellatins are outlined in **Figure 29G**. Lysines (highlighted in yellow) -7, -20 and -24 (for Oce-F1 only) are stretched toward membrane interface in order to enable the anchoring of the amphipathic helices^{73,74}, since the alkyl backbone is pulled into the membrane hydrophobic phase^{68,69} whereas the positively charged amino group is pulled into the membrane hydrophilic surface. Conversely, Lys-11 is clearly pulled into the hydrophilic zone for the three ocellatins, indicating that this residue has no function as an anchoring point.

3.5.2. Glycotriazole-peptides

Mechanically oriented POPC:POPS (3:1 molar ratio) bilayers containing [pOAcGlc-Trz-A¹⁴]-PS-2 were investigated by solid-state NMR spectroscopy. Both ¹⁵N chemical shift (75 ppm) and ²H quadrupolar splitting (44.5 kHz) indicate a homogeneous in-planar alignment of the glycotriazole-peptide labeled sites. The spectra thus allow the investigation of peptides' membrane alignment with high precision. Glycotriazole-peptide alignments that agree simultaneously with both experimental measurements are found in the intersections of contours map from the two measurements. However, the configuration associated with the intersection I (168°/76°) is characterized by a partial insertion of the α -helix structure inside the membrane (**Figure 33B**). Due the high energetic penalty of such arrangement, this possibility is excluded from further discussion. In contrast, the alignment represented by intersection II (141°/91°) is characterized by favorable localizations of both hydrophilic and hydrophobic residues as well as an in-planar orientation within the membrane. Hence, intersection II represents the lowest potential energy configuration (**Figure 33B, C**).

The comparison between the membrane topologies of the wild-type peptide PS-2⁵³ and of its glycotriazole derivative is of utmost importance for the study of these new class of compounds. At position 14, the threonine residue of PS-2 is replaced by a per-*O*-acetylated-glycotriazole residue and no significant differences are noticed as far as membrane topologies are concerned when both geometries are compared to each other (**Figure 35**). These results are expected, in as much as very similar NMR parameters were obtained for (3,3,3-²H₃-Ala-8, ¹⁵N-Leu-15)-PS-2 reconstituted into mechanically oriented POPC:POPS (3:1 molar ratio) bilayers ($\delta^{15}\text{N} = 74$ ppm, $\Delta\nu_Q = 46$ kHz).

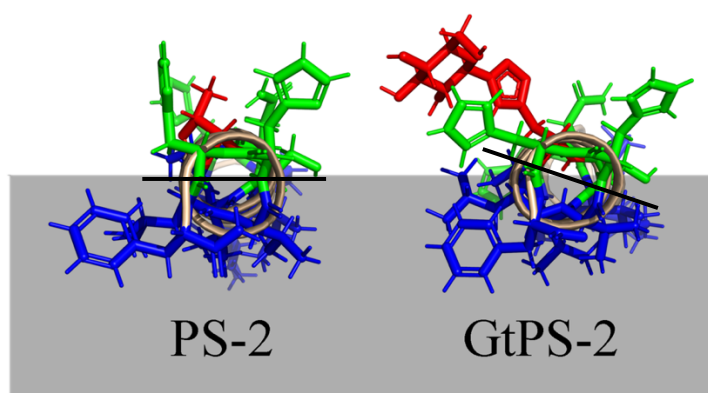


Figure 35: Membrane alignments of PS-2 (Resende et al., 2014)⁵³ and [pOAcGlc-Trz-A¹⁴]-PS-2 (GtPS-2). Hydrophilic residues are shown in green and hydrophobic residues in blue. The red sticks represent Thr-14 for PS-2 and the glycotriazole moiety for [pOAcGlc-Trz-A¹⁴]-PS-2. The gray areas represent approximately the hydrophobic thickness of a bilayer.

[pOAcGlc-Trz-A¹⁴]-PS-2 deviates 11° clockwise about its internal axis and with the result Pro-6, His-7, Ser-13 and Leu-15 are closer pulled into the interface whereas the glycotriazole residue remains into the hydrophilic core, as observed for Thr-14 in the wild-type sequence. It is noteworthy the role that Ser-13 plays in delimitating peptides partition within the membrane for both arrangements. However, since His-7 is slightly closer to the membrane interface for the GtP, it seems that GtP-PS2 pitch angle is modulated by both residues.

Comparative thermodynamic studies³⁹ of peptide-membrane interactions with anionic bilayers of the glycotriazole-PS-2 derivative and the wild-type species revealed a decrease in the enthalpic term ΔH° as well as decrease in both entropic ΔS° and absolute value of free Gibbs energy ΔG° terms for the glycotriazole-peptide. Thus, solid-state NMR measurements are in accordance with ITC data, since the reallocation of both polar and nonpolar residues into the interface dwindles the glycotriazole-peptide insertion into POPC:POPS bilayers. Besides, this outcome is also reflected by the smooth increase of -1° in [pOAcGlc-Trz-A¹⁴]-PS-2 tilt angle at C-terminus, leading residues at N-terminus less inserted into the bilayer

By and large, the reason why the per-*O*-acetylated-glycotriazole moiety does not enhance the affinity of PS-2 to phospholipid bilayers³⁹ may stem from the fact that the per-*O*-acetylated glucose side chain lies on the hydrophilic region of the membrane and, for this very particular case, it does not significantly change the membrane arrangement of the peptide. This outcome is a relevant piece of information since, up to our knowledge, there is no report in the literature about the membrane partition of unusual glycotriazole residues.

When the activities³⁸, structures³⁸, membrane topologies⁵³ and membrane interactions³⁹ of the three wild-type phylloseptins (-1, -2 and -3) are compared to each other, it is clear the importance of a hydrophilic residue at position 14 to ensure stronger activity and membrane interactions for PS-2 in relation to PS-1 and -3 (PS-2 carries a Thr-14 residue, whereas PS-1 and -3 carry an Ala-14). In this context, our research group has already invested some efforts on the removal of the acetyl groups of the per-*O*-acetylated-glucose, to obtain the polyhydroxylated-GtP derivative of PS-2, however we have hitherto obtained relatively small amount of the pure product³⁹. Our team is still working to improve this selective deprotection, inasmuch as the results obtained so far indicate that the polyhydroxylated derivative might significantly present stronger activities and membrane affinity in comparison to both the wild-type and the per-*O*-acetylated GtP derivative.

Mechanically oriented POPC:POPG:Ergosterol (3:1:1 molar ratio) bilayers containing [pOAcGlc-Trz-A¹]-HSP1-NH₂ were also investigated by solid-state NMR spectroscopy. Interestingly, the low intensity peak near -15 ppm demonstrates membrane disruption of chain order in the phospholipids at 1 mol% peptide concentration even in the presence of ergosterol, which is responsible to modulate membranes fluidity of fungi and protozoa^{78,79}. ¹⁵N chemical shift (82 ppm) indicates that [pOAcGlc-Trz-A¹]-HSP1-NH₂ presents approximately a planar membrane orientation, since the peak width also indicates an inhomogeneous alignment of the ¹⁵N-Leu-10 labeled site. In contrast, ²H quadrupolar splitting (23 kHz) indicates a homogeneous alignment of 3,3,3-²H₃-Ala-8.

Five intersections are found in the topology contour plot obtained from ¹⁵N and ²H simulations (**Figure 34A**). Topologies II (175°/72°), III (118°/80°) and V (137°/95°) are disfavored thermodynamically since all charged residues (Asp-4, Lys-7 and Lys-11) are pulled into the hydrophobic core and therefore they must be rejected for further discussion (**Figure 34B**). By the same token, topology I (44°/72°) is also disfavored thermodynamically since Asp-4 lies on the hydrophobic core. Conversely, topology IV (20°/102°) does not present an ideal partition either between both hydrophobic and hydrophilic cores of the α -helix with membrane faces, but polar residues are pulled into the membrane interface (**Figure 34B**).

The three-dimensional structure of [pOAcGlc-Trz-A¹]-HSP1-NH₂ shows an asymmetrical amphipathic partition between the respective hydrophobic and hydrophilic faces of the α -helix. This imperfection not only stems from the fact that ~72% of the residues that constitutes the glycotriazole-peptide are nonpolar, but also due to its distribution in the secondary structure, which makes that hydrophobic perimeter approximately occupies an 80% of the total (**Figure 36**). Slight deviations from planarity has been held responsible for the optimization of both hydrophobic moment and amphipathicity in bilayers, as observed in topological studies of Piscidin-1 and -3⁸⁰. Thus, the 12° deviation from the membrane surface seen in topology IV might lead to a deeper insertion of the hydrophobic residues near C-terminus into the membrane.

The tilting of the helix leads glycotriazole, Asp-4 and Lys-11 to be pulled into the interface, which modulate the glycotriazole-peptide pitch angle. It is expected that the flexibility of lysine sidechain allows the charged amino group of Lys-11 to snorkeling out toward the hydrophilic core⁶⁸⁻⁷² and anchor the peptide⁸¹⁻⁸³, as reported for ocellatins. In addition, aromatic and

charged residues have also been described as anchoring points for peptides in phospholipid bilayers^{68,82,84} hence it stands to reason that Asp-4, Lys-11 and glycotriazole residues anchor the α -helix in the membrane. In contrast, Lys-7 does not act as anchor since it is virtually pulled into the hydrophilic core due to peptide tilting at N-terminus.

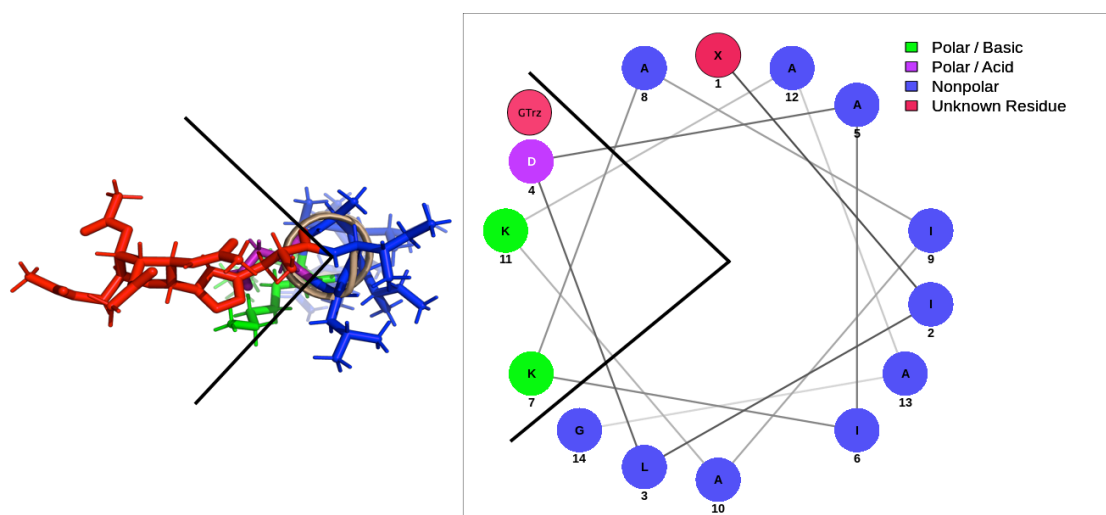


Figure 36: Schiffer-Edmundson wheel projection of [pOAcGlc-Trz-A¹]-HSP1-NH₂. Hydrophobic residues are shown in blue, positively charged residues are shown in green, negatively charged residues are shown in purple and the glycotriazole residue is shown in red. The pair of black lines delimit the separation between the hydrophilic and hydrophobic faces. GTrz circle was added manually in accordance to the three-dimensional structure of [pOAcGlc-Trz-A¹]-HSP1-NH₂. The hydrophobic perimeter is represented by the length of the external circumference delimited by these pairs of solid lines. This simulation was performed at <http://lbqp.unb.br/NetWheels/>.

Up to our knowledge, there is no topological information on the literature about the membrane interaction of HSP1-NH₂, which impossibilities a direct analysis of the influence of the glycotriazole residue on the membrane topology of the wild-type peptide, as done above for PS-2. Nevertheless, the topological outcome for GtP-HSP1-NH₂ indicates that the glycotriazole residue lies on the membrane interface. As for the GtP derivative of PS-2, this residue was observed on the hydrophilic part of the bilayer, hence these results indicate the existence of hydrophilic interactions between the per-*O*-acetylated-glycotriazole residue and the membrane, which is very likely related to its eleven hydrogen bond acceptor atoms.

Chapter 4: Computational and biophysical studies on the membrane interactions of ocellatins

4.1. Introduction

On the one hand, several biophysical methods have demonstrated to be reliable in the study of peptide-membrane interactions with biomimetic membrane models. Peptide-membrane interactions are related to fundamental physicochemical parameters within an intricate environment. However, the combination of many biophysical techniques, such as surface plasmon resonance spectroscopy (SPR), circular dichroism (CD), nuclear magnetic resonance spectroscopy (NMR), atomic force microscopy (AFM), X-Rays and isothermal titration calorimetry (ITC) among others, have enabled to gain insight into peptide-membrane interactions with a high degree of accuracy at atomic scale.

On the other hand, computer-based models have proven to be a powerful tool for studying and predicting a wide variety of chemical and biochemical processes, such as intrinsic strain of organic molecules, thermodynamics of ligand binding to proteins, conformational transitions and peptides dynamics in fluid membranes. Moreover, molecular simulations offer various physical quantities, which are often inaccessible experimentally, such as the prediction of the preferred orientation of a drug when bound to the target enzyme, to comprehend the molecular principles underlying countless phenomena.

This chapter, therefore, aims to gain more insight into the ocellatins-membrane interactions through different biophysical and computational approaches.

4.1.1. Isothermal titration calorimetry (ITC)

ITC isothermal titration calorimetry is one of the most used techniques for the thermodynamic description of different biomolecular systems. As in other techniques, ITC allows the study in biomimetic environments of membranes, such as phospholipid vesicles and micelles⁸⁵.

The main application of ITC is in the study of the thermodynamic parameters of a binding reaction. It not only allows the measurement of the binding enthalpy ΔH° , but also performs a complete thermodynamic analysis of the interaction, including the free binding energy of ΔG° , the binding entropy ΔS° and the variation in heat capacity ΔC° ^{85,86}. Moreover, these parameters can be used in calculating the interaction constant (K) and stoichiometric coefficient (n)⁸⁷. ITC has also been used to study secondary processes, which accompany peptide-membrane interaction, such as peptide-induced membrane permeabilization, changes in the lipid phase, membrane-induced peptide-peptide association, protonation reactions on the surface membrane and conformational changes of the peptide⁸⁸⁻⁹¹. Considering that the interaction of peptides with membrane lipid bilayers involves the breakdown and formation of intermolecular interactions, the ITC uses as a probe the direct measurement of the heat flow associated with these phenomena, making this technique very useful in investigating peptide-membrane interactions⁹².

ITC works basically with a thermal core equipped with two cells, one as reference and the other containing the sample. The two cells are set to the desired experimental temperature. The titrate is loaded into a syringe, which is attached to a very precise injection device, and when this titrate is injected into a series of small aliquots in the cell containing the titrant, an energy disturbance is generated that evolves over a period of time, if any interaction occurs, until the bonding reaction reaches the equilibrium⁹³. Thus, for each change of heat measured in the cell, a signal is acquired. Therefore, if it is an exothermic process, the signal is represented by a negative deflection whereas should it be endothermic, it will be represented by a positive deflection. As the temperature of the two cells becomes equal, the signal returns to its initial position. The first peaks are more intense because most of the injected titrate is linked to the titrant. Once the titrant becomes saturated with the titrate, less titrate will bind as the injections follow, and therefore less heat will be generated.

By the integration of each signal using mathematical models, the raw data is transformed into a plotted function of the titrant molar ratio per molecule titrated in the cell. Thus, whereas each black dot on the curve represents an individual heat signal, the solid black line represents the best fit for the connection algorithm used in the software. Hence, from the plotted function the interaction enthalpy ΔH° is determined as the difference between the maximum and minimum values of the titrate heat (y axis), stoichiometric coefficient is referred as the midpoint of the

sigmoidal curve and both affinity (K_a) and dissociation (K_d) constants are related to both the concentration and the slope of the sigmoidal function (**Figure 37**).

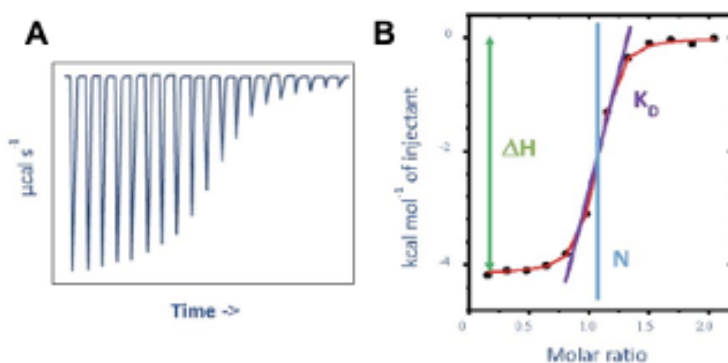


Figure 37: (A) raw ITC data (B) binding isotherm from ITC experiment (from Frasca 2016)⁹⁴.

4.1.2. Surface plasmon resonance spectroscopy (SPR)

Because of its capability of measuring quantitative binding affinities and kinetics in real-time, surface plasmon resonance has emerged as a sensitive and rapid technique for the study of binding interactions of antimicrobial peptides or glycopeptides^{95–97} with membranes.

SPR spectroscopy⁹⁶ is based on the measure of a change in the refractive index of the medium close to a metal surface, and it is used to monitor the binding of peptides to bilayers immobilized on the metal surface. The process exploits the generation of plasmon resonance on the surface of a thin metal and the total internal reflection of light at the solution-surface interface. Thus, it produces an evanescent wave, which is an oscillating electromagnetic field spatially concentrated in the vicinity of the source that travels a short distance through the solution and allows the real-time measurement of the peptide binding to the surface of the biomimetic membranes. Thus, in order to detect the binding of a peptide to a membrane, peptides are injected into an aqueous solution which is in continuous flow. Polarized light is directly cast through a prism to the thin metal surface in which the plasmon of the surface is generated at a certain critical angle in relation to the incident light. This critical angle is dependent on the refractive index of the intimately vicinity (300 nm above the surface of the gold film) and it changes when peptide binds to the immobilized bilayers. Therefore, if the interaction between the peptide and the membrane occurs, the refractive index of the gold film surface changes and as a consequence the signal intensity increases. The real-time response is given in the form of a sensogram and the response units (RU) are used to describe the increase in intensity of the signal (**Figure 38**).

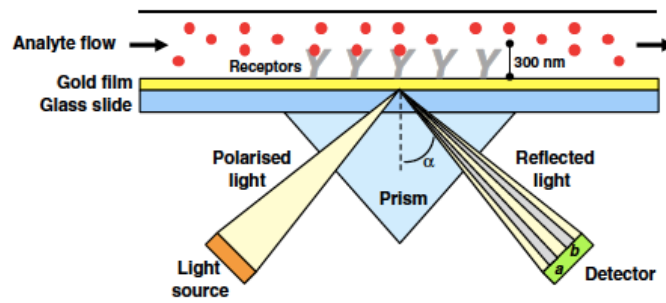


Figure 38: Simplified scheme of SPR operating mechanism (from Patching *et. al*)⁹⁶.

Many physicochemical parameters can be obtained from the shape of sensograms. Binding sites go on to become occupied when peptides are injected into the flow cell and they bind with the immobilized bilayers. This process is known as the association phase and is characterized by a change in the initial critical angle a , in which the RU signal starts increasing in a curve-shaped manner that can be used to measure the association rate (k_{on}). A steady state is reached when the RU signal arrives at its maximum value, characterized by a final change in critical angle b . The maximum RU value, which sometimes becomes a plateau, is related to the equilibrium between those peptides which bind to the membrane and those which dissociate^{95,96}. Hence, it can be used to measure both binding affinity (k_a) and dissociation (k_d) constants. Thereafter, the dissociation phase comes when binding sites become unoccupied because of the removal of peptides from the continuous flow. Thus, RU signal decreases in a convex-shaped manner, which can be used to measure the dissociation rate (k_{off}). At the end of the experiment, the metal surface is regenerated and returns to the critical angle a (**Figure 39**).

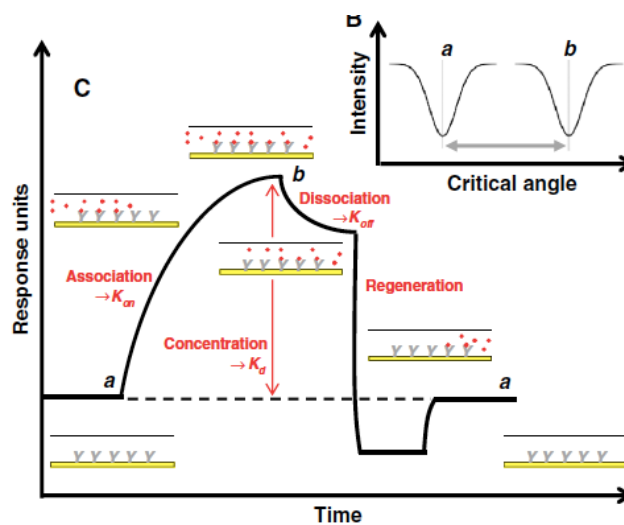


Figure 39: General sensogram showing the stages of interaction peptide-bilayer interaction (from Patching *et. al*)⁹⁶.

4.1.3 Molecular dynamics (MD)

Among all the methods to investigate membrane-associated peptides, both solution NMR and solid-state NMR spectroscopies are the only techniques that can depict peptides structures and their orientations in membranes at atomic scale. These approaches, however, measure the time-averaged composite of several conformations and orientations⁹⁸, leading to the averaged structure and alignment of peptides. Conversely, the computational study of peptides not only yields large sets of individual structures in high detail, but also their dynamic properties in both aqueous media and membranes. Hence, through molecular dynamics, the activity of antimicrobial peptides can be more thoroughly analyzed underpinning the structure-activity relationship in determining their membrane disruptive properties.

In essence, molecular dynamics simulations combine the equations of motion of classical mechanics, principally Newton's law, and the potential energy through which the forces that act on each atom are defined as the negative derivative of the potential energy [18]⁹⁹. Hence, trajectories, defined as the array of time-dependent configurations for each atom, are the result of the simultaneous integration of Newton's equation of motion for each atom⁹⁸.

$$F_i = m_i a_i = -\nabla_i V = -\frac{dE}{dr_i} \quad [18]$$

The potential energy, generally referred as "force field", is the sum of bond and angle energies, bond rotation energy and the energy of nonbonded electrostatic and van der Waal interactions, all of those parametrized from X-ray, IR, Raman spectroscopy data and quantum mechanical calculations⁹⁸.

It exists a whole host of force fields designed for different systems, although the choice of the force field depends on what kind of system one wants to study and what one is interested in studying. For the study of polypeptides, not least, it exists several class I force fields such as AMBER, CHARMM and GROMOS96, among other⁹⁸.

For the MD simulations run in this work, AMBER has been the force field used to study OcelB2 dynamics in membranes. This mathematical model is generally described as [19]¹⁰⁰:

$$\begin{aligned}
E_{total} = & \sum_{bonds} K_r (r - r_{eq})^2 + \sum_{angles} K_\theta (\theta - \theta_{eq})^2 \\
& + \sum_{dihedrals} \frac{1}{2} K [1 + \cos(n\phi - \gamma)] + \sum_{i < j} \left[\frac{A_{ij}}{r_{ij}^{12}} - \frac{B_{ij}}{r_{ij}^6} + \frac{q_i q_j}{\epsilon R_{ij}} \right]
\end{aligned}
\tag{19}$$

Where the first three terms represent the energy gap between a geometry at the equilibrium, in which bond lengths, bond angles and dihedral angles have ideal values, and the genuine geometry. On the other hand, the last term is related to nonbonded van der Waals and electrostatic interactions¹⁰⁰.

Finally, the MD simulations were carried out with GROMACS MD package, since apart from being designed for simulations of lipids, proteins and nucleic acids, it is one of the fastest MD simulations program.

4.2. Objectives

1. Perform Isothermal titration calorimetry experiments of ocellatin-LB1, -LB2 and -F1 with POPC LUVs in order to get more insight into their thermodynamics of binding to POPC membranes.
2. Perform surface plasmon resonance (SPR) spectroscopy experiments of ocellatin-LB1, -LB2 and -F1 with POPC bilayers in order to get more insight into their kinetics of binding to POPC membranes.
3. Perform MD simulations of Ocellatin-LB2 in POPC bilayers in order to get more insight into its inhomogeneous alignment according to ¹⁵N and ²H NMR broad line shapes.

4.3. Methods

4.3.1. Isothermal titration calorimetry (ITC)

Isothermal titration calorimetry (ITC) experiments were performed at 25 °C with a high-precision VP-ITC Microcalorimeter® (Malvern Instrument Ltd, Worcestershire, UK) for 35 µM peptide solutions in 10 mM Tris-HCl, pH 8.5 containing 20 mM NaCl. The ITC equipment was electrically and chemically calibrated before performing the experiments. All solutions and buffers employed in the experiments were filtered and degassed under vacuum (140 mbar) for eight minutes. The peptide solutions in the calorimeter cell were titrated with fifty-one successive injections of 20 µM POPC LUVs (the first 1 µL injection was discarded in order to eliminate diffusion effects of the material from syringe to calorimeter cell and this injection was followed by fifty injections of 5 µL). Injection times of 2 s with intervals of 240 s have been used in the experiment. A similar titration was performed with buffer in the calorimeter cell using the same lipid suspensions to determine the corresponding heats of dilution, which were then subtracted from the heats determined in the corresponding peptide-to-lipid binding experiments. To determine the heat produced by the peptide-to-lipid interaction, each peak of the calorimetric curve was integrated following standard procedures as described by Wieprecht and Seelig, 2002¹⁰¹. The total lipid concentration was used in the estimation of the binding degree as well as in the determination of the thermodynamic binding parameters¹⁰². The raw data were analyzed with the software Microcal Origin 5.0 (OriginLab Corporation, Northampton, USA) for ITC, supplied together with the microcalorimeter.

4.3.2. Surface Plasmon Resonance (SPR)

SPR measurements were performed at 25 °C using 10 µL·min⁻¹ flow rate for LUVs immobilization and peptide-membrane interactions and recorded at 850 nm on a SPR Navi™ 200 instrument (BioNavis Ltd., Ylöjärvi, Finland). SiO₂ sensor chips (SPR102-SIO2) were used to phospholipid immobilization, which were washed *in situ* in the flow channel with sequential 5 min injections of 5% Hellmanex® III (Sigma, St Louis, MO), 2-propanol and Milli-Q water immediately before each experiment. For each measurement, the sensor chip was first subjected to the running buffer (10 mM Tris-HCl buffer, pH 8.5) and then 0.05 to 1 mM POPC solutions during approximately 15-20 min until baseline stabilization. The experiments consisted of 50 µL injections of peptide solutions at 45 µM, in the running buffer. The surface partition constant (*K*) of the peptide-membrane interactions were obtained from SPR

experiments by fitting the data to the following equation [20] taking the electrostatic interaction into account ¹⁰³:

$$\Delta RU_{eq} = \Delta RU_{eq(max)} \left[\frac{Kc_L}{\exp\left(\frac{Z_p \Psi F}{RT}\right) + Kc_L} \right] \quad [20]$$

where ΔRU_{eq} is the change in the observable RU_{eq} intensity at 15 min after peptide injection, and $\Delta RU_{eq(max)}$ is the maximum change of the observable RU_{eq} obtained by fitting the raw data, Z_p is the charge on the peptide, Ψ , is the membrane surface potential, F is Faraday's constant, R is the universal gas constant and T is temperature. The concentration of accessible lipid (considering the outer leaflet of the membrane bilayer, which represent 60% of the total lipid concentration) is represented by c_L . The quantification of the total phospholipid content immobilized in the sensor ship was performed as described by Junior *et al.* 2017 ³³.

The membrane surface potential, Ψ , was calculated from zeta potential and considering the exponential decay of the electrostatic potential ^{104,105} according to Equation [21].

$$\Psi = \zeta e^{\kappa x} \quad [21]$$

Where ζ represents the zeta potential; κ , the inverse of the Debye length; and x , the hydrodynamic layer thickness, in this case assumed to be at $x = 0.24$ nm from the POPC liposome surface ^{106,107}. The zeta potentials of the 0.05 to 1.00 mM POPC solutions were measured at 25 °C in a Malvern Zetasizer Nano ZS[®] particle analyzer (Malvern Instrument Ltd., Worcestershire, UK) as described by Junior *et al.* 2017 ³³. The zeta potential value used in Eq. 2 (-5.2 mV \pm 0.2) corresponds to the mean of the ζ values of POPC solutions.

4.3.3. Molecular dynamics simulations

MD simulations of the membrane-bound Oca-LB2 peptide were performed in a POPC bilayer consisting of 128 lipids (64 molecules in each membrane leaf) and 7758 TIP3P water molecules. SLIPID force field was used to describe the lipid molecules ¹⁰⁸, whereas the AMBER99SB-ILDN force field was used for the description of the other components ¹⁰⁹.

Model preparation, simulations and analyses were performed with the GROMACS software package¹¹⁰ (version 2020) and Visual Molecular Dynamics¹¹¹ software.

First, a pre equilibrated POPC bilayer was inserted in the center of a simulation box. Thereafter, the three-dimensional structure of Ose-LB2 with the respective orientation determined by solid-state NMR (ρ , τ) was incorporated to the system 2 nm apart from membrane surface. Membrane and peptide were solvated with 60 TIP3P¹¹² water molecules (randomly added) per phospholipid. The system was inspected to remove water molecules added inside the membrane hydrophobic core defined by the limit of the ester oxygens (O30/O31 and O20/21) and the last carbon of the aliphatic tail (C316). The simulation box was then subjected to a standard energy minimization protocol, 10.000 steps of steep descent and conjugated gradient, where the peptide heavy atoms were kept under position restraint by a harmonic potential ($1.000 \text{ kJ}\cdot\text{mol}^{-1}\cdot\text{nm}^{-2}$). After energy minimization, the system was equilibrated in two phases. First at 293 K for 100 ns on the NVT ensemble (constant volume V , temperature T , and number of particles N) using a V-Rescale temperature coupling¹¹³ together with the LINCS algorithm¹¹⁴ to constrain all bonds. Long range electrostatics were treated via particle-mesh Ewald¹¹⁵ combined with a 1.4 nm direct space cutoff for van der Waals and Coulomb interactions. After, at 293 K for 100 ns on the NPT ensemble (constant pressure p , temperature T , and number of particles N) using a Nosé–Hoover thermostat¹¹⁶ and Parrinello–Rahman barostat at 1 bar¹¹⁷ with semi-isotropic pressure coupling.

To speed up the membrane peptide interaction, the peptide insertion phase was executed at 480 K¹¹⁸. The system was heated from 293 K to 480 K applying Gromacs simulated annealing ramp algorithm (1 ns at 293 K, from 293 to 480K in 3 ns, 1 ns at 480 K) under position restraint potential ($1.000 \text{ kJ}\cdot\text{mol}^{-1}\cdot\text{nm}^{-2}$). The system was reequilibrated at 480 K in two phase step, 100 ns on the NVT ensemble and 100 ns on NPT ensemble as described in the preparation phase. The system was then simulated at 480 K for 100 ns to allow the peptide insertion. To keep the original fold, α -helix hydrogen bonds were distance restrained ($1.000 \text{ kJ}\cdot\text{mol}^{-1}\cdot\text{nm}^{-2}$). In general, a complete insertion and stabilization of peptide-membrane is obtained within 20~30 ns. After the peptide insertion, the temperature was returned to 293 K applying simulated annealing protocol (1 ns at 480 K, from 480 to 293K in 3 ns, 1 ns at 293 K) and reequilibrated in two phase step, 100 ns on the NVT ensemble and 100 ns on NPT ensemble as described in the preparation phase.

Finally, the system was simulated in the absence restraints at 293 K for 1000 ns in the NPT ensemble (constant pressure p , temperature T , and number of particles N), using a Nosé–Hoover thermostat¹¹⁶ and Parrinello–Rahman barostat at 1 bar¹¹⁷ with semi-isotropic pressure coupling. A time step of 2 fs was used for all simulations, together with the LINCS algorithm¹¹⁵ to constrain all bonds. Long range electrostatics were treated via particle-mesh Ewald¹¹⁴ combined with a 1.4 nm direct space cutoff for van der Waals and Coulomb interactions. Snapshots were saved every 50 ps.

The studies of MD were carried out by the collaborator Dr Francisco Gomes Neto from Fiocruz.

4.4. Results

In order to better characterize the membrane association of the three ocellatins, we have investigated their interactions with large unilamellar vesicles (LUVs) in a quantitative manner by isothermal titration calorimetry (ITC). In a recent publication, our group investigated the thermodynamics of interactions of these three ocellatins with POPC:POPG (3:1) LUVs under similar conditions³⁰. Nevertheless, here we present thermodynamic studies in presence of POPC LUVs in order to keep a similar zwitterionic media to that used in solid-state NMR experiments. For comparison purposes, all experiments consisted of titrations of 20 μM POPC LUVs into the 35 μM peptide solutions.

The heat flow changes when the three ocellatins bind to the phospholipid vesicles are presented in **Figure 40A-C** and the respective binding isotherms are shown in **Figure 40D-F**. The raw data (**Figure 40A-C**) obtained for each titration reveal significant affinity to phospholipid vesicles^{101,119} and suggest a higher affinity of Oce-F1 with POPC LUVs when compared with the other analogues. The thermodynamic parameters (ΔG° , ΔH° , ΔS°), the apparent binding constants (K_{app}), and the stoichiometric coefficients (n) were determined by non-linear curve fitting using the model of equivalent binding sites (red line in **Figure 40D-F**). In all systems, the entropic contributions during the peptide-membrane binding process exceed the enthalpic ones, although at different proportions, being fifteenfold for Oce-LB1, fivefold for -F1 and roughly twofold for -LB2.

Despite a higher ΔG° value is observed for the Oce-LB1-POPC interaction in comparison to that of -LB2, a greater enthalpic contribution is related to the membrane interaction of Oce-LB2. Interestingly, the balance between enthalpic and entropic terms lead to similar ΔG° values for the interactions of both -LB1 and -F1 with POPC LUVs. The parameters of the interactions with anionic POPC:POPG LUVs are also listed in **Table 6**³⁰.

Either in the presence of zwitterionic or anionic phospholipids, the relative magnitude of both K_{app} and ΔG° absolute values is Oce-F1 > Oce-LB1 > Oce-LB2. When each ocellatin is considered, greater K_{app} and ΔG° absolute values are observed for peptide interactions with the anionic LUVs.

The affinity constants and thermodynamic parameters obtained for the three ocellatins in presence of both POPC and POPC:POPG LUVs are summarized in **Table 6**. Either in the presence of zwitterionic or anionic phospholipids, the relative magnitude of both K_{app} and ΔG°

absolute values is Oce-F1 > Oce-LB1 > Oce-LB2. When each ocellatin is considered, greater K_{app} and ΔG° absolute values are observed for peptide interactions with the anionic LUVs.

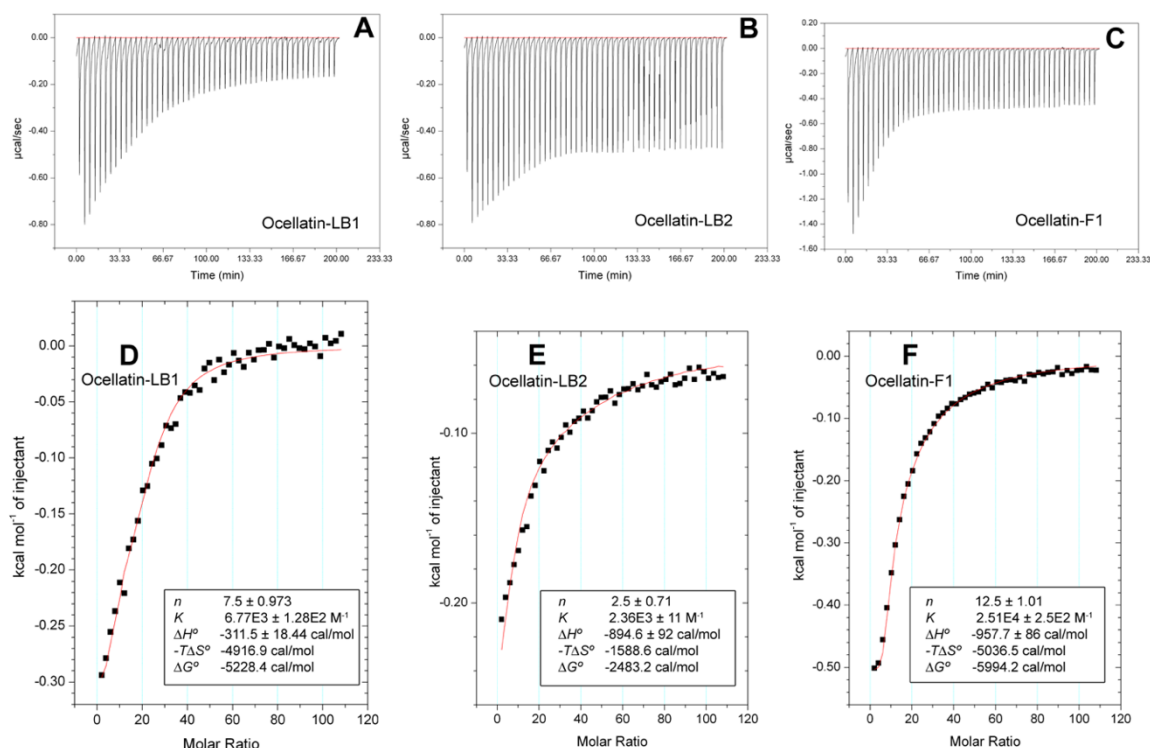


Figure 40: Isothermal titration calorimetry of ocellatin peptides in 10 mM Tris-HCl, pH 8.5, containing 20 mM NaCl with POPC LUVs (20mM stock solutions in 10 mM tris-HCl, pH 8.5 containing 20 mM NaCl). The heat flow for (A) ocellatin-LB1 (35.3 μ M), (B) Ocellatin-LB2 (36.1 μ M) and (C) ocellatin-F1 (18.2 μ M) injection as a function of time (raw data). The enthalpy as a function of the (D) Ocellatin-LB1, (E) Ocellatin-LB2 and (F) Ocellatin-F1 to POPC molar ratio. The baseline was corrected, and the heat of dilution subtracted from each experimental point.

Table 6: Thermodynamic parameters obtained from ITC in both POPC and POPC:POPG (3:1 mole/mole)³⁰ membranes

		K_{app}	ΔH°	$-T\Delta S^\circ$	ΔG°
		($10^3 \cdot M^{-1}$)	($10^3 \cdot \text{cal/mol}$)	($10^3 \cdot \text{cal/mol}$)	($10^3 \cdot \text{cal/mol}$)
Oce-LB1	POPC	6.80	-0.31	-4.92	-5.23
	POPC:POPG (3:1)*	10.4	-0.95	-4.50	-5.45
Oce-LB2	POPC	2.36	-0.89	-1.59	-2.48
	POPC:POPG (3:1)*	9.62	-1.11	-4.32	-5.43
Oce-F1	POPC	25.1	-0.96	-5.04	-5.99
	POPC:POPG (3:1)*	29.3	-1.19	-4.89	-6.08

Isothermal titration calorimetry of ocellatin peptides in 10 mM Tris-HCl, pH 8.5, containing 20 mM NaCl with either POPC or POPC:POPG (3:1) LUVs (20 mM stock solutions in 10 mM tris-HCl, pH 8.5 containing 20 mM NaCl). *Data obtained by Gomes *et al.*, 2018³⁰

Surface partition constants (K) of the interactions between ocellatins and zwitterionic model membranes were also assessed by surface plasmon resonance spectroscopy (SPR). POPC LUVs were immobilized on a SiO₂ sensor chip in the presence of Tris-HCl running buffer before

peptide injection at different concentrations. The RU signal intensity increase as a function of the lipid concentration (**Figure 41D**) indicates once more the peptide-membrane binding. The profiles of peptide-membrane binding sensograms of Oce-LB1, -LB2 and -F1 (**Figure 41A-C**) are similar to each other. Nevertheless, markedly higher response levels are observed for the membrane interactions of Oce-F1 in comparison to those of the other peptides.

Examination of each sensogram reveals different binding kinetics with noteworthy differences in both association and dissociation rates for POPC surfaces. In fact, the shape of the sensograms indicate that the peptides bind to the lipid surface in a biphasic manner⁹⁵. **Figure 4D** shows the simulations according to Equation [20] of the RU signal intensity as a function of the phospholipid concentration. The SPR titrations (**Figure 41D**) yielded surface partition constant K of 7000 M^{-1} , 3100 M^{-1} and 22500 M^{-1} for Oce-LB1, -LB2 and -F1, respectively.

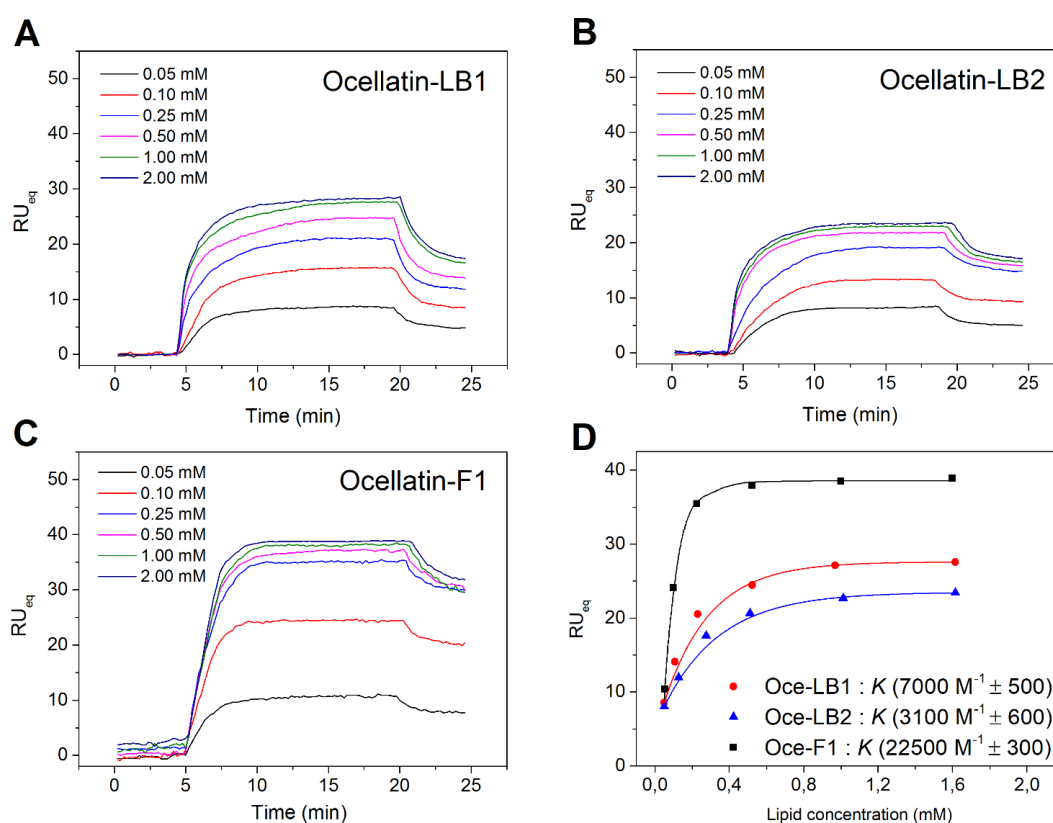


Figure 41: SPR sensograms for the bilayer interaction of (A) Ocellatin-LB1, (B) Ocellatin-LB2 and (C) Ocellatin-F1. POPC bilayers were immobilized onto the surface of a SiO₂ sensor chip and the peptides were injected at 2.6, 5.12, 11.25, 22.5 and 45 μM concentrations in 10 mM Tris-HCl buffer, pH 8.0, containing 20 mM NaCl. (D) Comparative sensogram for the bilayer interaction of the three ocellatins at $\sim 50 \mu\text{M}$ (Oce-LB1 and -LB2 at 52 μM and -F1 50 μM). (E) Non-linear fitting of RU intensities as a function of peptide-POPC molar ration of Oce-LB1 (red), Oce-LB2 (blue) and Oce-F1 (black).

Finally, in light of the broader ¹⁵N and deuterium NMR peak widths observed for Oce-LB2, we decided to perform MD simulations to better understand the nature of the peptide association to POPC bilayers. Hence, we set out to determine the trajectory of the membrane interaction of

Oce-LB2 and the topological flexibility was monitored by following the helix tilt and pitch angles over time, in comparison to the values determined by solid-state NMR spectroscopy.

The peptide was originally placed ~ 2 nm above the phospholipid bilayer in the water phase, with an alignment relative to the membrane normal representing the rotational pitch and tilt angular pair determined by solid-state NMR spectroscopy (**Figure 42**). Strong distance restraints were applied to the backbone hydrogen bonds to keep the original helical conformation. The evolution of the interaction between ocellatin-LB2 and the POPC bilayer was monitored through two parameters: (i) the tilt angle of the peptide as described in the Methods section (starting from $\tau=86^\circ$: **Figure 42A**) and (ii) the distance between the amide nitrogen of the labelled site (^{15}N -Leu17) and the membrane (**Figure 42B**, starting at 20 Å). Here we used the average position of the nitrogen in the choline head group as reference (**Figure 42B**). The average position of other atoms such as the ester oxygens, which represents the transition region for the hydrophobic core of the membrane were also monitored.

As the simulation begins the peptide gets closer to the membrane, changing its position in the simulation box (**Figure 42C**). **Figure 42A-B** shows a constant decrease in the tilt angle and a decrease in the distance between the peptide and the nitrogen of the choline head group of POPC. At 0.2 ns, the peptide touches the membrane, its insertion starts by dipping first the N-terminal region into the bilayer (**Figure 42C**). This process, accompanied by a constant change of the tilt angle, continues until 0.8 ns. At this time, the peptide finally positions itself planar within the membrane surface with the hydrophilic residues pointing out the hydrophilic region (**Figure 42C**). Interestingly, from this time interval to the end of the insertion phase (4 ns), the peptide's pitch angle keeps fluctuating within a range ($\rho=24.18^\circ \pm 0.44$) relatively close to the angle determined by solid-state NMR whilst the peptide tilt angle undergoes considerable fluctuations until 0.8 ns, probably sampling the best level of insertion (**Figure 42B**).

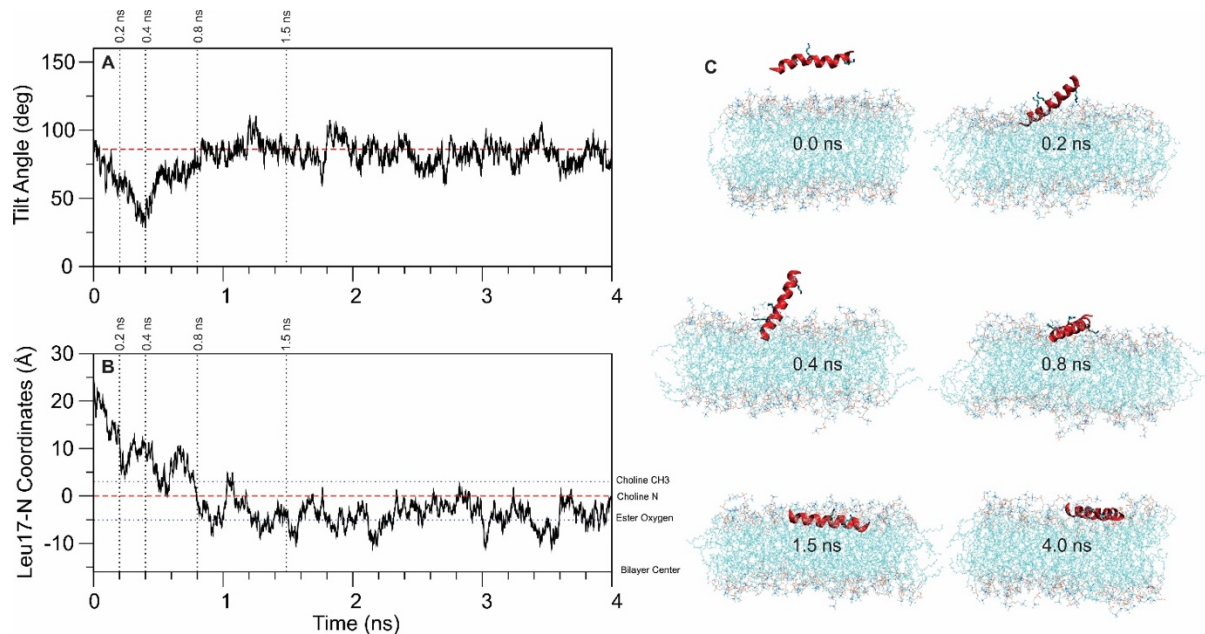


Figure 42: Setup of the Ocellatin-LB2-POPC bilayer model. Initially the peptide is included in the simulation box ~ 20 Å apart from the bilayer surface at the topology derived from solid-state NMR data ($t = 86^\circ$ and $r = 26^\circ$). Different snapshots are shown to represent stages of the peptide insertion into the bilayer. Variations during the simulation of (A) the tilt angle and (B) the insertion depth relative to the distance between the isotopically labelled ^{15}N -Leu-17 site and the lipid bilayer. (C) Lateral perspectives of the selected snapshots are shown to the right.

The final coordinates of the insertion phase simulation were used as the starting model for the unrestrained simulation of the complexed ocellatin-LB2/POPC bilayer. The Ocellatin-LB2 MD simulation was conducted for 1000 ns. **Figure 43A-B** show the variation of the rotational pitch and tilt angular pairs during the evolution of the simulation. Interestingly, no significant variation of the rotational pitch angle is observed throughout the simulation trajectory and almost all of the structures agree with the topological data obtained by solid-state NMR spectroscopy within $\pm 3^\circ$. On the other hand, more pronounced oscillations of the tilt angle are noticed. Two distinct topological ranges centered at $\tau = 86^\circ$ and 94° are observed during the first 500 ns of simulation. Whereas the first range corresponds to the tilt angle derived from the solid-state NMR data (**Table 7**), the second range indicates a different degree of insertion, nevertheless oscillations of the tilt angle suggest wobbling upon membrane binding.

Discarding the first 200 ns of simulation, the dwell time at $\tau \sim 86^\circ$ reaches 49% of the trajectory and it increases to 62% for the last 200 ns of simulation (800 to 1000 ns). These results indicate that helix tilting is similar to that determined from solid-state NMR parameters and that a clear partition between hydrophilic and hydrophobic faces within the membrane clearly restraints azimuthal rotation. However, it is evident that the C-terminal portion of the helix wobbles up and down throughout the trajectory in order to maximize the contact of Asn-23 with the

hydrophilic face. This topological flexibility is very likely represented by the broader ^{15}N -Leu17 and $^2\text{H}_3$ -Ala10 resonances of Oce-LB2 in comparison to those of the other ocellatins.

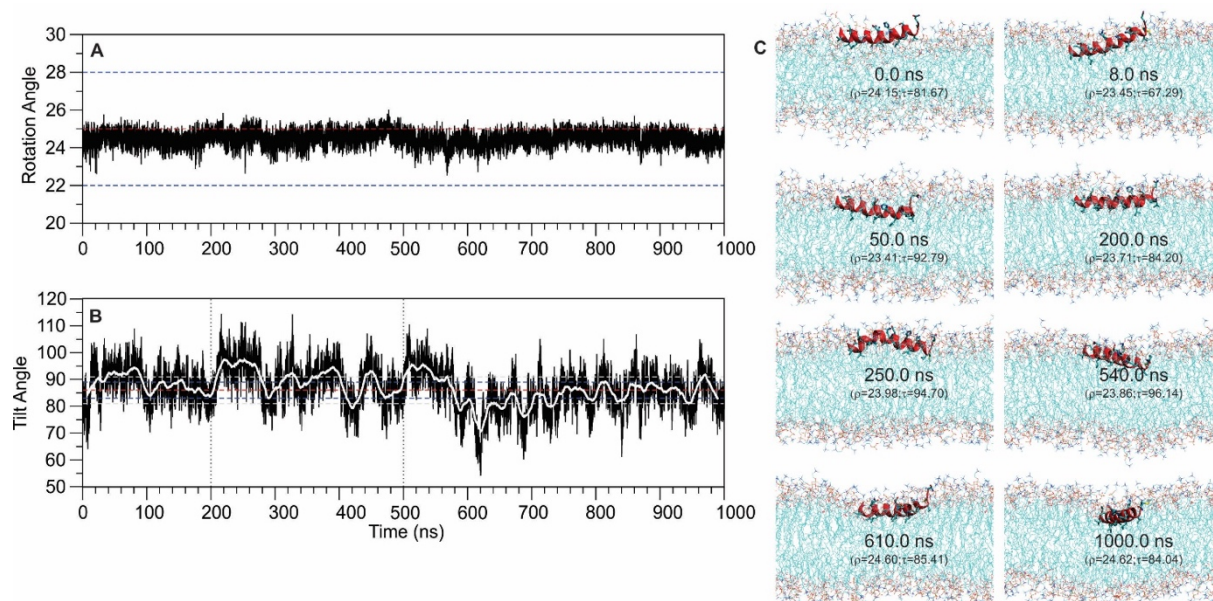


Figure 43: MD simulations of Ocellatin-LB2 reconstituted into POPC bilayer. (A) Rotational pitch and (B) tilt angles as function of the simulation time. The red dotted lines represent the topology determined from solid-state NMR data data ($\tau = 86^\circ$ and $\rho = 26^\circ$) and the blue dotted lines represent the respective variations ($\Delta\tau$ and $\Delta\rho$) within $\pm 3^\circ$. (C) Lateral perspectives of selected snapshots with the respective angular pairs are shown to the right.

Table 7: Experimental Rotation and Tilt angle in the MD simulations

Dwell time		200 ns (%)	200-1000 ns (%)	Last 200 ns (%)
Topology	$\tau = 86^\circ \pm 3^\circ$	33	30	40
	$\tau = 86^\circ \pm 5^\circ$	47	49	62

All measures were done with the rotation angle $\Delta\rho = \pm 3^\circ$ (Reference values of Oce-LB2 $\rho = 25^\circ / \tau = 86^\circ$)

Along the MD simulation trajectory, the peptide interacts dynamically with the membrane, changing its relative position over time, consequently interacting with different groups of atoms as lipids, solvent molecules, and ions. Therefore, these dynamical contacts are expressed as averaged interaction of these atoms (or groups of atoms) as function of time and as function of the simulation box axis. For membrane systems it is useful to calculate the density of atom groups across a lipid bilayer, located at the xy plane in the simulation box, and typically with the z axis being the membrane normal.

The first step was calculating the average position of reference atoms in the bilayer. **Figure 44A** shows the two peak densities for the phosphorous atom (POPC phosphate group) along the Z axis (normal to membrane surface): at 2.64 nm and 6.29 nm, corresponding to the two lipid leaflets of the bilayer. Calculating the densities for the nitrogen atom of the choline head groups it is possible to correlate the relative positions to phosphate groups. **Figure 44B** shows peak densities for the oxygen atoms of the ester groups in the POPC structure, identified by O21/O22 and O31/O32. The ester group position was used as limit of the hydrophilic region of the POPC bilayer, or the starting coordinates for the membrane hydrophobic core. **Figure 44C** shows peak densities for selected atoms of Ocelatin-LB2, the amine nitrogens from the peptide bond of Ala-10, Leu-17 and Met-22. As the reference of all the maps is the simulation box, it is possible to correlate the relative positions of the peak densities. The coordinates for the average positions of the labelled Leu-17 and Ala-10 coincide with the coordinates of the oxygen atoms O31/O32 and O21/O22 (**Figure 44C**) of the POPC ester groups, which indicates that the internal axis of the helix is located in the interfacial region.

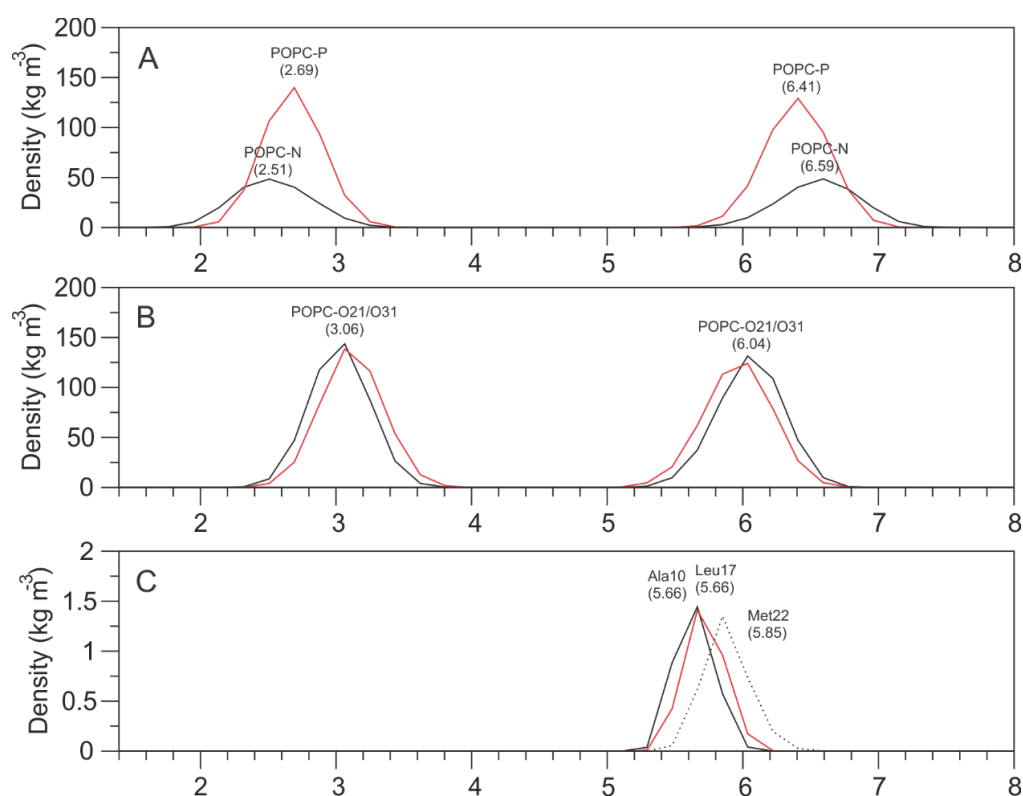


Figure 44: Density profiles of Ocellatin-LB2 reconstituted into the POPC bilayer averaged over the last 200 ns of MD simulation (800 to 1000 ns). (A) Density profiles of the phosphorous and nitrogen atoms (POPC-P; POPC-N) in each bilayer leaf. From the average position of the P atoms of each leaf it is possible to estimate the center of bilayer at 4.47 nm. (B) Density profiles of oxygen atoms, in the ester groups (O21/O22 and O31/O32) of POPC. (C) Density profile for the amidic nitrogen of Ala-10, Leu-17 and Met-22. Together, these density profiles suggest that Ocellatin-LB2 is in the transition region of the bilayer hydrophobic core, with Ala-10, Leu-17 and Met-22 density peaks in the region of POPC O31/O32 atoms. Hydrogen bond analysis indicate interactions of the lysine residues (Lys-7, Lys-11 and Lys-20) with the phosphate groups and the oxygen atoms of the ester groups (data not shown).

4.5. Discussion

The hydrophobic effect is supposedly the driving force of membrane binding^{101,120}, inasmuch as the thermodynamic parameters suggest an entropy-driven mechanisms for all ocellatins (**Table 6**). The observed relative affinity of interactions Oce-F1>Oce-LB1>Oce-LB2 is independent of the anionic³⁰ or zwitterionic phospholipid composition.

The highest apparent binding constant (K_{app}) and ΔG° of Oce-F1 in comparison to the other peptides, unequivocally confirm that the extra -Lys-Leu residues at C-terminus lead to stronger peptide-membrane interactions. By analyzing the membrane alignment of Oce-F1 (**Figure 29F and G**), these two most C-terminal residues lie on the interface, which corresponds to both stronger hydrophobic interactions including membrane insertion of Leu-24 sidechain as well as the electrostatic interactions between the charged Lys-24 and the phosphate groups and water molecules of the membrane interface. On the other hand, in spite of carrying an additional Asn at the C-terminus when compared to Oce-LB1, Oce-LB2 presents the smallest K_{app} and ΔG° absolute values, which are respectively about 10 and 2 times lower in comparison to those of Oce-F1.

Lastly, the entropic contributions observed for Ocellatin-F1 and -LB1 are about threefold higher than the determined for Oce-LB2. These data might be addressed as a greater insertion of Oce-F1 and -LB1 within the membrane, which leads to a higher release of water molecules from the hydration shell^{94,120,121}, when compared to the -LB2 analogue.

Extra quantitative information was given by SPR spectroscopy regarding the surface partition of the interactions between ocellatins and zwitterionic LUVs. The interactions of Oce-F1 clearly lead to significantly higher response levels. Besides, the calculated surface partition constants (K) demonstrate quite larger value for Oce-F1 when compared to the Oce-LB1 and Oce-LB2 (Fig. 4F), which is in line with ITC results.

The relative partition constants Oce-F1>Oce-LB1>Oce-LB2 correlate with the better-defined separation of hydrophilic and hydrophobic residues and the better-defined topology of Oce-F1 and -LB1 when compared to -LB2 (**Figure 29D-G**). Thus, the extra amphipathic helical turn by Leu-23 and Lys-24 help in a better anchoring of the Oce-F1 C-terminal portion into the

membrane (**Figure 29D-G**) and consequently a higher partition constant for this peptide (**Figure 41D**).

Interestingly, the sensogram of Oce-LB2 reveals a faster membrane dissociation in comparison to its analogues, since the RU signal decreases about two-three minutes before Oce-F1 and Oce-LB1 (**Figure 41A-C**). Considering the high degree of similarity among all three ocellatins, a two minutes delay in the peptide-membrane dissociation turns out to a significant difference. These thermodynamically and kinetically less favored membrane association of Oce-LB2 correlates with the hypothesis of a lower peptide insertion into the membrane¹²¹, topological variability and a lower entropic contribution (**Table 6**), related to the lower desolvation of membrane surface^{94,120,121}.

MD simulations of Oce-LB2 revealed that the helix azimuthal angle is virtually constant due to the anchoring role of both Lys-7 and Lys-20 residues (**Figure 43A**). Notwithstanding, wobbling motions of the helix main axis up and down result in slightly different degrees of membrane insertion. This process modulates the relative position of Asn-23 with respect to the bilayer surface.

By monitoring the helix tilting during the simulations within an interval of $\Delta\tau \pm 5$, the populational density between these two states become roughly fifty-fifty, indicating an interconversion between both states represented by topologies with τ near 86° and 94° (**Figure 43B**). Inquisitively, topology II ($4^\circ/91^\circ$) represents a quite similar alignment when compared to topology I (**Figure 29E**) and, besides, it lies within the range of tilt angles assessed by molecular dynamics. However, II would force the insertion of Lys-20 into the bilayer and MD simulations clearly restrain considerable rotations around the helix main axis, since it would represent a significant energy cost.

Chapter 5: Conclusions

All peptides and glycotriazole-peptides were obtained with high purity, ensuring adequate quality for the solid-state NMR experiments and other biophysical assays.

The membrane affinity, disruptive properties and antimicrobial activities of ocellatins can be discussed in regard to lysins anchoring role as a major parameter. Solid-state NMR spectroscopy indicated that both Lys-7 and -20 sidechains are stretched toward membrane interface to enable the anchoring of the amphipathic helices. For Oce-F1, however, the extra Lys-24 is also stretched toward the interface, which leads to a greater number of membrane anchoring points. Besides, the extra Leu-25 at Oce-F1 C-terminus also lies on the interface, which allows the insertion of its hydrophobic chain in the membrane interior.

The extra Asn-23 at Oce-LB2 C-terminus rotates the peptide helix 19° anticlockwise in comparison to -LB1, which leads to a topological variability in terms of the peptide's tilt angle. This topological change can be explained regarding the Whimley-White hydrophobicity scale in which is stated that the interfacial free energy of carboxyamide sidechains are unfavored by a factor of ~ 0.5 kcal/mol⁷⁷. Hence, Asn-23 becomes favorably distanced from the interfacial region and pulled into the hydrophilic face by a 4° slight inward deviation from planarity at N-terminus but, in turn, reduces both membrane binding and affinity constants as proved by ITC and SPR spectroscopy.

The topological analysis of peptide-membrane interactions, together with the examination of both structure and amino acids composition, enables to gain insight into where the antimicrobial potential gaps stems from, *i.e.*, $F1 \gg LB1 \geq LB2$ ^{26,30}. An important topic to be addressed in future investigations is the synthesis of Oce-F1 analogs with site-directed substitutions at position 23, inasmuch as Asn-23 seems to alter peptide dynamics, membrane affinity and topology, which reduces the antimicrobial potential of Oce-LB2.

Solid-state NMR measurements have revealed that the substitution of Thr-14 for a per-*O*-acetylated glycotriazole residue did not lead to significant topological differences. Nevertheless, a subtle rotation on its internal axis is observed and [pOAcGlc-Trz-A¹⁴]-PS-2 is deviated 11° clockwise about its internal axis when compared to the wild-type peptide. This

deviation pulls His-7 closer into the interface, unlike PS-2 where the pitch angle is only modulated by Ser-13. GtP-PS2 partition depends on both His-7 and Ser-13 residues. Besides, peptide tilt angle is also increased by -1° at C-terminus, leading the amphipathic design of the α -helix less inserted into the membrane. This depiction is related to ITC measurements³⁹ in anionic bilayers in which the entropic term is mitigated and the enthalpic one is increased. In light of these results, further studies are in the pipeline to study whether deacetylated glycotriazole residue enhances membrane affinity in regard to both PS-2 and [pOAcGlc-Trz-A¹⁴]-PS-2.

Opposite to [pOAcGlc-Trz-A¹⁴]-PS-2, disruptive membrane properties, affinity and antimicrobial activities are enhanced synergically by the glycotriazole residue in [pOAcGlc-Trz-A¹]-HSP1-NH₂. Due to the asymmetrical amphipathic design of the peptide, a tilted orientation at C-terminus within the membrane permits a greater interaction of nonpolar residues within hydrophobic core. Unlike [pOAcGlc-Trz-A¹⁴]-PS-2, for [pOAcGlc-Trz-A¹]-HSP1-NH₂ the glycotriazole residue is pulled into the interface which is highly likely that it works as an anchor point because of the aromatic triazole group. Thus, the enhancement of the glycotriazole-peptide properties³³, which has been assessed by SPR, dye leakage, dynamic light scattering, and zeta potential measurements³³ may stem from the anchor role of the glycotriazole. Besides, negatively charged Asp-4 close to the interface, and the intrinsic snorkeling effects of Lys-11 make that these residues work as anchoring points. In future investigations, it is of paramount interest to study the interaction topology of the wild-type HSP1 in order to compare more accurately the differences that arise from the insertion of the synthetic glycotriazole residue.

Finally, as far as we know, this work investigates in an unprecedented way the interaction topologies of glycotriazole-peptides within phospholipid bilayers at atomic scale by mechanically oriented solid-state NMR spectroscopy. The localization of the per-*O*-acetylated-glycotriazole residue, either on the hydrophilic part of the bilayer or on the membrane interface, suggests the eleven hydrogen bond acceptor atoms that constitute the glycotriazole moiety play important roles for the GtP-membrane interaction.

Bibliography

- (1) Zhang, L.; Gallo, R. L. Antimicrobial Peptides. *CURBIO* **2016**, *26* (1), R14–R19. <https://doi.org/10.1016/j.cub.2015.11.017>.
- (2) Fleming, A. On a Remarkable Bacteriolytic Element Found in Tissues and Secretions. *Proc. R. Soc. B Biol. Sci.* **1922**, *93* (653), 306–317. <https://doi.org/10.1098/rspb.1922.0023>.
- (3) Hancock, R. E. W.; Chapple, D. S. Peptide Antibiotics. *Antimicrob. Agents Chemother.* **1999**, *43* (6), 1317–1323. <https://doi.org/10.1128/aac.43.6.1317>.
- (4) Harris, F.; Dennison, S.; Phoenix, D. Anionic Antimicrobial Peptides from Eukaryotic Organisms. *Curr. Protein Pept. Sci.* **2009**, *10* (6), 585–606. <https://doi.org/10.2174/138920309789630589>.
- (5) Hancock, R. E. W.; Falla, T.; Brown, M., Cationic Bactericidal Peptides. In: *Advances in Microbial Physiology*, Ed.; Academic Press, 1995; Vol. 37, pp 135–175. [https://doi.org/https://doi.org/10.1016/S0065-2911\(08\)60145-9](https://doi.org/https://doi.org/10.1016/S0065-2911(08)60145-9).
- (6) Epand, R. M.; Vogel, H. J. Diversity of Antimicrobial Peptides and Their Mechanisms of Action. *Biochim. Biophys. Acta - Biomembr.* **1999**, *1462* (1), 11–28. [https://doi.org/https://doi.org/10.1016/S0005-2736\(99\)00198-4](https://doi.org/https://doi.org/10.1016/S0005-2736(99)00198-4).
- (7) Steiner, H.; Hultmark, D.; Engström, Å.; Bennich, H.; Boman, H. G. Sequence and Specificity of Two Antibacterial Proteins Involved in Insect Immunity. *Nature* **1981**, *292* (5820), 246–248. <https://doi.org/10.1038/292246a0>.
- (8) Bechinger, B.; Zasloff, M.; Opella, S. J. Structure and Dynamics of the Antibiotic Peptide PGLa in Membranes by Solution and Solid-State Nuclear Magnetic Resonance Spectroscopy. *Biophys. J.* **1998**, *74* (2 I), 981–987. [https://doi.org/10.1016/S0006-3495\(98\)74021-4](https://doi.org/10.1016/S0006-3495(98)74021-4).
- (9) Timothy J. Falla, D. Nedra Karunaratne, R. E. W. H. Mode of Action of the Antimicrobial Peptide Indolicidin. **1996**, *271* (32), 19298–19303.
- (10) Hancock, R. E. W. Peptide Antibiotics. *Lancet* **1997**, *349* (9049), 418–422. [https://doi.org/https://doi.org/10.1016/S0140-6736\(97\)80051-7](https://doi.org/https://doi.org/10.1016/S0140-6736(97)80051-7).
- (11) Bradshaw, J. P. Cationic Antimicrobial Peptides: Issues for Potential Clinical Use. *BioDrugs* **2003**, *17* (4), 233–240. <https://doi.org/10.2165/00063030-200317040-00002>.
- (12) Matsuzaki, K. Why and How Are Peptide-Lipid Interactions Utilized for Self-Defense? Magainins and Tachyplesins as Archetypes. *Biochim. Biophys. Acta - Biomembr.* **1999**, *1462* (1–2), 1–10. [https://doi.org/10.1016/S0005-2736\(99\)00197-2](https://doi.org/10.1016/S0005-2736(99)00197-2).
- (13) Matsuzaki, K.; Sugishita, K.; Fujii, N.; Miyajima, K. Molecular Basis for Membrane Selectivity of an Antimicrobial Peptide, Magainin 2. *Biochemistry* **1995**, *34* (10), 3423–3429. <https://doi.org/10.1021/bi00010a034>.
- (14) Zasloff, M. Antimicrobial peptides of multicellular organisms. *Nature* **2002**, 389–395. <https://doi.org/10.1038/415389>
- (15) Westerhoff, H. V.; Juretic, D.; Hendler, R. W.; Zasloff, M. Magainins and the Disruption of Membrane-Linked Free-Energy Transduction. *Proc. Natl. Acad. Sci. U. S. A.* **1989**, *86* (17), 6597–6601. <https://doi.org/10.1073/pnas.86.17.6597>.

- (16) Yang, L.; Weiss, T. M.; Lehrer, R. I.; Huang, H. W. Crystallization of Antimicrobial Pores in Membranes: Magainin and Protegrin. *Biophys. J.* **2000**, *79* (4), 2002–2009. [https://doi.org/10.1016/S0006-3495\(00\)76448-4](https://doi.org/10.1016/S0006-3495(00)76448-4).
- (17) Bierbaum, G., Sahl, H. Induction of autolysis of staphylococci by the basic peptide antibiotics Pep 5 and nisin and their influence on the activity of autolytic enzymes. *Arch. Microbiol.* **141**, 249–254 (1985) <https://doi.org/10.1007/BF00408067>
- (18) Silva, P. M.; Gonçalves, S.; Santos, N. C. Defensins: Antifungal Lessons from Eukaryotes. *Front. Microbiol.* **2014**, *5* (MAR), 1–17. <https://doi.org/10.3389/fmicb.2014.00097>.
- (19) Lin Yang, Thad A. Harroun, Thomas M. Weiss, Lai Ding, and H. W. H. Barrel-Stave Model or Toroidal Model? A Case Study on Melittin Pores. *Biophys. J.* **2001**, *81*, 1475–1485.
- (20) Sengupta, D.; Leontiadou, H.; Mark, A. E.; Marrink, S.-J. Toroidal Pores Formed by Antimicrobial Peptides Show Significant Disorder. *Biochim. Biophys. Acta - Biomembr.* **2008**, *1778* (10), 2308–2317. <https://doi.org/https://doi.org/10.1016/j.bbamem.2008.06.007>.
- (21) Bechinger, B.; Lohner, K. Detergent-like Actions of Linear Amphipathic Cationic Antimicrobial Peptides. *Biochim. Biophys. Acta - Biomembr.* **2006**, *1758* (9), 1529–1539. <https://doi.org/https://doi.org/10.1016/j.bbamem.2006.07.001>.
- (22) Carnicelli, V.; Lizzi, a R.; Ponzi, a; Amicosante, G.; Bozzi, a; Giulio, a Di. Interaction between Antimicrobial Peptides (AMPs) and Their Primary Target , the Biomembranes . *Microb. Pathog. Strateg. Combat. them Sci. Technol. Educ.* **2013**, 1123–1134.
- (23) Li, Y.; Xiang, Q.; Zhang, Q.; Huang, Y.; Su, Z. Overview on the Recent Study of Antimicrobial Peptides: Origins, Functions, Relative Mechanisms and Application. *Peptides* **2012**, *37* (2), 207–215. <https://doi.org/https://doi.org/10.1016/j.peptides.2012.07.001>.
- (24) Kosikowska, P.; Lesner, A. Antimicrobial Peptides (AMPs) as Drug Candidates: A Patent Review (2003–2015). *Expert Opin. Ther. Pat.* **2016**, *26* (6), 689–702. <https://doi.org/10.1080/13543776.2016.1176149>.
- (25) Purruicker, O.; Hillebrandt, H.; Adlkofer, K.; Tanaka, M. Deposition of Highly Resistive Lipid Bilayer on Silicon–Silicon Dioxide Electrode and Incorporation of Gramicidin Studied by Ac Impedance Spectroscopy. *Electrochim. Acta* **2001**, *47*, 791–798. [https://doi.org/10.1016/S0013-4686\(01\)00759-9](https://doi.org/10.1016/S0013-4686(01)00759-9).
- (26) Gusmão, K. A. G.; dos Santos, D. M.; Santos, V. M.; Cortés, M. E.; Reis, P. V. M.; Santos, V. L.; Piló-Veloso, D.; Verly, R. M.; de Lima, M. E.; Resende, J. M. Ocellatin Peptides from the Skin Secretion of the South American Frog *Leptodactylus Labyrinthicus* (Leptodactylidae): Characterization, Antimicrobial Activities and Membrane Interactions. *J. Venom. Anim. Toxins Incl. Trop. Dis.* **2017**, *23* (1), 1–14. <https://doi.org/10.1186/s40409-017-0094-y>.
- (27) Marani, M. M.; Dourado, F. S.; Quelemes, P. V.; de Araujo, A. R.; Perfeito, M. L. G.; Barbosa, E. A.; Vêras, L. M. C.; Coelho, A. L. R.; Andrade, E. B.; Eaton, P.; et al. Characterization and Biological Activities of Ocellatin Peptides from the Skin Secretion of the Frog *Leptodactylus Pustulatus*. *J. Nat. Prod.* **2015**, *78* (7), 1495–1504. <https://doi.org/10.1021/np500907t>.

- (28) Cunha Neto, R. dos S.; Vigerelli, H.; Jared, C.; Antoniazzi, M. M.; Chaves, L. B.; da Silva, A. de C. R.; Melo, R. L. de; Sciani, J. M.; Pimenta, D. C. Synergic Effects between Ocellatin-F1 and Bufotenine on the Inhibition of BHK-21 Cellular Infection by the Rabies Virus. *J. Venom. Anim. Toxins Incl. Trop. Dis.* **2015**, *21* (1), 50. <https://doi.org/10.1186/s40409-015-0048-1>.
- (29) Libério, M. S.; Joanitti, G. A.; Azevedo, R. B.; Cilli, E. M.; Zanotta, L. C.; Nascimento, A. C.; Sousa, M. V.; Pires Júnior, O. R.; Fontes, W.; Castro, M. S. Anti-Proliferative and Cytotoxic Activity of Pentadactylin Isolated from *Leptodactylus Labyrinthicus* on Melanoma Cells. *Amino Acids* **2011**, *40* (1), 51–59. <https://doi.org/10.1007/s00726-009-0384-y>.
- (30) Gomes, K. A. G. G.; dos Santos, D. M.; Santos, V. M.; Piló-Veloso, D.; Mundim, H. M.; Rodrigues, L. V.; Lião, L. M.; Verly, R. M.; de Lima, M. E.; Resende, J. M. NMR Structures in Different Membrane Environments of Three Ocellatin Peptides Isolated from *Leptodactylus Labyrinthicus*. *Peptides* **2018**, *103* (December 2017), 72–83. <https://doi.org/10.1016/j.peptides.2018.03.016>.
- (31) Michalek, M.; Salnikov, E. S.; Bechinger, B. Structure and Topology of the Huntingtin 1–17 Membrane Anchor by a Combined Solution and Solid-State NMR Approach. *Biophys. J.* **2013**, *105* (3), 699–710. <https://doi.org/https://doi.org/10.1016/j.bpj.2013.06.030>.
- (32) Prates, M. V.; Sforça, M. L.; Regis, W. C. B.; Leite, J. R. S. A.; Silva, L. P.; Pertinhez, T. A.; Araújo, A. L. T.; Azevedo, R. B.; Spisni, A.; Bloch, C. The NMR-Derived Solution Structure of a New Cationic Antimicrobial Peptide from the Skin Secretion of the Anuran *Hyla Punctata*. *J. Biol. Chem.* **2004**, *279* (13), 13018–13026. <https://doi.org/10.1074/jbc.M310838200>.
- (33) Junior, E. F. C.; Guimarães, C. F. R. C.; Franco, L. L.; Alves, R. J.; Kato, K. C.; Martins, H. R.; de Souza Filho, J. D.; Bemquerer, M. P.; Munhoz, V. H. O.; Resende, J. M.; et al. Glycotriazole-Peptides Derived from the Peptide HSP1: Synergistic Effect of Triazole and Saccharide Rings on the Antifungal Activity. *Amino Acids* **2017**, *49* (8), 1389–1400. <https://doi.org/10.1007/s00726-017-2441-2>.
- (34) Sforça, M. L.; Oyama Sérgio; Canduri, F.; Lorenzi, C. C. B.; Pertinhez, T. A.; Konno, K.; Souza, B. M.; Palma, M. S.; Ruggiero Neto, J.; Azevedo Walter F.; et al. How C-Terminal Carboxyamidation Alters the Biological Activity of Peptides from the Venom of the Eumenine Solitary Wasp. *Biochemistry* **2004**, *43* (19), 5608–5617. <https://doi.org/10.1021/bi0360915>.
- (35) Ali, M. F.; Soto, A.; Knoop, F. C.; Conlon, J. M. Antimicrobial Peptides Isolated from Skin Secretions of the Diploid Frog, *Xenopus Tropicalis* (Pipidae). *Biochim. Biophys. Acta - Protein Struct. Mol. Enzymol.* **2001**, *1550* (1), 81–89. [https://doi.org/https://doi.org/10.1016/S0167-4838\(01\)00272-2](https://doi.org/https://doi.org/10.1016/S0167-4838(01)00272-2).
- (36) Katayama, H.; Ohira, T.; Aida, K.; Nagasawa, H. Significance of a Carboxyl-Terminal Amide Moiety in the Folding and Biological Activity of Crustacean Hyperglycemic Hormone. *Peptides* **2002**, *23* (9), 1537–1546. [https://doi.org/https://doi.org/10.1016/S0196-9781\(02\)00094-3](https://doi.org/https://doi.org/10.1016/S0196-9781(02)00094-3).
- (37) Leite, J. R. S. A.; Silva, L. P.; Rodrigues, M. I. S.; Prates, M. V.; Brand, G. D.; Lacava, B. M.; Azevedo, R. B.; Bocca, A. L.; Albuquerque, S.; Bloch, C. Phylloseptins: A Novel Class of Anti-Bacterial and Anti-Protozoan Peptides from the Phyllomedusa Genus. *Peptides* **2005**, *26* (4), 565–573. <https://doi.org/10.1016/j.peptides.2004.11.002>.

- (38) Resende, J. M.; Moraes, C. M.; Prates, M. V.; Cesar, A.; Almeida, F. C. L.; Mundim, N. C. C. R.; Valente, A. P.; Bemquerer, M. P.; Piló-Veloso, D.; Bechinger, B. Solution NMR Structures of the Antimicrobial Peptides Phylloseptin-1, -2, and -3 and Biological Activity: The Role of Charges and Hydrogen Bonding Interactions in Stabilizing Helix Conformations. *Peptides* **2008**, *29* (10), 1633–1644. <https://doi.org/10.1016/j.peptides.2008.06.022>.
- (39) Guimarães, C. F. R. C. Síntese de Peptídeos : Cinética de Dimerização via Formação de Ligação de Dissulfeto , Obtenção e Estudos Biofísicos de Glicotriazol-Peptídeos CARLOS FILIPE REIS COSTA GUIMARÃES Síntese de Peptídeos : Cinética de Dimerização via Formação de Ligação de Dis. *PhD Thesis - UFMG* **2017**.
- (40) WUST, M. A. Estudos Estruturais Por RMN Do Glicopiranosil-Triazol-Peptídeo [POAcGlc-Trz-A14]PS-2 Em Meios Miméticos de Membrana. *Master's thesis - UFMG* **2017**.
- (41) Kimmerlin, T.; Seebach, D. “100 Years of Peptide Synthesis”: Ligation Methods for Peptide and Protein Synthesis with Applications to β -Peptide Assemblies. *J. Pept. Res.* **2005**, *65* (2), 229–260. <https://doi.org/10.1111/j.1399-3011.2005.00214.x>.
- (42) W.C. Chan; White, P.D., *Fmoc Solid Phase Peptide Synthesis: A practical approach*. New York: Oxford University Press, **2000**.
- (43) Liang, L.; Astruc, D. The Copper(I)-Catalyzed Alkyne-Azide Cycloaddition (CuAAC) “Click” Reaction and Its Applications. An Overview. *Coord. Chem. Rev.* **2011**, *255* (23–24), 2933–2945. <https://doi.org/10.1016/j.ccr.2011.06.028>.
- (44) Tornøe, C. W.; Christensen, C.; Meldal, M. Peptidotriazoles on Solid Phase: [1,2,3]-Triazoles by Regiospecific Copper(I)-Catalyzed 1,3-Dipolar Cycloadditions of Terminal Alkynes to Azides. *J. Org. Chem.* **2002**, *67* (9), 3057–3064. <https://doi.org/10.1021/jo011148j>.
- (45) Rostovtsev, V. V.; Green, L. G.; Fokin, V. V.; Sharpless, K. B. A Stepwise Huisgen Cycloaddition Process: Copper(I)-Catalyzed Regioselective “Ligation” of Azides and Terminal Alkynes. *Angew. Chemie Int. Ed.* **2002**, *41* (14), 2596–2599. [https://doi.org/10.1002/1521-3773\(20020715\)41:14<2596::AID-ANIE2596>3.0.CO;2-4](https://doi.org/10.1002/1521-3773(20020715)41:14<2596::AID-ANIE2596>3.0.CO;2-4).
- (46) Rodionov, V. O.; Presolski, S. I.; Díaz Díaz, D.; Fokin, V. V.; Finn, M. G. Ligand-Accelerated Cu-Catalyzed Azide–Alkyne Cycloaddition: A Mechanistic Report. *J. Am. Chem. Soc.* **2007**, *129* (42), 12705–12712. <https://doi.org/10.1021/ja072679d>.
- (47) Himo, F.; Lovell, T.; Hilgraf, R.; Rostovtsev, V. V.; Noodleman, L.; Sharpless, K. B.; Fokin, V. V. Copper(I)-Catalyzed Synthesis of Azoles. DFT Study Predicts Unprecedented Reactivity and Intermediates. *J. Am. Chem. Soc.* **2005**, *127* (1), 210–216. <https://doi.org/10.1021/ja0471525>.
- (48) Worrell, B. T.; Malik, J. A.; Fokin, V. V. Direct Evidence of a Dinuclear Copper Intermediate in Cu(I)-Catalyzed Azide-Alkyne Cycloadditions. *Science (80-.)*. **2013**, *340* (6131), 457 LP – 460. <https://doi.org/10.1126/science.1229506>.
- (49) Troll, W., and Cannan, R. K. A Modified Photometric Ninhydrin Method for the Analysis of Amino and Imino Acids. *J. Biol. Chem.* **1953**, *200*, 803–811.
- (50) Yang, Y. *Side Reactions in Peptide Synthesis*. Copenhagen: Oxford Academic Press, **2016**. <https://doi.org/10.1016/b978-0-12-801009-9.00014-8>.

- (51) Aisenbrey, C.; Bertani, P.; Bechinger, B. Solid-State NMR Investigations of Membrane-Associated Antimicrobial Peptides. *Antimicrob. Pept. Methods Mol. Biol.* **2016**, *618*, 209–233. <https://doi.org/10.1007/978-1-60761-594-1>.
- (52) Bechinger, B.; Sizun, C. Alignment and Structural Analysis of Membrane Polypeptides By ^{15}N And ^{31}P Solid-State NMR Spectroscopy. *Concepts Magn. Reson. Part A Bridg. Educ. Res.* **2003**, *18* (2), 130–145. <https://doi.org/10.1002/cmr.a.10070>.
- (53) Resende, J. M.; Verly, R. M.; Aisenbrey, C.; Cesar, A.; Bertani, P.; Piló-Veloso, D.; Bechinger, B. Membrane Interactions of Phylloseptin-1, -2, and -3 Peptides by Oriented Solid-State NMR Spectroscopy. *Biophys. J.* **2014**, *107* (4), 901–911. <https://doi.org/10.1016/j.bpj.2014.07.014>.
- (54) Levitt, M. H. *Spin Dynamics*; John Wiley & Sons, Ltd: Chichester, 2008.
- (55) Salnikov, E.; Bertani, P.; Raap, J.; Bechinger, B. Analysis of the Amide ^{15}N Chemical Shift Tensor of the Catetrasubstituted Constituent of Membrane-Active Peptaibols, the α -Aminoisobutyric Acid Residue, Compared to Those of Di- and Tri-Substituted Proteinogenic Amino Acid Residues. *J. Biomol. NMR* **2009**, *45* (4), 373–387. <https://doi.org/10.1007/s10858-009-9380-5>.
- (56) Bechinger, B.; Salnikov, E. S. The Membrane Interactions of Antimicrobial Peptides Revealed by Solid-State NMR Spectroscopy. *Chem. Phys. Lipids* **2012**, *165* (3), 282–301. <https://doi.org/10.1016/j.chemphyslip.2012.01.009>.
- (57) Seelig, J. Deuterium Magnetic Resonance: Theory and Application to Lipid Membranes. *Q. Rev. Biophys.* **1977**, *10* (3), 353–418. <https://doi.org/10.1017/S0033583500002948>.
- (58) Aisenbrey, C.; Bechinger, B. Investigations of Polypeptide Rotational Diffusion in Aligned Membranes by ^2H and ^{15}N Solid-State NMR Spectroscopy. *J. Am. Chem. Soc.* **2004**, *126* (50), 16676–16683. <https://doi.org/10.1021/ja0468675>.
- (59) Rance, M.; Byrd, R. A. Obtaining High-Fidelity Spin-12 Powder Spectra in Anisotropic Media: Phase-Cycled Hahn Echo Spectroscopy. *J. Magn. Reson.* **1983**, *52* (2), 221–240. [https://doi.org/https://doi.org/10.1016/0022-2364\(83\)90190-7](https://doi.org/https://doi.org/10.1016/0022-2364(83)90190-7).
- (60) Hediger, S.; Meier, B. H.; Ernst, R. R. Adiabatic Passage Hartmann-Hahn Cross Polarization in NMR under Magic Angle Sample Spinning. *Chem. Phys. Lett.* **1995**, *240* (5), 449–456. [https://doi.org/https://doi.org/10.1016/0009-2614\(95\)00505-X](https://doi.org/https://doi.org/10.1016/0009-2614(95)00505-X).
- (61) Davis, J. H.; Jeffrey, K. R.; Bloom, M.; Valic, M. I.; Higgs, T. P. Quadrupolar Echo Deuteron Magnetic Resonance Spectroscopy in Ordered Hydrocarbon Chains. *Chem. Phys. Lett.* **1976**, *42* (2), 390–394. [https://doi.org/https://doi.org/10.1016/0009-2614\(76\)80392-2](https://doi.org/https://doi.org/10.1016/0009-2614(76)80392-2).
- (62) Jaeger, C.; Hemmann, F. EASY: A Simple Tool for Simultaneously Removing Background, Deadtime and Acoustic Ringing in Quantitative NMR Spectroscopy - Part I: Basic Principle and Applications. *Solid State Nucl. Magn. Reson.* **2014**, *57–58*, 22–28. <https://doi.org/10.1016/j.ssnmr.2013.11.002>.
- (63) Silva Marinho, L. E. Estudos Biofísicos Do Mecanismo de Ação de Glicotriazol-Péptídeos, UFVJM, 2018.
- (64) Aisenbrey, C.; Salnikov, E. S.; Raya, J.; Michalek, M.; Bechinger, B. *Solid-State NMR Approaches to Study Protein Structure and Protein–Lipid Interactions*; Kleinschmidt, J. H., Ed.; Springer, 2019; Vol. 2003. https://doi.org/https://doi.org/10.1007/978-1-4939-9512-7_23, ©.

- (65) Resende, J. M.; Moraes, C. M.; Munhoz, V. H. O.; Aisenbrey, C.; Verly, R. M.; Bertani, P.; Cesar, A.; Piló-Veloso, D.; Bechinger, B. Membrane Structure and Conformational Changes of the Antibiotic Heterodimeric Peptide Distictin by Solid-State NMR Spectroscopy. *Proc. Natl. Acad. Sci. U. S. A.* **2009**, *106* (39), 16639–16644. <https://doi.org/10.1073/pnas.0905069106>.
- (66) Aisenbrey, C.; Bechinger, B. Tilt and Rotational Pitch Angle of Membrane-Inserted Polypeptides from Combined ¹⁵N and ²H Solid-State NMR Spectroscopy. *Biochemistry* **2004**, *43* (32), 10502–10512. <https://doi.org/10.1021/bi049409h>.
- (67) Aisenbrey, C.; Sizun, C.; Koch, J.; Herget, M.; Abele, R.; Bechinger, B.; Tampé, R. Structure and Dynamics of Membrane-Associated ICP47, a Viral Inhibitor of the MHC I Antigen-Processing Machinery. *J. Biol. Chem.* **2006**, *281* (41), 30365–30372. <https://doi.org/10.1074/jbc.M603000200>.
- (68) Granseth, E.; Von Heijne, G.; Elofsson, A. A Study of the Membrane-Water Interface Region of Membrane Proteins. *J. Mol. Biol.* **2005**, *346* (1), 377–385. <https://doi.org/10.1016/j.jmb.2004.11.036>.
- (69) Strandberg, E.; Killian, J. A. Snorkeling of Lysine Side Chains in Transmembrane Helices: How Easy Can It Get? *FEBS Lett.* **2003**, *544* (1–3), 69–73. [https://doi.org/10.1016/S0014-5793\(03\)00475-7](https://doi.org/10.1016/S0014-5793(03)00475-7).
- (70) De Planque, M. R. R.; Killian, J. A. Protein-Lipid Interactions Studied with Designed Transmembrane Peptides: Role of Hydrophobic Matching and Interfacial Anchoring (Review). *Mol. Membr. Biol.* **2003**, *20* (4), 271–284. <https://doi.org/10.1080/09687680310001605352>.
- (71) Killian, J. A.; Von Heijne, G. How Proteins Adapt to a Membrane-Water Interface. *Trends Biochem. Sci.* **2000**, *25* (9), 429–434. [https://doi.org/10.1016/S0968-0004\(00\)01626-1](https://doi.org/10.1016/S0968-0004(00)01626-1).
- (72) Illergård, K.; Kauko, A.; Elofsson, A. Why Are Polar Residues within the Membrane Core Evolutionary Conserved? *Proteins Struct. Funct. Bioinforma.* **2011**, *79* (1), 79–91. <https://doi.org/10.1002/prot.22859>.
- (73) De Planque, M. R. R.; Kruijtzter, J. A. W.; Liskamp, R. M. J.; Marsh, D.; Greathouse, D. V.; Koeppe, R. E.; De Kruijff, B.; Killian, J. A. Different Membrane Anchoring Positions of Tryptophan and Lysine in Synthetic Transmembrane α -Helical Peptides. *J. Biol. Chem.* **1999**, *274* (30), 20839–20846. <https://doi.org/10.1074/jbc.274.30.20839>.
- (74) Harzer, U.; Bechinger, B. Alignment of Lysine-Anchored Membrane Peptides under Conditions of Hydrophobic Mismatch: A CD, ¹⁵N and ³¹P Solid-State NMR Spectroscopy Investigation. *Biochemistry* **2000**, *39* (43), 13106–13114. <https://doi.org/10.1021/bi000770n>.
- (75) Kougentakis, C. M.; Grasso, E. M.; Robinson, A. C.; Caro, J. A.; Schlessman, J. L.; Majumdar, A.; García-Moreno E., B. Anomalous Properties of Lys Residues Buried in the Hydrophobic Interior of a Protein Revealed with ¹⁵N-Detect NMR Spectroscopy. *J. Phys. Chem. Lett.* **2018**, *9* (2), 383–387. <https://doi.org/10.1021/acs.jpcclett.7b02668>.
- (76) Sengupta, D.; Smith, J. C.; Ullmann, G. M. Partitioning of Amino-Acid Analogues in a Five-Slab Membrane Model. *Biochim. Biophys. Acta - Biomembr.* **2008**, *1778* (10), 2234–2243. <https://doi.org/10.1016/j.bbamem.2008.06.014>.
- (77) White, S. H.; Wimley, W. C. Hydrophobic Interactions of Peptides with Membrane Interfaces. *Biochim. Biophys. Acta - Rev. Biomembr.* **1998**, *1376* (3), 339–352. [https://doi.org/10.1016/S0304-4157\(98\)00021-5](https://doi.org/10.1016/S0304-4157(98)00021-5).

- (78) Malmsten, M. 4 - Protein and Peptide Interactions with Phospholipid Membranes and Surfaces; Griesser, H. J. B. T.-T. F. C. for B. and B. A., Ed.; Woodhead Publishing, Cambridge, MA. 2016; pp 61–77. <https://doi.org/https://doi.org/10.1016/B978-1-78242-453-6.00004-3>.
- (79) Parks, L. W.; Casey, W. M. PHYSIOLOGICAL IMPLICATIONS OF STEROL BIOSYNTHESIS IN YEAST. *Annu. Rev. Microbiol.* **1995**, *49* (1), 95–116. <https://doi.org/10.1146/annurev.mi.49.100195.000523>.
- (80) Perrin, B. S.; Tian, Y.; Fu, R.; Grant, C. V.; Chekmenev, E. Y.; Wieczorek, W. E.; Dao, A. E.; Hayden, R. M.; Burzynski, C. M.; Venable, R. M.; et al. High-Resolution Structures and Orientations of Antimicrobial Peptides Piscidin 1 and Piscidin 3 in Fluid Bilayers Reveal Tilting, Kinking, and Bilayer Immersion. *J. Am. Chem. Soc.* **2014**, *136* (9), 3491–3504. <https://doi.org/10.1021/ja411119m>.
- (81) Liu, A.; Wenzel, N.; Qi, X. Role of Lysine Residues in Membrane Anchoring of Saposin C. *Arch. Biochem. Biophys.* **2005**, *443* (1–2), 101–112. <https://doi.org/10.1016/j.abb.2005.09.007>.
- (82) Vostrikov, V. V.; Daily, A. E.; Greathouse, D. V.; Koeppe, R. E. Charged or Aromatic Anchor Residue Dependence of Transmembrane Peptide Tilt. *J. Biol. Chem.* **2010**, *285* (41), 31723–31730. <https://doi.org/10.1074/jbc.M110.152470>.
- (83) Holt, A.; Killian, J. A. Orientation and Dynamics of Transmembrane Peptides: The Power of Simple Models. *Eur. Biophys. J.* **2010**, *39* (4), 609–621. <https://doi.org/10.1007/s00249-009-0567-1>.
- (84) Shahmiri, M.; Cornell, B.; Mechler, A. Phenylalanine Residues Act as Membrane Anchors in the Antimicrobial Action of Aurein 1.2. *Biointerphases* **2017**, *12* (5), 05G605. <https://doi.org/10.1116/1.4995674>.
- (85) Seelig, J. Thermodynamics of Lipid–Peptide Interactions. *Biochim. Biophys. Acta - Biomembr.* **2004**, *1666* (1), 40–50. <https://doi.org/https://doi.org/10.1016/j.bbamem.2004.08.004>.
- (86) Seelig, J. Titration Calorimetry of Lipid–Peptide Interactions. *Biochim. Biophys. Acta - Rev. Biomembr.* **1997**, *1331* (1), 103–116. [https://doi.org/https://doi.org/10.1016/S0304-4157\(97\)00002-6](https://doi.org/https://doi.org/10.1016/S0304-4157(97)00002-6).
- (87) Broecker, J.; Vargas, C.; Keller, S. Revisiting the Optimal Cvalue for Isothermal Titration Calorimetry. *Anal. Biochem.* **2011**, *418* (2), 307–309. <https://doi.org/https://doi.org/10.1016/j.ab.2011.07.027>.
- (88) Heerklotz, H. The Microcalorimetry of Lipid Membranes. *J. Phys. Condens. Matter* **2004**, *16* (15), R441–R467. <https://doi.org/10.1088/0953-8984/16/15/r01>.
- (89) Heerklotz, H.; Seelig, J. Titration Calorimetry of Surfactant–Membrane Partitioning and Membrane Solubilization. *Biochim. Biophys. Acta - Biomembr.* **2000**, *1508* (1), 69–85. [https://doi.org/https://doi.org/10.1016/S0304-4157\(00\)00009-5](https://doi.org/https://doi.org/10.1016/S0304-4157(00)00009-5).
- (90) Andreev, O. A.; Dupuy, A. D.; Segala, M.; Sandugu, S.; Serra, D. A.; Chichester, C. O.; Engelman, D. M.; Reshetnyak, Y. K. Mechanism and Uses of a Membrane Peptide That Targets Tumors and Other Acidic Tissues &in Vivo&; *Proc. Natl. Acad. Sci.* **2007**, *104* (19), 7893 LP – 7898. <https://doi.org/10.1073/pnas.0702439104>.

- (91) Deleu, M.; Crowet, J.-M.; Nasir, M. N.; Lins, L. Complementary Biophysical Tools to Investigate Lipid Specificity in the Interaction between Bioactive Molecules and the Plasma Membrane: A Review. *Biochim. Biophys. Acta - Biomembr.* **2014**, *1838* (12), 3171–3190. <https://doi.org/https://doi.org/10.1016/j.bbamem.2014.08.023>.
- (92) Verly, R. M.; Rodrigues, M. A.; Daghanli, K. R. P.; Denadai, A. M. L.; Cuccovia, I. M.; Bloch, C.; Frézard, F.; Santoro, M. M.; Piló-Veloso, D.; Bemquerer, M. P. Effect of Cholesterol on the Interaction of the Amphibian Antimicrobial Peptide DD K with Liposomes. *Peptides* **2008**, *29* (1), 15–24. <https://doi.org/https://doi.org/10.1016/j.peptides.2007.10.028>.
- (93) Srivastava, V. K.; Yadav, R. Chapter 9 - Isothermal Titration Calorimetry; Misra, G. B. T.-D. P. H. for C. B. D. S., Ed.; Academic Press, London, 2019; pp 125–137. <https://doi.org/https://doi.org/10.1016/B978-0-12-816548-5.00009-5>.
- (94) Frasca, V. Biophysical Characterization of Antibodies with Isothermal Titration Calorimetry. *J. Appl. Bioanal.* **2016**, *2* (3), 90–102. <https://doi.org/10.17145/jab.16.013>.
- (95) Mozsolits, H.; Wirth, H. J.; Werkmeister, J.; Aguilar, M. I. Analysis of Antimicrobial Peptide Interactions with Hybrid Bilayer Membrane Systems Using Surface Plasmon Resonance. *Biochim. Biophys. Acta - Biomembr.* **2001**, *1512* (1), 64–76. [https://doi.org/10.1016/S0005-2736\(01\)00303-0](https://doi.org/10.1016/S0005-2736(01)00303-0).
- (96) Patching, S. G. Surface Plasmon Resonance Spectroscopy for Characterisation of Membrane Protein-Ligand Interactions and Its Potential for Drug Discovery. *Biochim. Biophys. Acta - Biomembr.* **2014**, *1838* (1 PARTA), 43–55. <https://doi.org/10.1016/j.bbamem.2013.04.028>.
- (97) Kamimori, H.; Hall, K.; Craik, D. J.; Aguilar, M.-I. Studies on the Membrane Interactions of the Cyclotides Kalata B1 and Kalata B6 on Model Membrane Systems by Surface Plasmon Resonance. *Anal. Biochem.* **2005**, *337* (1), 149–153. <https://doi.org/https://doi.org/10.1016/j.ab.2004.10.028>.
- (98) Copps J., Murphy R.F., Lovas S. (2008) Molecular Dynamics Simulations of Peptides. In: Otvos L. (eds) Peptide-Based Drug Design. Methods In Molecular Biology™, vol 494. Humana Press <https://doi.org/10.1007/978-1-59745-419-3>.
- (99) Schneider R., Sharma A.R., Rai A. (2008) Introduction to Molecular Dynamics. In: Fehske H., Schneider R., Weiße A. (eds) Computational Many-Particle Physics. Lecture Notes in Physics, vol 739. Springer, Berlin, Heidelberg <https://doi.org/10.1007/978-3-540-74686-7>.
- (100) Weiner, P. K.; Kollman, P. A. AMBER: Assisted Model Building with Energy Refinement. A General Program for Modeling Molecules and Their Interactions. *J. Comput. Chem.* **1981**, *2* (3), 287–303. <https://doi.org/10.1002/jcc.540020311>.
- (101) Wieprecht, T.; Seelig, J. B. T.-C. T. in M. Isothermal Titration Calorimetry for Studying Interactions between Peptides and Lipid Membranes. In *Peptide-Lipid Interactions*; Academic Press, USA, 2002; Vol. 52, pp 31–56. [https://doi.org/https://doi.org/10.1016/S1063-5823\(02\)52004-4](https://doi.org/https://doi.org/10.1016/S1063-5823(02)52004-4).
- (102) Abraham, T.; Lewis, R. N. A. H.; Hodges, R. S.; McElhaney, R. N. Isothermal Titration Calorimetry Studies of the Binding of the Antimicrobial Peptide Gramicidin S to Phospholipid Bilayer Membranes. *Biochemistry* **2005**, *44* (33), 11279–11285. <https://doi.org/10.1021/bi050898a>.

- (103) Bong, D. T.; Janshoff, A.; Steinem, C.; Ghadiri, M. R. Membrane Partitioning of the Cleavage Peptide in Flock House Virus. *Biophys. J.* **2000**, *78* (2), 839–845. [https://doi.org/https://doi.org/10.1016/S0006-3495\(00\)76641-0](https://doi.org/https://doi.org/10.1016/S0006-3495(00)76641-0).
- (104) Verwey, E. J. W.; Overbeek, J. T. .; Nes, K. *Theory of the Stability of Lyophobic Colloids: The Interaction of Sol Particles Having an Electric Double Layer.*; Elsevier Publishing Company: New York, NY, 1948.
- (105) Tadros, T. F.; Vladisavljević, G. T.; Kobayashi, I.; Nakajima, M.; Mucic, N.; Pradines, V.; Javadi, A.; Sharipova, A.; Krägel, J.; Leser, M. E.; et al. Emulsion Formation, Stability, and Rheology. *Emulsion Formation and Stability*. January 29, 2013, pp 1–75. <https://doi.org/doi:10.1002/9783527647941.ch1>.
- (106) Chibowski, E.; Szcześ, A. Zeta Potential and Surface Charge of DPPC and DOPC Liposomes in the Presence of PLC Enzyme. *Adsorption* **2016**, *22* (4), 755–765. <https://doi.org/10.1007/s10450-016-9767-z>.
- (107) Satoh, K. Determination of Binding Constants of Ca²⁺, Na⁺, and Cl[–] Ions to Liposomal Membranes of Dipalmitoylphosphatidylcholine at Gel Phase by Particle Electrophoresis. *Biochim. Biophys. Acta - Biomembr.* **1995**, *1239* (2), 239–248. [https://doi.org/https://doi.org/10.1016/0005-2736\(95\)00154-U](https://doi.org/https://doi.org/10.1016/0005-2736(95)00154-U).
- (108) Jämbeck, J. P. M.; Lyubartsev, A. P. Derivation and Systematic Validation of a Refined All-Atom Force Field for Phosphatidylcholine Lipids. *J. Phys. Chem. B* **2012**, *116* (10), 3164–3179. <https://doi.org/10.1021/jp212503e>.
- (109) Lindorff-Larsen, K.; Piana, S.; Palmo, K.; Maragakis, P.; Klepeis, J. L.; Dror, R. O.; Shaw, D. E. Improved Side-Chain Torsion Potentials for the Amber Ff99SB Protein Force Field. *Proteins Struct. Funct. Bioinforma.* **2010**, *78* (8), 1950–1958. <https://doi.org/10.1002/prot.22711>.
- (110) Berendsen, H. J. C.; van der Spoel, D.; van Drunen, R. GROMACS: A Message-Passing Parallel Molecular Dynamics Implementation. *Comput. Phys. Commun.* **1995**, *91* (1), 43–56. [https://doi.org/https://doi.org/10.1016/0010-4655\(95\)00042-E](https://doi.org/https://doi.org/10.1016/0010-4655(95)00042-E).
- (111) Humphrey, W.; Dalke, A.; Schulten, K. VMD: Visual Molecular Dynamics. *J. Mol. Graph.* **1996**, *14* (1), 33–38. [https://doi.org/https://doi.org/10.1016/0263-7855\(96\)00018-5](https://doi.org/https://doi.org/10.1016/0263-7855(96)00018-5).
- (112) Jorgensen, W. L.; Chandrasekhar, J.; Madura, J. D.; Impey, R. W.; Klein, M. L. Comparison of Simple Potential Functions for Simulating Liquid Water. *J. Chem. Phys.* **1983**, *79* (2), 926–935. <https://doi.org/10.1063/1.445869>.
- (113) Bussi, G.; Donadio, D.; Parrinello, M. Canonical Sampling through Velocity Rescaling. *J. Chem. Phys.* **2007**, *126* (1), 14101. <https://doi.org/10.1063/1.2408420>.
- (114) Hess, B.; Bekker, H.; Berendsen, H. J. C.; Fraaije, J. LINCS: A Linear Constraint Solver for Molecular Simulations. *J. Comput. Chem.* **1997**, *18* (12), 1463–1472.
- (115) Darden, T.; York, D.; Pedersen, L. Particle Mesh Ewald: An N·log(N) Method for Ewald Sums in Large Systems. *J. Chem. Phys.* **1993**, *98* (12), 10089–10092. <https://doi.org/10.1063/1.464397>.
- (116) Nosé, S. A Molecular Dynamics Method for Simulations in the Canonical Ensemble. *Mol. Phys.* **1984**, *52* (2), 255–268. <https://doi.org/10.1080/00268978400101201>.
- (117) Parrinello, M.; Rahman, A. Polymorphic Transitions in Single Crystals: A New Molecular Dynamics Method. *J. Appl. Phys.* **1981**, *52* (12), 7182–7190. <https://doi.org/10.1063/1.328693>.

- (118) Ulmschneider, J. P.; Smith, J. C.; Ulmschneider, M. B.; Ulrich, A. S.; Strandberg, E. Reorientation and Dimerization of the Membrane-Bound Antimicrobial Peptide PGLa from Microsecond All-Atom MD Simulations. *Biophys. J.* **2012**, *103* (3), 472–482. <https://doi.org/10.1016/j.bpj.2012.06.040>.
- (119) Verly, R. M.; Resende, J. M.; Junior, E. F. C.; De Magalhães, M. T. Q.; Guimarães, C. F. C. R.; Munhoz, V. H. O.; Bemquerer, M. P.; Almeida, F. C. L.; Santoro, M. M.; Piló-Veloso, D.; et al. Structure and Membrane Interactions of the Homodimeric Antibiotic Peptide Homotarsinin. *Sci. Rep.* **2017**, *7* (March 2014), 1–13. <https://doi.org/10.1038/srep40854>.
- (120) Wieprecht, T.; Beyermann, M.; Seelig, J. Binding of Antibacterial Magainin Peptides to Electrically Neutral Membranes: Thermodynamics and Structure. *Biochemistry* **1999**, *38* (32), 10377–10387. <https://doi.org/10.1021/bi990913+>.
- (121) López Cascales, J. J.; Zenak, S.; García De La Torre, J.; Lezama, O. G.; Garro, A.; Enriz, R. D. Small Cationic Peptides: Influence of Charge on Their Antimicrobial Activity. *ACS Omega* **2018**, *3* (5), 5390–5398. <https://doi.org/10.1021/acsomega.8b00293>.

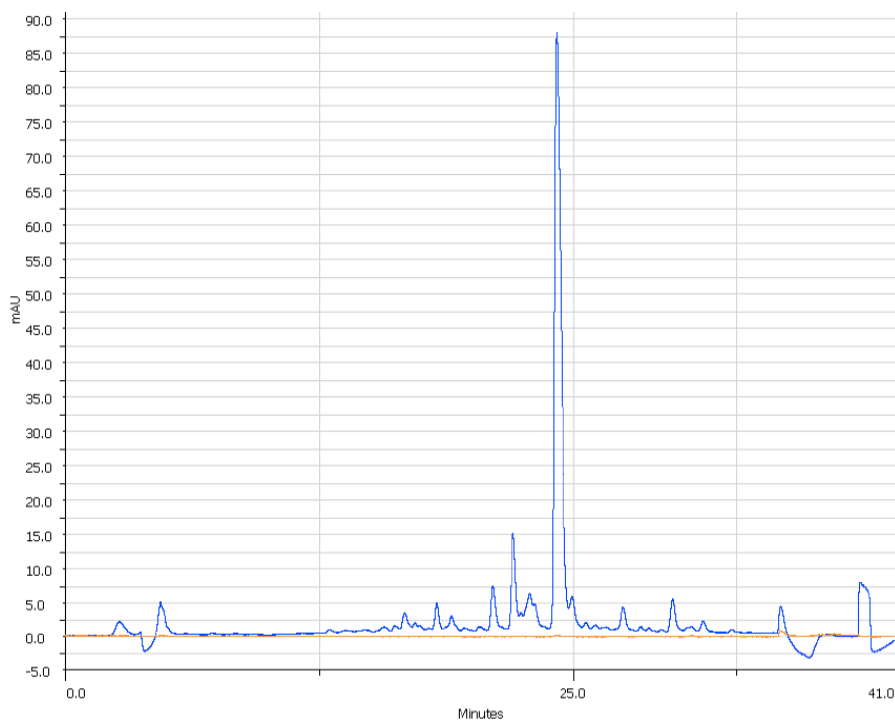
APPENDIX 1

Number	([² H ₃]-Ala-10, ¹⁵ N-Leu-17)-OceF1				([² H ₃]-Ala-8, ¹⁵ N-Leu-10)-[pOAcGlc-Trz-A1]-HSP1-NH2				([² H ₃]-Ala-8, ¹⁵ N-Leu-14)-[pOAcGlc-Trz-A14]-PS-2			
	Amino acid	Reagent excess	Reaction Time (h)	Recoupling conditions	Amino acid	Reagent excess	Reaction Time (h)	Recoupling conditions	Amino acid	Reagent excess	Reaction Time (h)	Recoupling conditions
1	L	4	3	-	G	4	3	-	F	4	3	-
2	K	4	2	-	A	4	2	-	H	4	3	-
3	N	4	2	-	A	4	2	-	H	4	2	-
4	M	4	2.3	-	K	4	2	-	V	4	3	-
5	V	4	2.5	-	A	4	4	-	L	4	4	-
6	K	4	2.5	-	I	4	3.5	-	[Pra]	1.5	4	-
7	S	4	2	-	A	4	4	-	S	4	3	-
8	A	4	2	-	K	4	3	-	V	4	4	4/2h
9	L	4	4	-	I	4	3.5	4/4h	A	4	4	-
10	H	4	2	-	A	4	3	-	N	4	4	-
11	G	4	2.3	-	D	4	3.5	5/4h	I	4	4	-
12	A	4	2	-	L	4	3.5	-	A	4	4	-
13	I	4	2	-	I	4	4	4/4h	H	4	4	-
14	D	4	2	-	[Pra]	1.5	4	-	P	4	4	-
15	K	4	3	-	-	-	-	-	I	4	4	-
16	A	4	4	-	-	-	-	-	L	4	4	-
17	A	4	2	-	-	-	-	-	S	4	4	-
18	G	4	3	-	-	-	-	-	L	4	4	-
19	K	4	2.3	-	-	-	-	-	F	4	4	-
20	L	4	2	-	-	-	-	-	-	-	-	-
21	I	5	2	6/2.5h	-	-	-	-	-	-	-	-
22	D	5	3.5	-	-	-	-	-	-	-	-	-
23	V	5	4	-	-	-	-	-	-	-	-	-
24	V	5	4	-	-	-	-	-	-	-	-	-
25	G	5	4	-	-	-	-	-	-	-	-	-

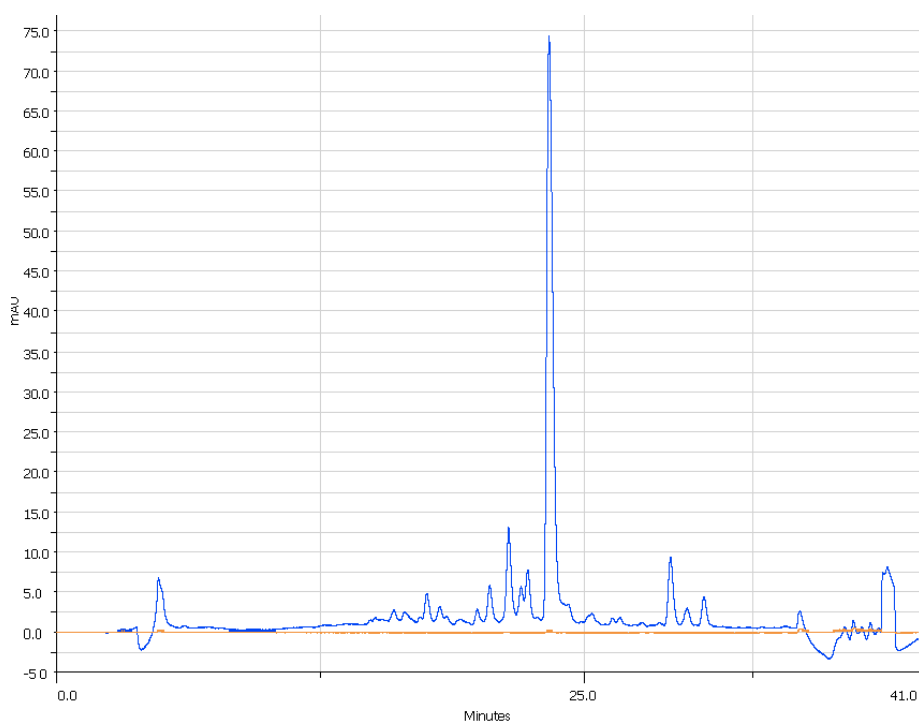
*Note that peptides are synthesized from C-terminus to N-terminus. Recoupling constants (Reagent excess/time in hours)

APPENDIX 2

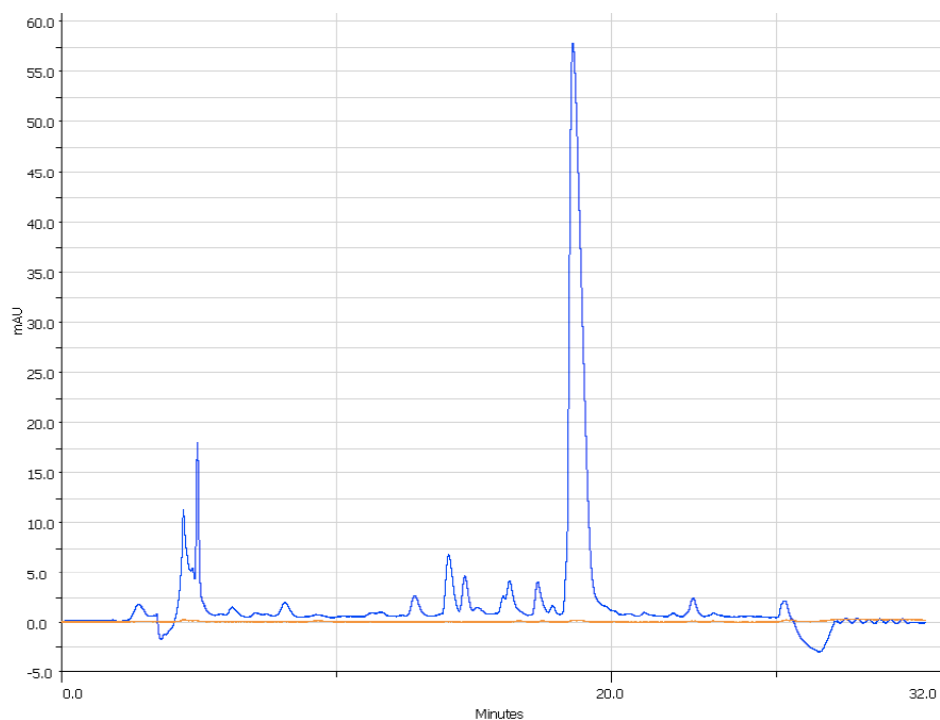
HPLC chromatogram obtained for Oce-LB1 purification, with a Luna 5 μm C18 100 \AA reverse stationary phase (150 x 3000 mm):



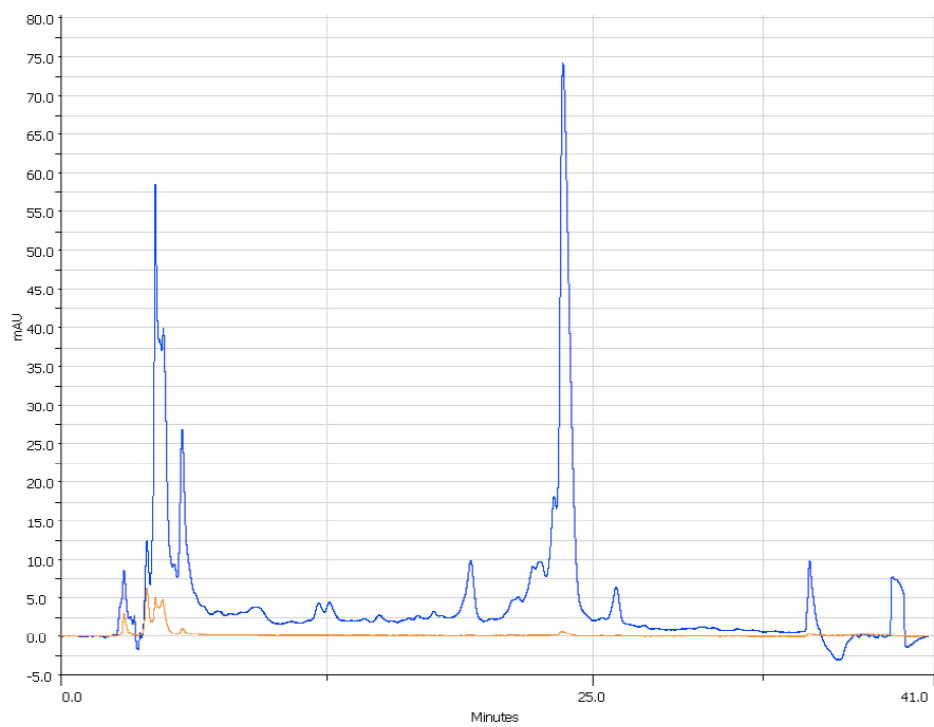
HPLC chromatogram obtained for Oce-LB2 purification, with a Luna 5 μm C18 100 \AA reverse stationary phase (150 x 3000 mm):



HPLC chromatogram obtained for [pOAcGlc-Trz-A¹]-HSP1-NH₂ purification, with a Luna 5 μ m C18 100 Å reverse stationary phase (150 x 3000 mm):

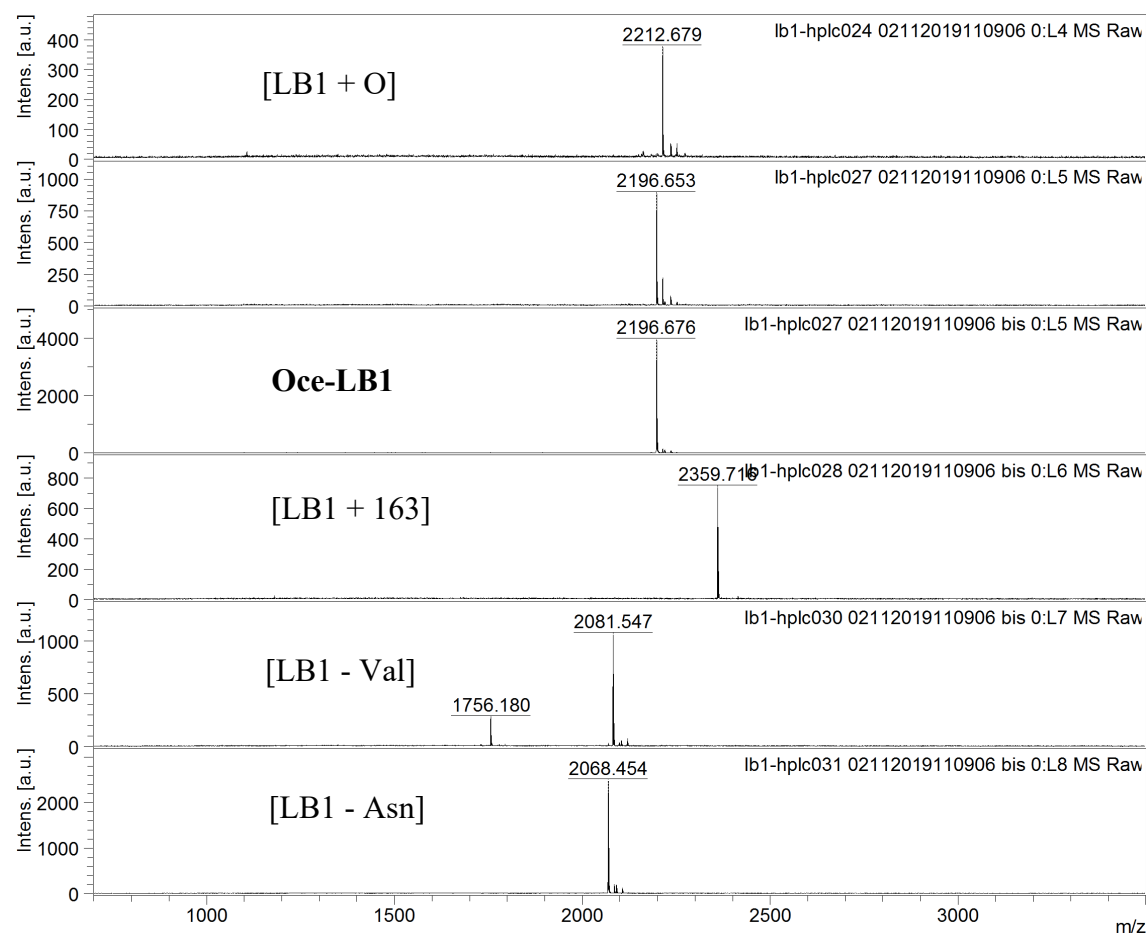


HPLC chromatogram obtained for [pOAcGlc-Trz-A¹]-PS-2 purification, with a Luna 5 μ m C18 100 Å reverse stationary phase (150 x 3000 mm):

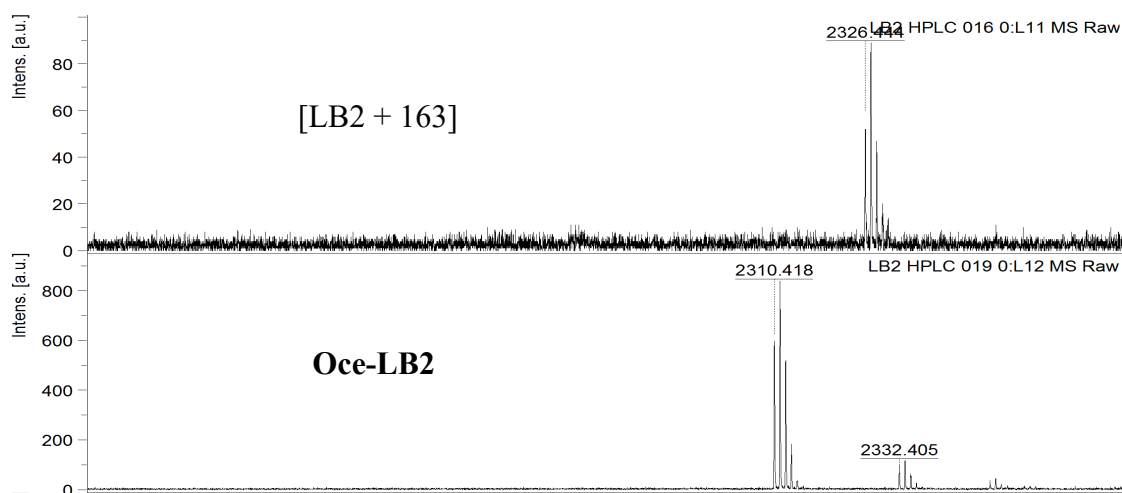


APPENDIX 3

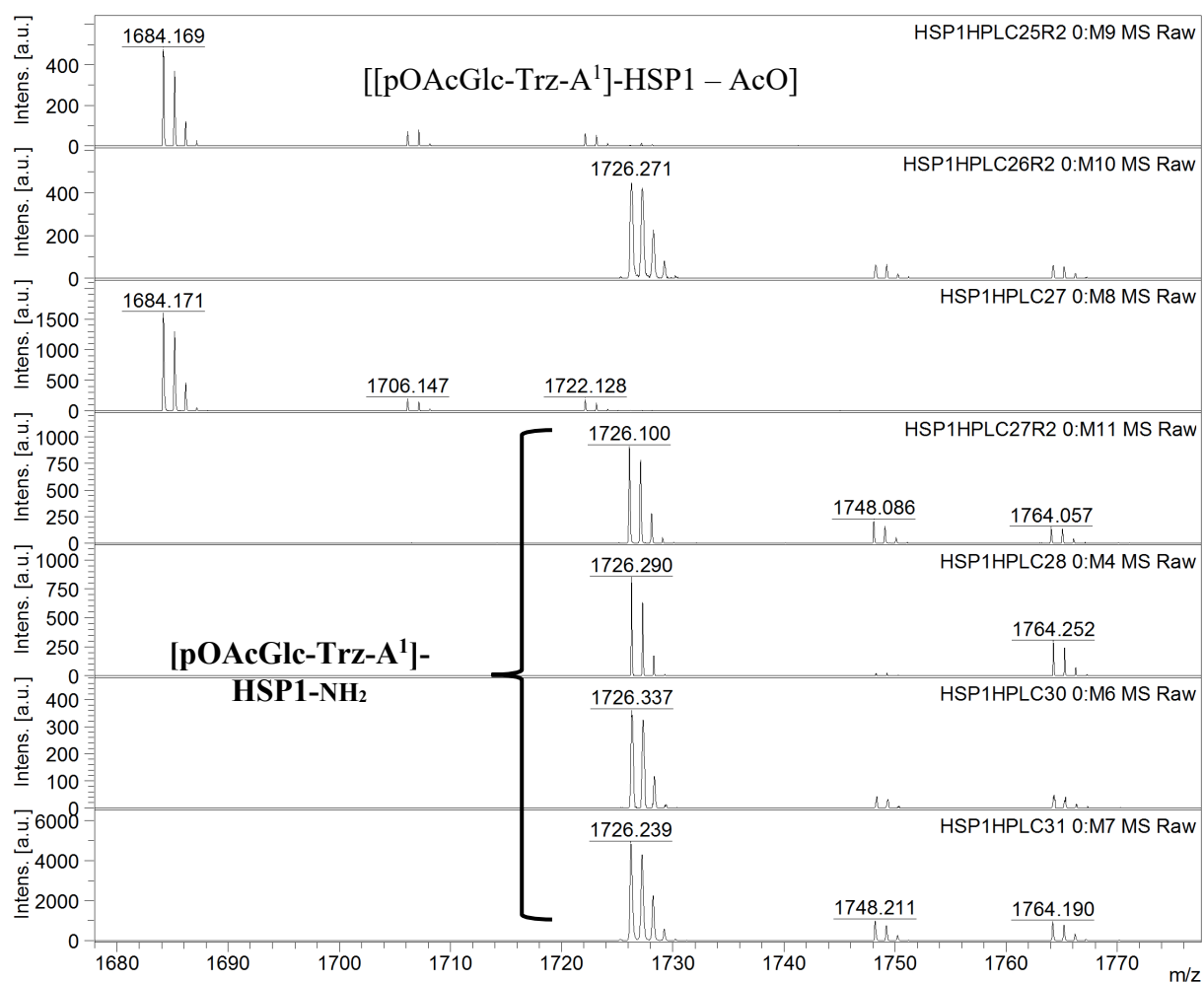
Mass spectra obtained by MALDI-TOF spectrometry for some collected fractions during the purification of Oce-LB2:



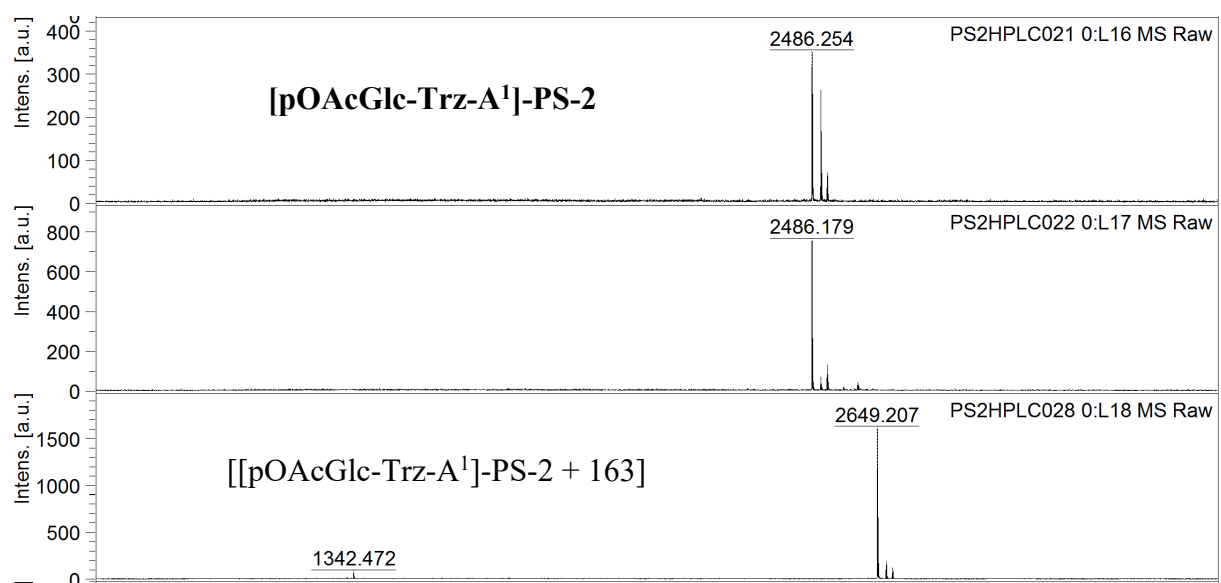
Mass spectra obtained by MALDI-TOF spectrometry for some collected fractions during the purification of Oce-LB2:



Mass spectra obtained by MALDI-TOF spectrometry for some collected fractions during the purification of [pOAcGlc-Trz-A¹]-HSP1-NH₂:



Mass spectra obtained by MALDI-TOF spectrometry for some collected fractions during the purification of [pOAcGlc-Trz-A¹⁴]-PS-2:



APPENDIX 4

Authorizations for the use of some figures used in this master's thesis.

The simulated solid-state NMR ^{15}N spectra from Figure 24 was taken from: "Alignment and structural analysis of membrane polypeptides by ^{15}N and ^{31}P solid-state NMR spectroscopy", **Concepts in Magnetic Resonance: Part A**, 2002, B. Bechinger *et al.*

Thank you for your order!

Dear Mr. Jose Maria Muñoz Lopez,

Thank you for placing your order through Copyright Clearance Center's RightsLink[®] service.

Order Summary

Licensee: jmunz
Order Date: Mar 3, 2020
Order Number: 4781160439297

Publication: Concepts in Magnetic Resonance: Part A, Bridging Education and Research
Title: Alignment and structural analysis of membrane polypeptides by ^{15}N and ^{31}P solid-state NMR spectroscopy
Type of Use: Dissertation/Thesis
Order Total: 0.00 USD

View or print complete [details](#) of your order and the publisher's terms and conditions.


Sincerely,

Copyright Clearance Center

Figure 1 was taken from an open-access article: "Defensins: antifungal lessons from eukaryotes", **Frontiers in Microbiology**, 2014, Silva *et al.* (<https://www.frontiersin.org/articles/10.3389/fmicb.2014.00097/full> last access on 03/03/2020)

Copyright © 2014 Silva, Gonçalves and Santos. This is an open-access article distributed under the terms of the **Creative Commons Attribution License (CC BY)** (<http://creativecommons.org/licenses/by/3.0/>). The use, distribution or reproduction in other forums is permitted, provided the original author(s) or licensor are credited and that the original publication in this journal is cited, in accordance with accepted academic practice. No use, distribution or reproduction is permitted which does not comply with these terms.

Correspondence:

Frasca V  Malvern Instruments, 22
Industrial Drive East, Northampton, MA 01060,
USA.
Phone: +1-4135701515.

Citation:

Frasca V. Biophysical characterization of
antibodies with isothermal titration
calorimetry. *J Appl Bioanal* 2(3), 90-102
(2016).

Open-access and Copyright:

©2016 Frasca V. This article is an open access
article distributed under the terms of the
[Creative Commons Attribution License \(CC-
BY\)](#) which permits any use, distribution, and
reproduction in any medium, provided the
original author(s) and source are credited.

Figure 37 was taken from an open-access article: “Biophysical characterization of antibodies with isothermal titration calorimetry”, **Journal of Applied Bioanalysis**, 2016, Verna Frasca.

(<https://betasciencepress-publishing.com/10-17145/fulltext/jab/biophysical-characterization-of-antibodies-with-isothermal-titration-calorimetry/> last access on 03/03/2020)

Both Figures 38 and 39 were taken from: “Surface plasmon resonance spectroscopy for characterization of membrane protein-ligand interactions and its potential for drug discovery”, **Biochimica et Biophysica acta (BBA)-Biomembranes**, 2014, Simon G. Patching *et al.*

Thank you for your order!

Dear Mr. Jose Maria Muñoz Lopez,

Thank you for placing your order through Copyright Clearance Center's RightsLink[®] service.

Order Summary

Licensee: jmunz
Order Date: Mar 2, 2020
Order Number: 4780930381263
Publication: Biochimica et Biophysica Acta (BBA) - Biomembranes
Title: Surface plasmon resonance spectroscopy for characterisation of
membrane protein–ligand interactions and its potential for drug discovery
Type of Use: reuse in a thesis/dissertation
Order Total: 0.00 USD

View or print complete [details](#) of your order and the publisher's terms and conditions.

Sincerely,

Copyright Clearance Center

